Focused mid-crustal magma intrusion during continental break-up in Ethiopia

Kevin Wong[1], David Ferguson[1], Penny Wieser[2], Daniel Morgan[1], Marie Edmonds[3], Amdemichael Zafu Tadesse[4], Gezahegn Yirgu[5], Jason Harvey[6], and Samantha J Hammond[7]

[1]University of Leeds
[2]UC Berkeley
[3]University of Cambridge
[4]Free University of Brussels (ULB)
[5]Addis Ababa University
[6]Leeds University
[7]Open University

March 1, 2023

Abstract

Significant volumes of magma are intruded into the crust during continental break-up, which can influence rift evolution by altering thermo-mechanical structure of the crust and thereby its response to extensional stresses. Rift magmas additionally feed surface volcanic activity and can be globally significant sources of tectonic CO2 emissions. Understanding how magmatism may affect rift development requires knowledge on magma intrusion depths in the crust. Here, using data from olivine-hosted melt inclusions, we investigate magma dynamics for basaltic intrusions in the Main Ethiopian Rift (MER). We find evidence for a spatially focused zone of magma intrusion at the MER upper-lower crustal boundary (10-15 km depth), consistent with geophysical datasets. We propose that ascending melts in the MER are intruded over this depth range as discrete sills, likely creating a mechanically weak mid-crustal layer. Our results have important implications for how magma addition can influence crustal rheology in a maturing continental rift.

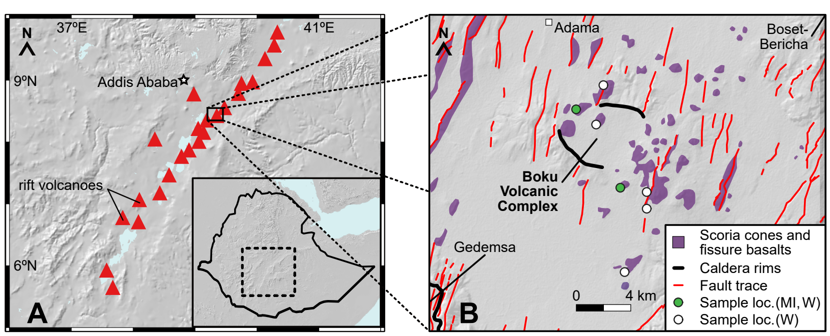

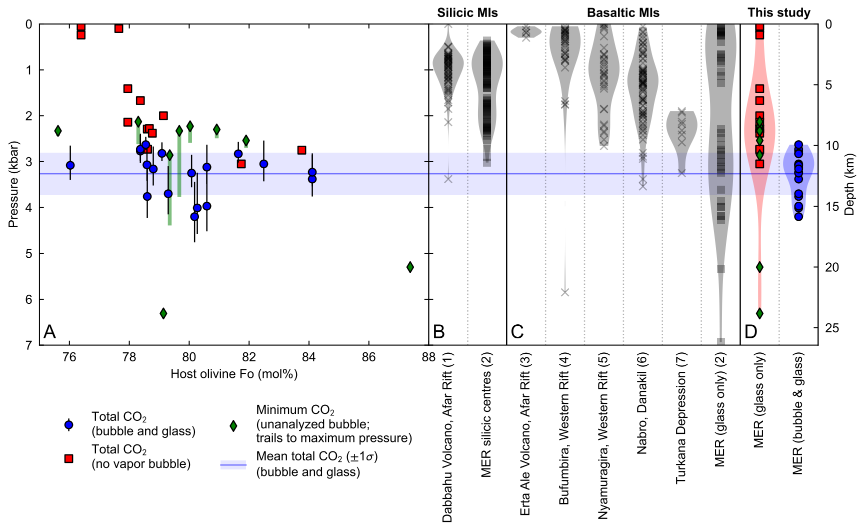
Silicic MIs
Basaltic MIs
This study
Pressure (kbar)
Depth (km)
Host olivine Fo (mol%)
A
B
C
D
Dabbahu Volcano, Afar Rift (1)
MER silicic centres (2)
Erta Ale Volcano, Afar Rift (3)
Bufumbira, Western Rift (4)
Nyamuragira, Western Rift (5)
Nabro, Danakil (6)
Turkana Depression (7)
MER (glass only) (2)
MER (glass only)
MER (bubble & glass)
Total CO_2 (bubble and glass)
Total CO_2 (no vapor bubble)
Minimum CO_2 (unanalyzed bubble; trails to maximum pressure)
Mean total CO_2 ($\pm1\sigma$) (bubble and glass)

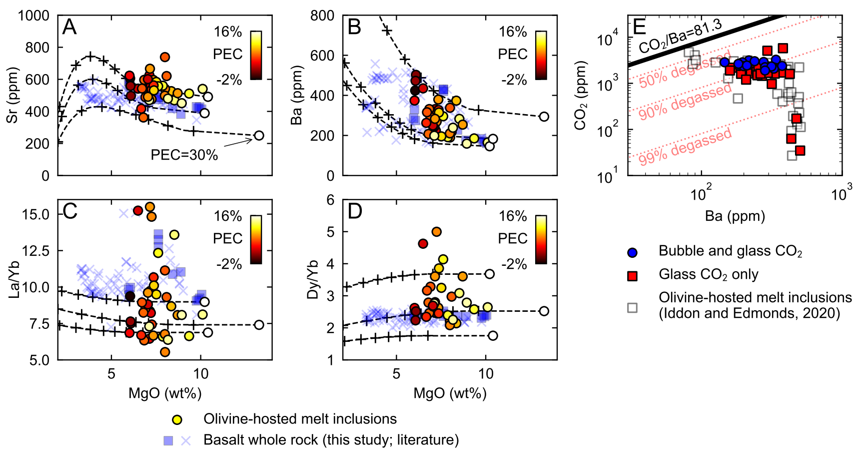
A
B
C
D
E
Sr (ppm)
Ba (ppm)
La/Yb
Dy/Yb
MgO (wt%)
16%
PEC
-2%
PEC=30%
CO_2/Ba=81.3
50% degassed
90% degassed
99% degassed
CO_2 (ppm)
Ba (ppm)
Bubble and glass CO_2
Glass CO_2 only
Olivine-hosted melt inclusions (Iddon and Edmonds, 2020)
Olivine-hosted melt inclusions
Basalt whole rock (this study; literature)

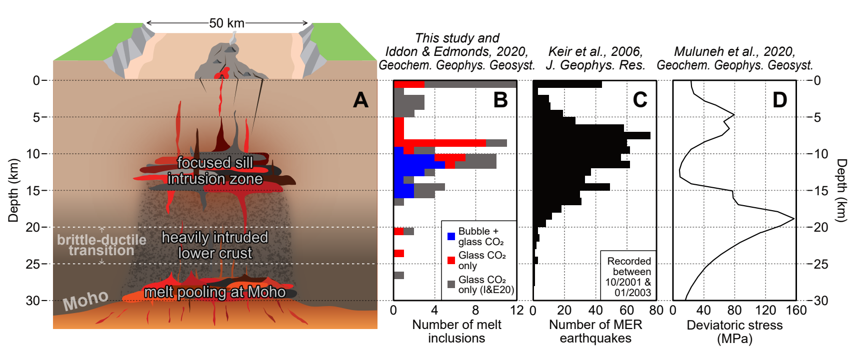
50 km
A
B
C
D
focused sill intrusion zone
heavily intruded lower crust
brittle-ductile transition
melt pooling at Moho
Moho
Depth (km)
This study and Iddon & Edmonds, 2020, Geochem. Geophys. Geosyst.
Keir et al., 2006, J. Geophys. Res.
Muluneh et al., 2020, Geochem. Geophys. Geosyst.
Bubble + glass CO_2
Glass CO_2 only
Glass CO_2 only (I&E20)
Recorded between 10/2001 & 01/2003
Number of melt inclusions
Number of MER earthquakes
Deviatoric stress (MPa)

Focused mid-crustal magma intrusion during continental break-up in Ethiopia

Kevin Wong[1*], David Ferguson[1], Penny Wieser[2], Daniel Morgan[1], Marie Edmonds[3], Amdemichael Zafu Tadesse[4], Gezahegn Yirgu[5], Jason Harvey[1], and Samantha Hammond[6]

[1]School of Earth and Environment, University of Leeds, Leeds LS2 9JT, United Kingdom
[2]Earth and Planetary Science, University of California, Berkeley, CA 94720-4767, United States of America
[3]Centre for the Observation and Modelling of Earthquakes, Volcanoes and Tectonics (COMET), Department of Earth Sciences, University of Cambridge, Cambridge CB2 3EQ, United Kingdom
[4]Department of Geosciences, Environment and Society, Université Libre de Bruxelles (ULB), 50 B-1050 Bruxelles, Belgium
[5]School of Earth Sciences, Addis Ababa University, P. O. Box 1176 Addis Ababa, Ethiopia
[6]School of Environment, Earth and Ecosystems Sciences, The Open University, Milton Keynes MK7 6AA, United Kingdom

Key Points:

- We determine magma storage conditions in the Main Ethiopian Rift through geochemical analysis of olivine-hosted melt inclusions.
- Volatile saturation barometry reveals that basaltic melts are focused at 10–15 km depth in the Ethiopian crust.
- Geochemical heterogeneity in melt inclusions suggests that magma storage is likely to occur in semi-discrete sills.

*Current address, Department of Biological, Geological, and Environmental Sciences (BiGeA), Alma Mater Studiorum Università di Bologna, Piazza di Porta San Donato 1, 40126, Bologna, Italy

Corresponding author: Kevin Wong, `kevin.wong@unibo.it`

Abstract

Significant volumes of magma are intruded into the crust during continental break-up, which can influence rift evolution by altering thermo-mechanical structure of the crust and thereby its response to extensional stresses. Rift magmas additionally feed surface volcanic activity and can be globally significant sources of tectonic CO_2 emissions. Understanding how magmatism may affect rift development requires knowledge on magma intrusion depths in the crust. Here, using data from olivine-hosted melt inclusions, we investigate magma dynamics for basaltic intrusions in the Main Ethiopian Rift (MER). We find evidence for a spatially focused zone of magma intrusion at the MER upper-lower crustal boundary (10-15 km depth), consistent with geophysical datasets. We propose that ascending melts in the MER are intruded over this depth range as discrete sills, likely creating a mechanically weak mid-crustal layer. Our results have important implications for how magma addition can influence crustal rheology in a maturing continental rift.

Plain Language Summary

Continental rifting, the break-up of continents to form new ocean basins, is a key component in the tectonic cycle that affects Earth's surface environment. The rifting process is aided by magmatic activity in its final stages, which weakens the crust by heating it. This is believed to facilitate present-day rifting in Ethiopia, where we can find rift-related volcanoes. Where melts are stored in the rifting crust will determine how heat is distributed, and therefore how the physical properties of the crust will be altered. Here we analyse melt inclusions, small pockets of precursor magmas trapped in crystals. Because melt inclusions are trapped at depth they record key geochemical information about the conditions magmas experience as they enter the crust from the mantle. By considering the concentrations of CO_2 and H_2O in our melt inclusions we demonstrate that magmas are focused in a 10–15 km zone in the rifting Ethiopian crust. The diverse geochemistry of our melt inclusions additionally suggests that magmas do not substantially mix together in the crust, and are likely to be stored within non-interacting magmatic bodies. This study therefore provides new insights into how melts are stored in the Ethiopian crust before volcanic eruptions.

1 Introduction

Continental rifting involves the rupture of strong continental lithosphere to form new ocean basins. Evidence from active continental rifts and passive margins suggests that continental break-up often involves intrusion of substantial volumes of magma into the rifting crust (e.g., White et al., 2008; Bastow et al., 2011; Bastow & Keir, 2011). These magmas can accommodate extension via dyke intrusion and, depending on their distribution in space and time, may alter the thermo-mechanical structure of the crust (e.g., Buck, 2006; Daniels et al., 2014; Lavecchia et al., 2016; Muluneh et al., 2020). Determining where and how intruded melts accumulate during rift development is therefore crucial for understanding how the rheology and density structure of the crust evolves with progressive rifting, which in turn has a strong influence on how the crust responds to far-field extensional stresses during non-magmatic and magmatic rifting regimes (e.g., Bialas et al., 2010; Tetreault & Buiter, 2018; Oliveira et al., 2022).

Although the syn-rift interplay between magmatism and tectonics is a key ingredient in facilitating continental break-up (e.g., Thybo & Nielsen, 2009; Bastow & Keir, 2011), observational constraints on the depths of basaltic intrusion in active rifts obtained through petrology and geochemistry remain limited. While geophysical observations can infer depths of intrusion and storage of crustal melts (e.g., seismicity concurrently triggered during emplacement; Keir et al., 2006; Ebinger et al., 2008), only petrological observations, obtained from basaltic materials derived directly from the intruding melts

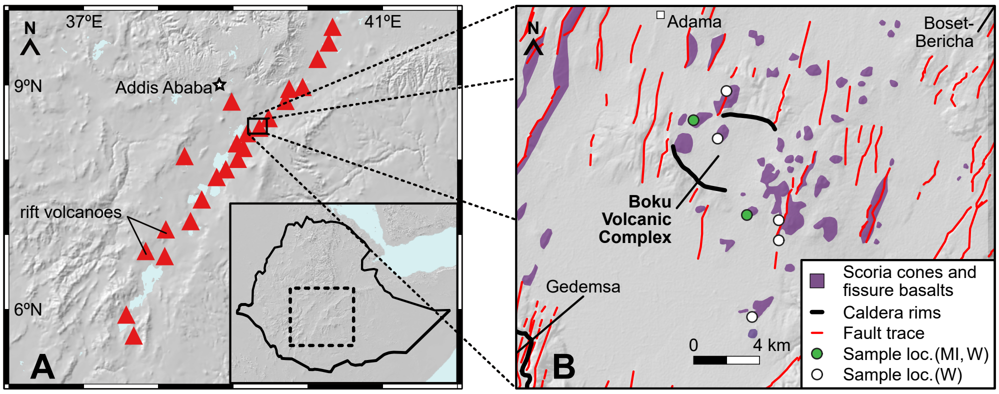

Figure 1. A. The location of the Boku Volcanic Complex in the MER. B. Simplified geological map of Boku, with olivine-hosted melt inclusion (MI) and whole-rock (W) sample localities shown. Digital elevation models are GTOPO30 (A) and SRTM (B). Volcano locations in subfigure A are obtained from the Global Volcanism Program, Smithsonian Institution (`https://volcano.si.edu/`).

themselves, can provide first-hand evidence of the magmatic conditions associated with crustal emplacement.

The Main Ethiopian Rift (MER), comprising the northernmost sector of the East African Rift system (EARS), provides a natural laboratory to examine the interplay between rift geodynamics and magmatic intrusion. This late-stage continental rift, which bridges the large fault-bound grabens of the Kenyan Rift and inferred incipient seafloor spreading in Afar (Figure 1A), has been extensively studied through multiple geophysical approaches (e.g., Bastow et al., 2011). These studies suggest that significant magma intrusion has occurred in the MER lithosphere, focused under ∼20 km-wide and ∼60 km-long magmatic-tectonic segments (e.g., Bastow et al., 2011), where as much as half of the crustal volume may comprise new igneous material (Maguire et al., 2006; Daniels et al., 2014). The compositional and thermal effects of magma intrusion may modify the response of the Ethiopian crust to extension, determining where and how strain is localized as rifting proceeds (e.g., Bastow & Keir, 2011; Lavecchia et al., 2016). Furthermore, degassing of intruded melts during and after emplacement contributes to the significant diffuse CO_2 fluxes measured in the MER (Hunt et al., 2017).

In this study we use petrological methods to investigate the storage depths and compositional diversity of intruded basaltic magmas in the northern MER. Our constraints on magma intrusion conditions are derived from analysis of olivine-hosted silicate melt inclusions (MIs), which are small pockets of quenched magma trapped within growing crystals during crustal magma storage (e.g., Wallace et al., 2021). Unlike erupted lavas, MIs can preserve magmatic volatile contents (e.g., CO_2, H_2O etc., Wallace et al., 2021), allowing volatile saturation pressures, and therefore magmatic storage depths, to be determined (e.g., Ghiorso & Gualda, 2015). Of particular importance is the volatile species CO_2, which degases strongly with decreasing pressure in basaltic magmas (e.g., Dixon et al., 1995). Continental rifts, including the MER, are known to be significant sources of passively degassing magmatic CO_2 (Lee et al., 2016; Foley & Fischer, 2017; Hunt et al., 2017). By considering the total CO_2 in MIs, entrapped within both glass and bubble, we provide new well-constrained petrological estimates of basaltic intrusion pressures in the MER.

2 Materials and Methods

Our samples are scoriae from the Boku Volcanic Complex, a Quaternary monogenetic basaltic cone field located in the northern MER (Figure 1B Tadesse et al., 2019). Littering the remnants of a collapsed ∼500 ka caldera, the later-stage ∼200 ka basaltic cones and fissure flows of Boku are associated with adjacent faults which are sub-parallel to the strike of the MER (Figure 1; Rooney et al., 2011; Tadesse et al., 2019). Quarries provide access into the interiors of cones, where fresh glassy basaltic scoria can be sampled.

Olivine crystals from two Boku cones (Figure 1), picked from disaggregated scoria, were characterized for MIs, individually polished to 0.25 μm grade on glass slides to expose MIs, and mounted in epoxy resin. We have measured the compositions of 40 MIs (full methods in Supporting Information). 27 of these MIs contain CO_2-rich vapor bubbles, which form from post-entrapment changes in pressure, volume and temperature (e.g., Moore et al., 2015; Maclennan, 2017). Bubbles can host a significant fraction of the MI CO_2 budget (e.g., Hartley et al., 2014; Wieser et al., 2021). To estimate the total CO_2 in MIs, essential for accurate barometry, 18 MIs were additionally assessed for shrinkage bubble CO_2 density using Raman spectroscopy. Our approach differs from previous studies considering MIs from the EARS in this regard, which have opted to either a) experimentally rehomogenize the bubble (Head et al., 2011; Hudgins et al., 2015), b) use CO_2 equation of state methods (Rooney et al., 2022), or c) select MIs without vapor bubbles wherever possible (Field, Barnie, et al., 2012; Field, Blundy, et al., 2012; A. Donovan et al., 2017; Iddon & Edmonds, 2020). The primary advantage of our approach is the direct measurement of bubble CO_2 without making assumptions concerning bubble cooling history and post-entrapment processes or experimentally modifying the MI glass composition, which will introduce uncertainties that are difficult to assess and quantify (Rasmussen et al., 2020; Wieser et al., 2021). In addition, by selecting bubble-hosting MIs we avoid biases towards magmatic conditions that favor bubble-free MIs, which may not be representative of crustal melt storage. By doing so, we provide a robust estimate of total CO_2 in an MI, which can be used to determine crustal melt storage pressures.

After Raman spectroscopy, all MIs were analysed for trace and volatile elements in the glass phase by SIMS. This was followed by EPMA to assess major element compositions of MI glass, carrier melt, and host olivine crystals. MI compositions were corrected for post-entrapment crystallization (PEC) using Petrolog3 software (Danyushevsky & Plechov, 2011, full details in Supporting Information). The total CO_2 of MIs is calculated by mass balance using the CO_2 measured in the bubble and MI glass (e.g., Hartley et al., 2014). To complement the MI compositional dataset, we have additionally assessed the major and trace element whole-rock compositions of basalts collected from several Boku scoria cones and fissure flows using XRF and solution ICP-MS respectively. All standards and geochemical data are presented in Supporting Dataset S1.

3 Results

3.1 Magma Intrusion Depths in the Main Ethiopian Rift

Our key barometric and geochemical results are presented in Figures 2 and 3, with additional figures presented in the Supporting Information. MIs are entrapped within olivine crystals of composition Fo_{76-88}, and there are no systematic differences in major, trace, or volatile element concentrations between MIs collected from the two cones in this study (Dataset S1). CO_2 concentrations range from 35–5770 ppm in MI glass only; MIs with CO_2 measurements in both the glass and vapor bubble have total combined CO_2 contents of 1895–3248 ppm, with 15–46% of the CO_2 residing within the bubble (Dataset S1). Where an unanalyzed shrinkage bubble is present, CO_2 contents are assumed to be minima and we estimate the plausible range of total CO_2 using our bub-

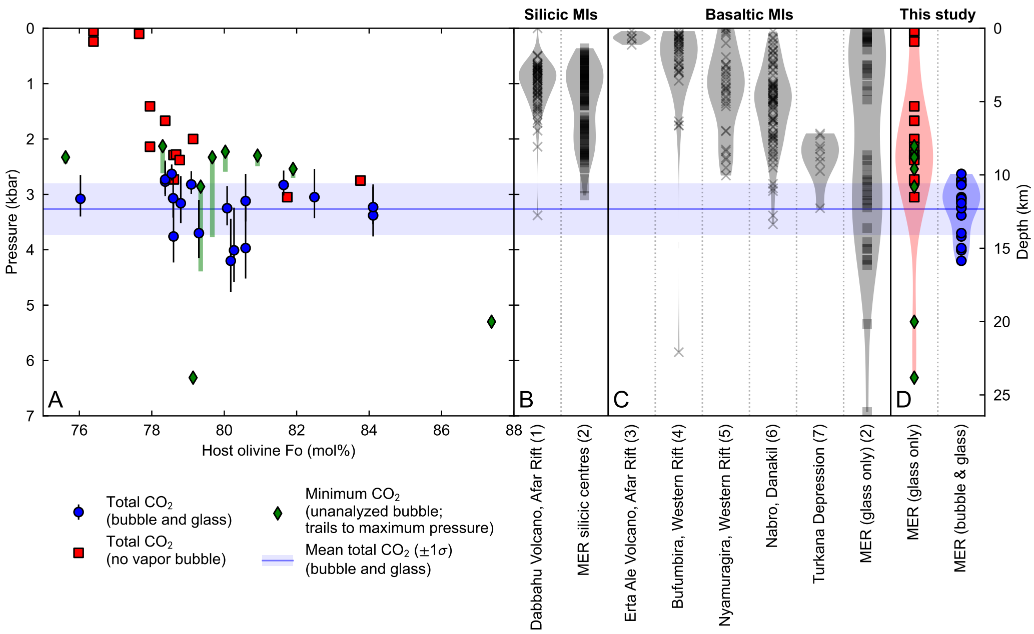

Figure 2. A. Volatile CO_2-H_2O saturation pressures of olivine-hosted MIs from the MER, plotted against MI olivine host Fo (olivine Fo=100·Mg/(Fe+Mg)). MIs are categorized on which components are analyzed. Physical dimensions of MI vapor bubbles that are analyzed only for glass composition can be used to estimate maximum CO_2 if bubble CO_2 density is well characterized (green diamonds); this is performed assuming a density of 0.21 g cm^{-3} (see Supporting Information). Error bars on pressures calculated from MIs for which bubble and glass are analysed are 1σ. B–D. Violin plots of volatile CO_2-H_2O saturation pressures recorded by mineral-hosted MIs from the EARS and Afar calculated using MagmaSat. Saturation pressures are individually determined for each MI using their recorded major and trace element composition and magmatic temperatures. Where FeO_t is provided without Fe_2O_3 all Fe is assumed to be Fe^{2+}. Subfigure B shows distributions of silicic MIs (SiO_2 >60 wt%), subfigure C shows basaltic MIs (SiO_2 <55 wt%), and subfigure D shows the basaltic MIs of this study. The blue line and shaded area across all subfigures marks the mean and 1σ of the MI subset of this study with combined vapor bubble and glass CO_2. References: 1. Field, Blundy, et al. (2012); 2. Iddon and Edmonds (2020), shown as squares for emphasis; 3. Field, Barnie, et al. (2012); 4. Hudgins et al. (2015); 5. Head et al. (2011); 6. A. Donovan et al. (2017); 7. Rooney et al. (2022), without bubble corrections.

ble CO_2 density measurements (see Supporting Information). H_2O concentrations display less variability: discounting the three MIs that have clearly degassed (containing $\leq$0.4 wt% H_2O), MIs have a mean H_2O concentration of 1.1$\pm$0.2 wt% (Supporting Figure S6), which is comparable to H_2O concentrations obtained from other MER and EARS MIs (Iddon & Edmonds, 2020; Rooney et al., 2022).

Volatile saturation pressures of MIs are calculated using the fully thermodynamic MagmaSat volatile solubility model (Ghiorso & Gualda, 2015) via the Python 3 library VESIcal (Iacovino et al., 2021; Wieser et al., 2022); other volatile solubility models are considered and compared in the Supporting Information. Storage pressures for MIs for which total CO_2 contents are known (vapor bubble and glass), determined at a magmatic temperature of 1200 °C (Iddon et al., 2019; Wong et al., 2022), vary over a relatively narrow range from 2.5–4.5 kbar (Figure 2A). In the MER these pressures correspond to depths of ~10–15 km (assuming a crustal density of 2.7 g cm^{-3}), among the deepest recorded volatile saturation depths for continental rift magmas (Figure 2B-D). Pressures recorded by MIs without bubbles overlap partially with those that do have analyzed bubbles; however, the average CO_2 concentration and therefore pressure of MIs without a bubble is typically lower than those with a bubble. Two MIs for which only inclusion glass CO_2 is known record higher pressures in excess of 5 kbar (~20 km), corresponding to the MER lower crust. Overall, our barometric results show a relatively limited distribution of magma storage depths with a narrowly focused zone of intrusion centered at ~12 km depth, coincident with the seismically imaged boundary between the upper and lower crust in the MER (Maguire et al., 2006), and in close agreement with MI volatile saturation pressures from the Turkana Depression to the south of the MER (Figure 2C; Rooney et al., 2022).

3.2 Melt Inclusion Trace Element Compositions

The major element compositions of MIs overlap with carrier basalt (Supporting Figure S8) and whole-rock compositions of erupted lavas (Dataset S1; Tadesse et al., 2019; Nicotra et al., 2021). Incompatible trace element concentrations vary considerably in both MIs and lavas, but nonetheless still overlap (Figures 3A and B). Greater primary compositional variability is preserved in the MIs over the whole rocks, further evidenced by variations in trace element ratios that are not significantly affected by crystal fractionation, e.g., La/Yb and Dy/Yb (Figures 3C and D). While absolute trace element compositions can be achieved by melt fractionation from our most primitive MIs (Figures 3A and B), the scatter in trace element ratios cannot be replicated solely by fractionation of a common parental melt (Figures 3C and D).

By comparing CO_2 concentrations with trace elements with similar behavior during mantle melting (e.g., Ba, Rb), CO_2 degassing from mantle melts can be assessed (e.g., Le Voyer et al., 2018). While primary magmatic CO_2 contents are not known for MER magmas, the highest observed CO_2/Ba and CO_2/Rb ratios approach those measured in undegassed MORB (Le Voyer et al., 2018). Assuming that initial CO_2-trace element ratios are similar to those of MORB, CO_2/Ba and CO_2/Rb systematics for MER MIs clearly show evidence for degassing of CO_2 even in MIs with total CO_2 determinations (Figure 3E). Most melts therefore appear to have lost substantial volumes of CO_2 prior to MI entrapment (Figure 3E). If MORB ratios are reflective of primary CO_2/Ba and CO_2/Rb values in MER melts then initial CO_2 contents will be in the range of 1–4 wt% (mean of 2.0$\pm$0.6 wt% with the same CO_2/Ba as MORB), with ~60–95% of the CO_2 having been exsolved at mid-crustal pressures.

CO_2 degassing in the MER, likely derived from degassing of intruded mid-crustal magmas, is focused along discrete fault zones (Hunt et al., 2017). By making assumptions on the volumes of melt intruded into the crust (e.g., Iddon & Edmonds, 2020), we determine that the difference between expected CO_2 concentrations in primary mantle

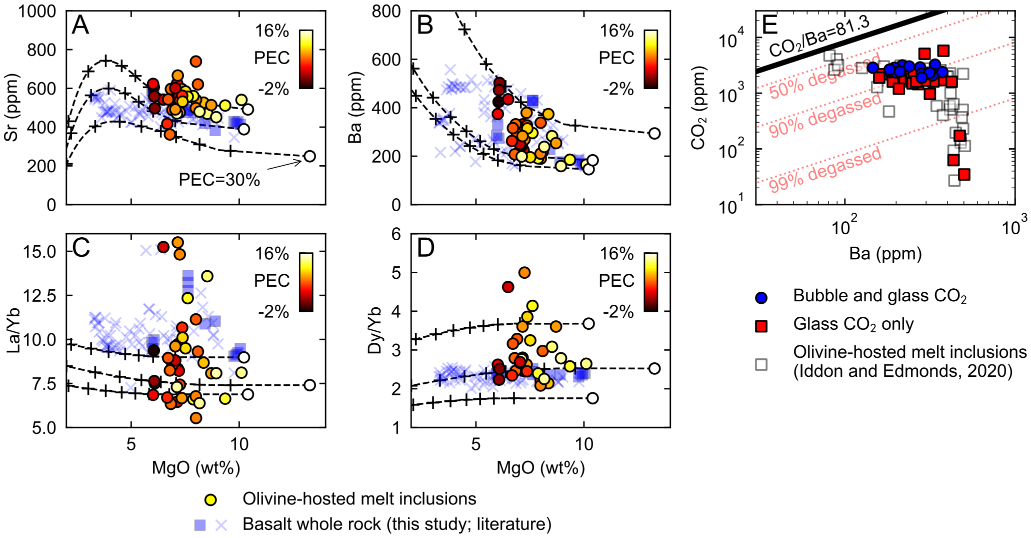

Figure 3. A–D. MI and whole-rock trace element and trace element ratios plotted against MgO (this study; Tadesse et al., 2019; Nicotra et al., 2021). Liquid lines of descent with crosses denoting 10% fractionation intervals are determined from our three highest MgO melts using Rhyolite-MELTS v1.2.0 (Gualda et al., 2012, see Supporting Information), assuming Rayleigh fractionation with the partition coefficients collated by Iddon and Edmonds (2020). PEC corrections are detailed in the Supporting Information. E. Olivine-hosted MI CO_2 plotted against Ba; primary CO_2/Ba of MORB (Le Voyer et al., 2018).

melts and those observed in our MIs is sufficient to generate the CO_2 fluxes measured from surface degassing (Figure 3E Hunt et al., 2017, see Supporting Information). The restriction of significant degassing to localized regions in the MER (Hunt et al., 2017) may suggest that some regions are subject to active intrusion at the present day whereas other portions are not; future studies should aim to constrain this periodicity of melt emplacement.

4 Discussion

4.1 Depths of Intrusion in the East African Rift

Our total CO_2 saturation pressures determined from vapor bubble and glass are in broad agreement with maximum pressures of melt storage estimated from MI volatiles at other EARS sectors (Figure 2B–D). Applying the same volatile solubility modelling performed on our MIs to literature datasets, we determine that our proposed 10–15 km depth range for basalt storage coincides with the deepest MIs at other parts of the EARS and Afar Rift (Figure 2C; e.g., A. Donovan et al., 2017; Rooney et al., 2022). Geophysical observations of crustal melt movement in other sectors of the EARS (Weinstein et al., 2017; Reiss et al., 2021, 2022) suggests that melt focusing at these pressures may be ubiquitous within the EARS.

The lack of evidence for significant melt storage within the upper crust in our dataset contrasts with the depth distributions for magma storage obtained from suites of MIs collected at large caldera-forming volcanic centers found along the MER (Figure 2; Iddon & Edmonds, 2020). Under these silicic centers, melt storage appears to extend upwards into the upper crust, where evolved magmas are generated via low pressure fractionation (Iddon & Edmonds, 2020). Notably, the maximum storage depths under caldera complexes in the EARS identified both from MI volatile saturation barometry (Figure 2; Iddon & Edmonds, 2020; Rooney et al., 2022) and from mineral barometry (Rooney et al., 2005; Iddon et al., 2019) coincides with the 10–15 km depth range observed in our dataset. This depth range may therefore be the locus of initial basaltic melt emplacement along the MER, with important implications for heat distribution within the rifting crust and therefore crustal strength profiles (Buck, 2006; Daniels et al., 2014; Lavecchia et al., 2016), such as the creation of a mid-crustal weak layer (Muluneh et al., 2020). With the exception of those below caldera complexes/silicic volcanoes (e.g., Biggs et al., 2011), upper crustal melt bodies (<10 km depth) in the MER are likely to be ephemeral, perhaps forming during periodic intrusive-eruptive episodes (e.g., Ebinger et al., 2013).

In contrast to the extensive MI data corresponding to mid-crustal pressures, very few MIs from our dataset and the MER dataset of Iddon and Edmonds (2020) record pressures corresponding to the lower crust or Moho (Figure 2; e.g., Maguire et al., 2006; Lavayssière et al., 2018). Considering the evolved compositions of our olivines (mean Fo_{80}) relative to Fo_{90} olivines in other MER volcanic materials (e.g., Rooney et al., 2005), we posit that an initial stage of fractionation near the Moho prior to ascent to mid-crustal pressures is necessary. This hypothesis is supported by low wavespeeds observed at Moho depths from the presence of melt in the heavily intruded lower crust (Keranen et al., 2009; Chambers et al., 2019, 2021), and numerical models suggesting that the lowermost crust is weak, hot and underlies a lower-crustal brittle-ductile transition at 20–25 km (Lavecchia et al., 2016; Muluneh et al., 2020). The absence of strong radial seismic anisotropy in the lower crust may also imply that melt storage at these depths may comprise both sills and isotropic bodies (Chambers et al., 2021). Melts pooling and fractionating at the base of the crust may bypass the ductile lowermost crust entirely if both density differences between melt and crust and lower crustal strain rates are sufficiently high (Muluneh et al., 2021).

4.2 Compositional Heterogeneity in Melt Inclusions

Variability in absolute trace element concentrations (Figures 3A and B) could result from fractional crystallization of distinct parental melts and/or mixing between variably fractionated melts with distinct origins. In contrast, the broader distribution of trace element ratios observed in MIs relative to whole rocks (Figures 3C and D) can only be inherited from the compositional heterogeneity of parental mantle-derived melts. Such variability may be derived from the melting of multiple source lithologies (e.g., Shorttle & Maclennan, 2011) and/or unmixed fractional mantle melts (e.g., Gurenko & Chaussidon, 1995).

Physical interactions between intrusive bodies therefore appear to be limited, and we infer that intruded magmas reside in a series of discrete sills emplaced at a common depth. The slightly lower degree of compositional diversity observed in erupted lavas (Figures 3C and D), even at higher MgO, suggests that some mixing does occur prior to eruption and that dyke intrusion into the upper crust may involve partially homogenized melts sourced from multiple mid-crustal sills. Erupted melts extend to lower MgO than the MIs (after PEC corrections), and pre-eruptive mixing and homogenization may therefore occur during a final stage of differentiation within upper crustal magma bodies.

4.3 Basaltic Melt Focusing in the Main Ethiopian Rift

The presence of melts intruded as mid-crustal sill complexes is strongly supported by geophysical observations of the present-day MER crust. Strong horizontally oriented seismic anisotropy observed in the MER at depths of 10–15 km is consistent with the presence of sills (Chambers et al., 2021). Low seismic moment earthquakes in northern MER magmatic segments are distributed within a narrow depth band between 8–16 km and have been interpreted as being triggered by movement or emplacement of mid-crustal melts (Keir et al., 2006; Daly et al., 2008). High Vp, high-Vp/Vs and high-density bodies are inferred to be present at these depths under Boku and other MER segments (Keranen et al., 2004; Cornwell et al., 2006; Daly et al., 2008), as are high-conductivity crustal anomalies (Whaler & Hautot, 2006), all indicative of partially molten intrusions in the mid-crust. Our results are also in good agreement with empirical observations relating MER cone clustering to melt intrusion depths (Mazzarini et al., 2013). In other words, the melt storage depths resolved directly using petrological methods are in very close agreement with the deepest intrusion pressures determined using geophysical techniques.

Focusing of ascending basaltic melts at this depth range can, to a first order, be attributed to MER crustal density structure as the mean density of the lower crust exceeds that of our MIs (mean of 2.71 g cm^{-3}, calculated after PEC corrections using DensityX, Iacovino and Till (2019); cf. e.g., Cornwell et al. (2006)). Driven by density differences, basaltic melts will rise to mid-crustal depths before they achieve neutral buoyancy, stall and crystallize. The upper crust, comparatively less dense than the lower crust, will limit the ascent of basalt melts beyond the focusing zone (Cornwell et al., 2006; Mickus et al., 2007).

Melt focusing in the mid-crust could also be attributed to the rheological structure of the crust. Numerical models based on seismic observations suggest that the 10–15 km depth range resolved using our MIs coincides with the weakest part of the Ethiopian crust, which is sandwiched between two strong brittle layers in the upper and mid-lower crust (Muluneh et al., 2020). The strong, lower-density brittle crust above this ductile zone, combined with the density limitations discussed above, likely inhibits further ascent of the buoyant melt (Cornwell et al., 2006; Muluneh et al., 2020). Melt may only progress directly to the surface through the breaking of dyke-induced faults (e.g., Casey et al., 2006), by exploiting pre-existing crustal weaknesses (e.g., Le Corvec et al., 2013), or after extensive fractionation to form lower-density silicic melts (e.g., Gleeson et al., 2017).

We therefore hypothesise that the intrusion and emplacement of melts into this weak, ductile mid-crust will have a strong effect on the overall rheology of the rifting crust, which in turn may govern how the crust locally accommodates strain in response to far-field extensional stresses. Ductile stretching may accommodate crustal deformation at a different rate or manner relative to the brittle layers above and below this weak zone, in turn possibly dictating that future batches of melt are focused in the same region. Indeed, the development of crustal sill systems in the MER may arise from pulsed emplacement of magmas from the lower crust or mantle (e.g., Annen et al., 2015). Stacked sills formed in this manner may maintain high localized temperatures in the crust, which can facilitate further intrusion of melt at shallower pressures, or may themselves contract during cooling to generate accommodation space for further intrusions (Magee et al., 2016). Future numerical or analog models of rift deformation in Ethiopia must account for the development of a hot, ductile, weak layer in the crust, and the influences such a layer may have on overall crustal rheology.

5 Summary

The results of our study are summarized in Figure 4. Through the careful analysis of major, trace, and volatile elements in olivine-hosted MIs, we propose that stacked mid-crustal sills in the depth range of 10–15 km are the dominant form of magmatic storage in the MER (Figures 4A and B). These sills are known to be horizontally oriented from seismic anisotropy (Chambers et al., 2019), and develop as a consequence of repeated magmatic intrusion into the mid-crust during the progression of late-stage continental rifting. Initially crystallizing at or near the Moho, mantle-derived magmas bypass the ductile lowermost crust to arrive at the Ethiopian mid-crust, heralded by seismic activity during emplacement (Figure 4C). These melts are stored as discrete sills in the weak,

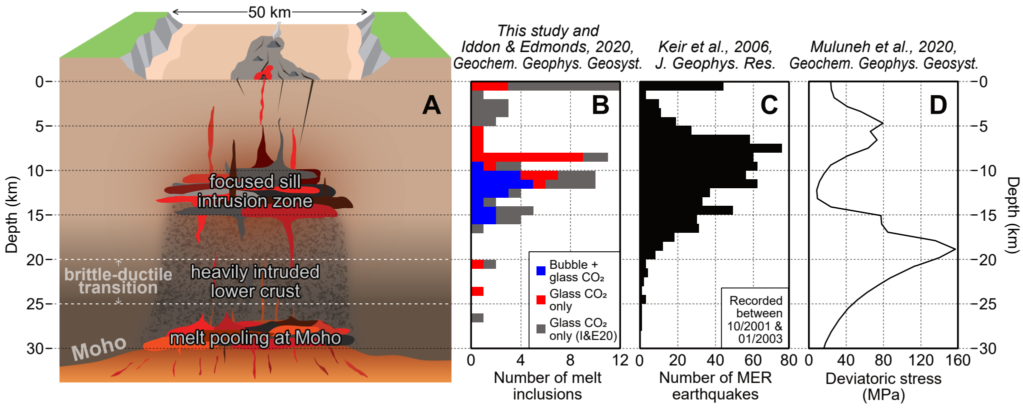

Figure 4. A. Summary cartoon illustrating our proposed structure of the MER crust. Horizontal and vertical dimensions not to same scale. B. Histogram of MER olivine-hosted MI saturation pressures (this study; Iddon & Edmonds, 2020). C. Histogram of MER earthquakes recorded between October 2001 and January 2003 (Keir et al., 2006; Daly et al., 2008, selection criteria in Supporting Figure S9). D. Numerical model of MER crustal deviatoric stress (Muluneh et al., 2020).

ductile mid-crust and blocked from further ascent by a strong, lower density upper crust (Figure 4D). The diverse range of trace element ratios observed in MIs gives evidence to limited melt mixing in the crust; partial mixing of magmas between sills may occur in the shallow crust prior to eruption (Figure 3). Petrological evidence for mid-crustal sills in the MER presented in this study is in agreement with geophysical observations (e.g., Keranen et al., 2004), and the volatile composition of basalts comprising these bodies are consistent with CO_2 degassing rates measured at the rift floor (Hunt et al., 2017). The presence of hot sills in the MER mid-crust has important implications for how intruding melts in late-stage rifts affect and are affected by the rheological structure of the crust, and should be considered a key element in future development of models of continental rifting.

6 Open Research

The complete dataset of geochemical analyses and melt inclusion microscope photographs is available within a Zenodo repository (`doi.org/10.5281/zenodo.7236254`).

Acknowledgments

KW and PW are funded by NERC DTP studentships NE/L002574/1 and NE/L002507/1 respectively. KW acknowledges additional financial support from the Geologists' Association New Researchers Award. Ion probe analyses are funded through NERC grant IMF694/1119 awarded to DF. ME acknowledges the support of COMET via NERC. We thank Cristina Talavera Rodriguez and Lesley Neve for performing geochemical analyses on our behalf during the COVID-19 pandemic. Yared Sinetebeb, Harri Wyn Williams, Emilie Ringe, and Richard Walshaw are thanked for assistance with fieldwork, sample preparation, Raman spectroscopy, and EPMA respectively. We acknowledge thought-provoking discussions with Ian Bastow, Emma Chambers, Tim Craig, Sophie Hautot, Derek Keir, Tyrone Rooney, and Kathy Whaler. Finally, we acknowledge the Ethiopian Ministry of Mines and Oromia State Administration for sampling and field permissions.

References

Allison, C. M., Roggensack, K., & Clarke, A. B. (2019, June). H_2O–CO_2 solubility in alkali-rich mafic magmas: new experiments at mid-crustal pressures. *Contributions to Mineralogy and Petrology*, *174*(7), 58. Retrieved 2022-02-01, from `https://doi.org/10.1007/s00410-019-1592-4` doi: 10.1007/s00410-019-1592-4

Annen, C., Blundy, J. D., Leuthold, J., & Sparks, R. S. J. (2015, August). Construction and evolution of igneous bodies: Towards an integrated perspective of crustal magmatism. *Lithos*, *230*, 206–221. Retrieved 2022-12-09, from `https://www.sciencedirect.com/science/article/pii/S0024493715001759` doi: 10.1016/j.lithos.2015.05.008

Armitage, J. J., Ferguson, D. J., Goes, S., Hammond, J. O. S., Calais, E., Rychert, C. A., & Harmon, N. (2015, May). Upper mantle temperature and the onset of extension and break-up in Afar, Africa. *Earth and Planetary Science Letters*, *418*, 78–90. Retrieved 2018-10-03, from `http://www.sciencedirect.com/science/article/pii/S0012821X15001259` doi: 10.1016/j.epsl.2015.02.039

Bastow, I. D., & Keir, D. (2011, April). The protracted development of the continent–ocean transition in Afar. *Nature Geoscience*, *4*(4), 248–250. Retrieved 2018-05-16, from `https://www.nature.com/articles/ngeo1095` doi: 10.1038/ngeo1095

Bastow, I. D., Keir, D., & Daly, E. (2011, June). The Ethiopia Afar Geoscientific Lithospheric Experiment (EAGLE): Probing the transition from continental rifting to incipient seafloor spreading. In *Geological Society of America Special Papers* (Vol. 478, pp. 51–76). Geological Society of America. Retrieved 2018-10-26, from `https://pubs.geoscienceworld.org/books/book/653/chapter/3806991/` doi: 10.1130/2011.2478(04)

Bastow, I. D., Pilidou, S., Kendall, J.-M., & Stuart, G. W. (2010, June). Melt-induced seismic anisotropy and magma assisted rifting in Ethiopia: Evidence from surface waves. *Geochemistry, Geophysics, Geosystems*, *11*(6). Retrieved 2018-11-02, from `https://agupubs.onlinelibrary.wiley.com/doi/full/10.1029/2010GC003036` doi: 10.1029/2010GC003036

Bialas, R. W., Buck, W. R., & Qin, R. (2010, March). How much magma is required to rift a continent? *Earth and Planetary Science Letters*, *292*(1), 68–78. Retrieved 2022-11-29, from `https://www.sciencedirect.com/science/article/pii/S0012821X10000555` doi: 10.1016/j.epsl.2010.01.021

Biggs, J., Bastow, I. D., Keir, D., & Lewi, E. (2011, September). Pulses of deformation reveal frequently recurring shallow magmatic activity beneath the Main Ethiopian Rift. *Geochemistry, Geophysics, Geosystems*, *12*(9). Retrieved 2019-02-05, from `https://agupubs.onlinelibrary.wiley.com/doi/full/10.1029/2011GC003662` doi: 10.1029/2011GC003662

Blundy, J. D., & Wood, B. J. (1991, January). Crystal-chemical controls on the partitioning of Sr and Ba between plagioclase feldspar, silicate melts, and hydrothermal solutions. *Geochimica et Cosmochimica Acta*, *55*(1), 193–209. Retrieved 2017-05-25, from `http://www.sciencedirect.com/science/article/pii/001670379190411W` doi: 10.1016/0016-7037(91)90411-W

Buck, W. R. (2006, January). The role of magma in the development of the Afro-Arabian Rift System. In G. Yirgu, C. Ebinger, & P. K. H. Maguire (Eds.), *The Afar Volcanic Province within the East African Rift System* (Vol. 259, pp. 43–54). Retrieved 2018-11-05, from `http://sp.lyellcollection.org/content/259/1/43`

Casey, M., Ebinger, C., Keir, D., Gloaguen, R., & Mohamed, F. (2006, January). Strain accommodation in transitional rifts: extension by magma intrusion and faulting in Ethiopian rift magmatic segments. In G. Yirgu, C. J. Ebinger, & P. K. H. Maguire (Eds.), *The Afar Volcanic Province within the East African Rift System* (Vol. 259, pp. 143–163). Retrieved 2018-09-23, from http://sp.lyellcollection.org/content/259/1/143

Chambers, E. L., Harmon, N., Keir, D., & Rychert, C. A. (2019, April). Using Ambient Noise to Image the Northern East African Rift. *Geochemistry, Geophysics, Geosystems*, *20*(4), 2091–2109. Retrieved 2019-06-21, from https://agupubs.onlinelibrary.wiley.com/doi/full/10.1029/2018GC008129 doi: 10.1029/2018GC008129

Chambers, E. L., Harmon, N., Rychert, C. A., & Keir, D. (2021, November). Variations in melt emplacement beneath the northern East African Rift from radial anisotropy. *Earth and Planetary Science Letters*, *573*, 117150. Retrieved 2021-11-03, from https://linkinghub.elsevier.com/retrieve/pii/S0012821X21004052 doi: 10.1016/j.epsl.2021.117150

Cornwell, D. G., Mackenzie, G. D., England, R. W., Maguire, P. K. H., Asfaw, L. M., & Oluma, B. (2006, January). Northern Main Ethiopian Rift crustal structure from new high-precision gravity data. In *The Afar Volcanic Province within the East African Rift System* (Vol. 259, pp. 307–321). Retrieved 2018-11-14, from http://sp.lyellcollection.org/content/259/1/307

Daly, E., Keir, D., Ebinger, C. J., Stuart, G. W., Bastow, I. D., & Ayele, A. (2008, March). Crustal tomographic imaging of a transitional continental rift: The Ethiopian rift. *Geophysical Journal International*, *172*(3), 1033–1048. Retrieved 2018-11-01, from https://academic.oup.com/gji/article/172/3/1033/571185 doi: 10.1111/j.1365-246X.2007.03682.x

Daniels, K. A., Bastow, I. D., Keir, D., Sparks, R. S. J., & Menand, T. (2014, January). Thermal models of dyke intrusion during development of continent–ocean transition. *Earth and Planetary Science Letters*, *385*, 145–153. Retrieved 2018-11-22, from http://www.sciencedirect.com/science/article/pii/S0012821X13005293 doi: 10.1016/j.epsl.2013.09.018

Danyushevsky, L. V. (2001, October). The effect of small amounts of H_2O on crystallisation of mid-ocean ridge and backarc basin magmas. *Journal of Volcanology and Geothermal Research*, *110*(3), 265–280. Retrieved 2021-03-30, from https://www.sciencedirect.com/science/article/pii/S037702730100213X doi: 10.1016/S0377-0273(01)00213-X

Danyushevsky, L. V., & Plechov, P. (2011, July). Petrolog3: Integrated software for modeling crystallization processes. *Geochemistry, Geophysics, Geosystems*, *12*(7), Q07021. Retrieved 2017-12-02, from http://onlinelibrary.wiley.com/doi/10.1029/2011GC003516/abstract doi: 10.1029/2011GC003516

DeVitre, C. L., Barth, A., Gazel, E., Plank, T. A., & Ramalho, R. (2021, December). Solving the Carbonate Problem in Melt Inclusion Bubbles. In *AGU Fall Meeting Abstracts.* Retrieved from https://agu.confex.com/agu/fm21/meetingapp.cgi/Paper/845682

DeVitre, C. L., Dayton, K., Gazel, E., Barth, A., Plank, T. A., Pamukcu, A., … Monteleone, B. (2022, July). Accounting for Multi-Phase Carbon in Melt Inclusion Bubbles. In *Goldschmidt Conference Abstracts.* Retrieved 2022-08-08, from https://conf.goldschmidt.info/goldschmidt/2022/meetingapp.cgi/Paper/12601

Dixon, J. E. (1997, April). Degassing of alkalic basalts. *American Mineralogist*, *82*(3-4), 368–378. Retrieved 2022-01-05, from https://pubs.geoscienceworld.org/ammin/article/82/3-4/368-378/43291 doi: 10.2138/am-1997-3-415

Dixon, J. E., Stolper, E. M., & Holloway, J. R. (1995, December). An Experimental Study of Water and Carbon Dioxide Solubilities in Mid-Ocean Ridge Basaltic Liquids. Part I: Calibration and Solubility Models. *Journal of Petrology*, *36*(6), 1607–1631. Retrieved 2019-04-08, from https://academic.oup.com/petrology/article/36/6/1607/1493308 doi: 10.1093/oxfordjournals.petrology.a037267

Donovan, A., Blundy, J., Oppenheimer, C., & Buisman, I. (2017, November). The

2011 eruption of Nabro volcano, Eritrea: perspectives on magmatic processes from melt inclusions. *Contributions to Mineralogy and Petrology*, *173*(1), 1. Retrieved 2022-01-17, from https://doi.org/10.1007/s00410-017-1425-2 doi: 10.1007/s00410-017-1425-2

Donovan, J. J. (2021). *Probe for EPMA v. 13.0.5 User's Guide and Reference (Xtreme Edition).* Retrieved 2022-06-07, from https://probesoftware.com/download/PROBEWIN.pdf

Ebinger, C. J., Keir, D., Ayele, A., Calais, E., Wright, T. J., Belachew, M., ... Buck, W. R. (2008, September). Capturing magma intrusion and faulting processes during continental rupture: Seismicity of the Dabbahu (Afar) rift. *Geophysical Journal International*, *174*(3), 1138–1152. Retrieved 2021-02-01, from https://doi.org/10.1111/j.1365-246X.2008.03877.x doi: 10.1111/j.1365-246X.2008.03877.x

Ebinger, C. J., van Wijk, J., & Keir, D. (2013, September). The time scales of continental rifting: Implications for global processes. In *Geological Society of America Special Papers* (Vol. 500, pp. 371–396). Geological Society of America. Retrieved 2018-05-18, from https://pubs.geoscienceworld.org/books/book/671/chapter/3807783/ doi: 10.1130/2013.2500(11)

Field, L., Barnie, T., Blundy, J., Brooker, R. A., Keir, D., Lewi, E., & Saunders, K. (2012, December). Integrated field, satellite and petrological observations of the November 2010 eruption of Erta Ale. *Bulletin of Volcanology*, *74*(10), 2251–2271. Retrieved 2019-08-21, from https://doi.org/10.1007/s00445-012-0660-7 doi: 10.1007/s00445-012-0660-7

Field, L., Blundy, J., Brooker, R. A., Wright, T., & Yirgu, G. (2012, July). Magma storage conditions beneath Dabbahu Volcano (Ethiopia) constrained by petrology, seismicity and satellite geodesy. *Bulletin of Volcanology*, *74*(5), 981–1004. Retrieved 2019-02-05, from http://link.springer.com/10.1007/s00445-012-0580-6 doi: 10.1007/s00445-012-0580-6

Foley, S. F., & Fischer, T. P. (2017, December). An essential role for continental rifts and lithosphere in the deep carbon cycle. *Nature Geoscience*, *10*(12), 897–902. Retrieved 2018-07-18, from https://www.nature.com/articles/s41561-017-0002-7 doi: 10.1038/s41561-017-0002-7

Ghiorso, M. S., & Gualda, G. A. R. (2015, June). An H_2O–CO_2 mixed fluid saturation model compatible with rhyolite-MELTS. *Contributions to Mineralogy and Petrology*, *169*(6), 53. Retrieved 2021-11-25, from https://doi.org/10.1007/s00410-015-1141-8 doi: 10.1007/s00410-015-1141-8

Gleeson, M. L. M., Stock, M. J., Pyle, D. M., Mather, T. A., Hutchison, W., Yirgu, G., & Wade, J. (2017, May). Constraining magma storage conditions at a restless volcano in the Main Ethiopian Rift using phase equilibria models. *Journal of Volcanology and Geothermal Research*, *337*, 44–61. Retrieved 2018-10-24, from http://www.sciencedirect.com/science/article/pii/S0377027316304383 doi: 10.1016/j.jvolgeores.2017.02.026

Gualda, G. A. R., Ghiorso, M. S., Lemons, R. V., & Carley, T. L. (2012, May). Rhyolite-MELTS: a Modified Calibration of MELTS Optimized for Silica-rich, Fluid-bearing Magmatic Systems. *Journal of Petrology*, *53*(5), 875–890. Retrieved 2021-03-24, from https://doi.org/10.1093/petrology/egr080 doi: 10.1093/petrology/egr080

Gurenko, A. A., & Chaussidon, M. (1995, July). Enriched and depleted primitive melts included in olivine from Icelandic tholeiites: origin by continuous melting of a single mantle column. *Geochimica et Cosmochimica Acta*, *59*(14), 2905–2917. Retrieved 2021-12-09, from https://www.sciencedirect.com/science/article/pii/0016703795001840 doi: 10.1016/0016-7037(95)00184-0

Hartley, M. E., Maclennan, J., Edmonds, M., & Thordarson, T. (2014, May). Reconstructing the deep CO_2 degassing behaviour of large basaltic fissure eruptions. *Earth and Planetary Science Letters*, *393*, 120–131. Retrieved 2018-02-16, from http://www.sciencedirect.com/science/article/pii/S0012821X14001125 doi: 10.1016/j.epsl.2014.02.031

Hauri, E., Wang, J., Dixon, J. E., King, P. L., Mandeville, C., & Newman, S. (2002, March). SIMS analysis of volatiles in silicate glasses: 1. Calibration, matrix effects and comparisons with FTIR. *Chemical Geology*, *183*(1), 99–114. Retrieved 2022-02-21, from https://www.sciencedirect.com/science/article/pii/S0009254101003758 doi: 10.1016/S0009-2541(01)00375-8

Head, E. M., Shaw, A. M., Wallace, P. J., Sims, K. W. W., & Carn, S. A. (2011). Insight into volatile behavior at Nyamuragira volcano (D.R. Congo, Africa) through olivine-hosted melt inclusions. *Geochemistry, Geophysics, Geosystems*, *12*(10). Retrieved 2022-01-17, from https://onlinelibrary.wiley.com/doi/abs/10.1029/2011GC003699 (_eprint: https://onlinelibrary.wiley.com/doi/pdf/10.1029/2011GC003699) doi: 10.1029/2011GC003699

Hudgins, T. R., Mukasa, S. B., Simon, A. C., Moore, G., & Barifaijo, E. (2015, April). Melt inclusion evidence for CO_2-rich melts beneath the western branch of the East African Rift: implications for long-term storage of volatiles in the deep lithospheric mantle. *Contributions to Mineralogy and Petrology*, *169*(5), 46. Retrieved 2020-09-15, from https://doi.org/10.1007/s00410-015-1140-9 doi: 10.1007/s00410-015-1140-9

Hunt, J. A., Zafu, A., Mather, T. A., Pyle, D. M., & Barry, P. H. (2017, October). Spatially Variable CO_2 Degassing in the Main Ethiopian Rift: Implications for Magma Storage, Volatile Transport, and Rift-Related Emissions. *Geochemistry, Geophysics, Geosystems*, *18*(10), 3714–3737. Retrieved 2018-08-07, from https://agupubs.onlinelibrary.wiley.com/doi/abs/10.1002/2017GC006975 doi: 10.1002/2017GC006975

Iacono-Marziano, G., Morizet, Y., Le Trong, E., & Gaillard, F. (2012, November). New experimental data and semi-empirical parameterization of H_2O–CO_2 solubility in mafic melts. *Geochimica et Cosmochimica Acta*, *97*, 1–23. Retrieved 2020-02-17, from http://www.sciencedirect.com/science/article/pii/S0016703712004930 doi: 10.1016/j.gca.2012.08.035

Iacovino, K., Matthews, S., Wieser, P. E., Moore, G. M., & Bégué, F. (2021). VESIcal Part I: An Open-Source Thermodynamic Model Engine for Mixed Volatile (H_2O-CO_2) Solubility in Silicate Melts. *Earth and Space Science*, *8*(11), e2020EA001584. Retrieved 2021-11-16, from https://onlinelibrary.wiley.com/doi/abs/10.1029/2020EA001584 (_eprint: https://onlinelibrary.wiley.com/doi/pdf/10.1029/2020EA001584) doi: 10.1029/2020EA001584

Iacovino, K., & Till, C. B. (2019, February). DensityX: A program for calculating the densities of magmatic liquids up to 1,627 °C and 30 kbar. *Volcanica*, *2*(1), 1–10. Retrieved 2021-03-04, from http://jvolcanica.org/ojs/index.php/volcanica/article/view/12 (Number: 1) doi: 10.30909/vol.02.01.0110

Iddon, F., & Edmonds, M. (2020). Volatile-Rich Magmas Distributed Through the Upper Crust in the Main Ethiopian Rift. *Geochemistry, Geophysics, Geosystems*, *21*(6), e2019–GC008904. Retrieved 2020-06-24, from https://agupubs.onlinelibrary.wiley.com/doi/abs/10.1029/2019GC008904 (_eprint: https://agupubs.onlinelibrary.wiley.com/doi/pdf/10.1029/2019GC008904) doi: 10.1029/2019GC008904

Iddon, F., Jackson, C., Hutchison, W., Fontijn, K., Pyle, D. M., Mather, T. A., … Edmonds, M. (2019). Mixing and Crystal Scavenging in the Main Ethiopian Rift Revealed by Trace Element Systematics in Feldspars and Glasses. *Geochemistry, Geophysics, Geosystems*, *20*(1), 230–259. Retrieved 2019-10-02, from https://agupubs.onlinelibrary.wiley.com/doi/abs/10.1029/2018GC007836 doi: 10.1029/2018GC007836

Jarosewich, E. (2002). Smithsonian Microbeam Standards. *Journal of Research* *of the National Institute of Standards and Technology*, *107*(6), 681–685. Retrieved 2022-02-21, from https://www.ncbi.nlm.nih.gov/pmc/articles/PMC4863845/ doi: 10.6028/jres.107.054

Jochum, K. P., Stoll, B., Herwig, K., Willbold, M., Hofmann, A. W., Amini, M., … Woodhead, J. D. (2006). MPI-DING reference glasses for in situ microanalysis: New reference values for element concentrations and isotope ratios. *Geochemistry, Geophysics, Geosystems*, *7*(2). Retrieved 2021-06-15, from https://agupubs.onlinelibrary.wiley.com/doi/abs/10.1029/2005GC001060 (_eprint: https://agupubs.onlinelibrary.wiley.com/doi/pdf/10.1029/2005GC001060) doi: 10.1029/2005GC001060

Keir, D., Ebinger, C. J., Stuart, G. W., Daly, E., & Ayele, A. (2006, May). Strain accommodation by magmatism and faulting as rifting proceeds to breakup: Seismicity of the northern Ethiopian rift. *Journal of Geophysical Research: Solid Earth*, *111*(B5). Retrieved 2018-11-01, from https://agupubs.onlinelibrary.wiley.com/doi/full/10.1029/2005JB003748 doi: 10.1029/2005JB003748

Kendall, J.-M., Stuart, G. W., Ebinger, C. J., Bastow, I. D., & Keir, D. (2005, January). Magma-assisted rifting in Ethiopia. *Nature*, *433*(7022), 146–148. Retrieved 2018-04-11, from https://www.nature.com/articles/nature03161 doi: 10.1038/nature03161

Keranen, K. M., Klemperer, S. L., Gloaguen, R., & EAGLE Working Group. (2004). Three-dimensional seismic imaging of a protoridge axis in the Main Ethiopian rift. *Geology*, *32*(11), 949. Retrieved 2018-11-01, from https://pubs.geoscienceworld.org/geology/article/32/11/949-952/103645 doi: 10.1130/G20737.1

Keranen, K. M., Klemperer, S. L., Julia, J., Lawrence, J. F., & Nyblade, A. A. (2009, May). Low lower crustal velocity across Ethiopia: Is the Main Ethiopian Rift a narrow rift in a hot craton? *Geochemistry, Geophysics, Geosystems*, *10*(5). Retrieved 2018-11-05, from https://agupubs.onlinelibrary.wiley.com/doi/abs/10.1029/2008GC002293 doi: 10.1029/2008GC002293

Lamadrid, H., Moore, L., Moncada, D., Rimstidt, J., Burruss, R., & Bodnar, R. (2017, February). Reassessment of the Raman CO_2 densimeter. *Chemical Geology*, *450*, 210–222. Retrieved 2020-02-09, from https://linkinghub.elsevier.com/retrieve/pii/S0009254116306945 doi: 10.1016/j.chemgeo.2016.12.034

Lavayssière, A., Rychert, C., Harmon, N., Keir, D., Hammond, J. O. S., Kendall, J.-M., … Leroy, S. (2018, October). Imaging Lithospheric Discontinuities Beneath the Northern East African Rift Using S-to-P Receiver Functions. *Geochemistry, Geophysics, Geosystems*. Retrieved 2018-11-19, from https://agupubs.onlinelibrary.wiley.com/doi/abs/10.1029/2018GC007463 doi: 10.1029/2018GC007463

Lavecchia, A., Beekman, F., Clark, S. R., & Cloetingh, S. A. P. L. (2016, August). Thermo-rheological aspects of crustal evolution during continental breakup and melt intrusion: The Main Ethiopian Rift, East Africa. *Tectonophysics*, *686*, 51–62. Retrieved 2022-06-01, from https://www.sciencedirect.com/science/article/pii/S0040195116302840 doi: 10.1016/j.tecto.2016.07.018

Le Corvec, N., Menand, T., & Lindsay, J. (2013). Interaction of ascending magma with pre-existing crustal fractures in monogenetic basaltic volcanism: an experimental approach. *Journal of Geophysical Research: Solid Earth*, *118*(3), 968–984. Retrieved 2022-11-25, from https://onlinelibrary.wiley.com/doi/abs/10.1002/jgrb.50142 (_eprint: https://onlinelibrary.wiley.com/doi/pdf/10.1002/jgrb.50142) doi: 10.1002/jgrb.50142

Lee, H., Muirhead, J. D., Fischer, T. P., Ebinger, C. J., Kattenhorn, S. A., Sharp,

Z. D., & Kianji, G. (2016, February). Massive and prolonged deep carbon emissions associated with continental rifting. *Nature Geoscience*, *9*(2), 145–149. Retrieved 2018-07-25, from `https://www.nature.com/articles/ngeo2622` doi: 10.1038/ngeo2622

Le Voyer, M., Hauri, E. H., Cottrell, E., Kelley, K. A., Salters, V. J. M., Langmuir, C. H., ... Füri, E. (2018). Carbon fluxes and primary magma CO_2 contents along the global mid-ocean ridge system. *Geochemistry, Geophysics, Geosystems*, *20*(3), 1387–1424. Retrieved 2018-12-03, from `https://agupubs.onlinelibrary.wiley.com/doi/abs/10.1029/2018GC007630` doi: 10.1029/2018GC007630

Maclennan, J. (2017, February). Bubble formation and decrepitation control the CO_2 content of olivine-hosted melt inclusions. *Geochemistry, Geophysics, Geosystems*, *18*(2), 597–616. Retrieved 2018-11-14, from `https://agupubs.onlinelibrary.wiley.com/doi/abs/10.1002/2016GC006633` doi: 10.1002/2016GC006633

Magee, C., Muirhead, J. D., Karvelas, A., Holford, S. P., Jackson, C. A., Bastow, I. D., ... Shtukert, O. (2016, June). Lateral magma flow in mafic sill complexes. *Geosphere*, *12*(3), 809–841. Retrieved 2022-05-09, from `https://doi.org/10.1130/GES01256.1` doi: 10.1130/GES01256.1

Maguire, P., Keller, G., Klemperer, S., Mackenzie, G., Keranen, K., Harder, S., ... Amha, M. (2006). Crustal structure of the northern Main Ethiopian Rift from the EAGLE controlled-source survey; a snapshot of incipient lithospheric break-up. In *The Afar Volcanic Province within the East African Rift System* (Vol. 259, pp. 269–292). Retrieved 2018-11-26, from `http://sp.lyellcollection.org/lookup/doi/10.1144/GSL.SP.2006.259.01.21`

Mazzarini, F., Rooney, T. O., & Isola, I. (2013, January). The intimate relationship between strain and magmatism: A numerical treatment of clustered monogenetic fields in the Main Ethiopian Rift. *Tectonics*, *32*(1), 49–64. Retrieved 2018-11-13, from `http://doi.wiley.com/10.1029/2012TC003146` doi: 10.1029/2012TC003146

Mickus, K., Tadesse, K., Keller, G. R., & Oluma, B. (2007, June). Gravity analysis of the main Ethiopian rift. *Journal of African Earth Sciences*, *48*(2), 59–69. Retrieved 2021-11-30, from `https://www.sciencedirect.com/science/article/pii/S1464343X07000192` doi: 10.1016/j.jafrearsci.2007.02.008

Moore, L. R., Gazel, E., Tuohy, R., Lloyd, A. S., Esposito, R., Steele-MacInnis, M., ... Bodnar, R. J. (2015, April). Bubbles matter: An assessment of the contribution of vapor bubbles to melt inclusion volatile budgets. *American Mineralogist*, *100*(4), 806–823. Retrieved 2019-05-13, from `https://pubs.geoscienceworld.org/ammin/article/100/4/806-823/40390` doi: 10.2138/am-2015-5036

Moore, L. R., Mironov, N., Portnyagin, M., Gazel, E., & Bodnar, R. J. (2018, June). Volatile contents of primitive bubble-bearing melt inclusions from Klyuchevskoy volcano, Kamchatka: Comparison of volatile contents determined by mass-balance versus experimental homogenization. *Journal of Volcanology and Geothermal Research*, *358*, 124–131. Retrieved 2022-08-25, from `https://www.sciencedirect.com/science/article/pii/S0377027317306510` doi: 10.1016/j.jvolgeores.2018.03.007

Muluneh, A. A., Brune, S., Illsley-Kemp, F., Corti, G., Keir, D., Glerum, A., ... Mori, J. (2020). Mechanism for Deep Crustal Seismicity: Insight From Modeling of Deformation Processes at the Main Ethiopian Rift. *Geochemistry, Geophysics, Geosystems*, *21*(7), e2020GC008935. Retrieved 2022-06-01, from `https://onlinelibrary.wiley.com/doi/abs/10.1029/2020GC008935` (_eprint: https://onlinelibrary.wiley.com/doi/pdf/10.1029/2020GC008935) doi: 10.1029/2020GC008935

Muluneh, A. A., Keir, D., & Corti, G. (2021). Thermo-Rheological Properties of the Ethiopian Lithosphere and Evidence for Transient Fluid Induced Lower Crustal Seismicity Beneath the Ethiopian Rift. *Frontiers in Earth Science*, *9*. Retrieved 2022-06-01, from https://www.frontiersin.org/article/10.3389/feart.2021.610165

Neave, D. A., Fabbro, G., Herd, R. A., Petrone, C. M., & Edmonds, M. (2012, March). Melting, Differentiation and Degassing at the Pantelleria Volcano, Italy. *Journal of Petrology*, *53*(3), 637–663. Retrieved 2019-02-05, from https://academic.oup.com/petrology/article/53/3/637/1613886 doi: 10.1093/petrology/egr074

Newman, S., & Lowenstern, J. B. (2002, June). VolatileCalc: a silicate melt–H_2O–CO_2 solution model written in Visual Basic for excel. *Computers & Geosciences*, *28*(5), 597–604. Retrieved 2021-02-01, from http://www.sciencedirect.com/science/article/pii/S0098300401000814 doi: 10.1016/S0098-3004(01)00081-4

Nicotra, E., Viccaro, M., Donato, P., Acocella, V., & De Rosa, R. (2021, November). Catching the Main Ethiopian Rift evolving towards plate divergence. *Scientific Reports*, *11*(1), 21821. Retrieved 2021-11-09, from https://www.nature.com/articles/s41598-021-01259-6 (Bandiera_abtest: a Cc_license_type: cc_by Cg_type: Nature Research Journals Number: 1 Primary_atype: Research Publisher: Nature Publishing Group Subject_term: Petrology;Tectonics;Volcanology Subject_term_id: petrology;tectonics;volcanology) doi: 10.1038/s41598-021-01259-6

Oliveira, M. E., Gomes, A. S., Rosas, F. M., Duarte, J. C., França, G. S., Almeida, J. C., & Fuck, R. A. (2022, May). Impact of crustal rheology and inherited mechanical weaknesses on early continental rifting and initial evolution of double graben structural configurations: Insights from 2D numerical models. *Tectonophysics*, *831*, 229281. Retrieved 2022-12-10, from https://www.sciencedirect.com/science/article/pii/S0040195122000750 doi: 10.1016/j.tecto.2022.229281

Rasmussen, D. J., Plank, T. A., Wallace, P. J., Newcombe, M. E., & Lowenstern, J. B. (2020, December). Vapor-bubble growth in olivine-hosted melt inclusions. *American Mineralogist*, *105*(12), 1898–1919. Retrieved 2021-03-03, from https://pubs.geoscienceworld.org/msa/ammin/article/105/12/1898/592851/Vapor-bubble-growth-in-olivine-hosted-melt (Publisher: GeoScienceWorld) doi: 10.2138/am-2020-7377

Reiss, M. C., De Siena, L., & Muirhead, J. D. (2022). The Interconnected Magmatic Plumbing System of the Natron Rift. *Geophysical Research Letters*, *49*(15), e2022GL098922. Retrieved 2022-11-24, from https://onlinelibrary.wiley.com/doi/abs/10.1029/2022GL098922 (_eprint: https://onlinelibrary.wiley.com/doi/pdf/10.1029/2022GL098922) doi: 10.1029/2022GL098922

Reiss, M. C., Muirhead, J. D., Laizer, A., Link, F., Kazimoto, E., Ebinger, C. J., & Rümpker, G. (2021, February). The Impact of Complex Volcanic Plumbing on the Nature of Seismicity in the Developing Magmatic Natron Rift, Tanzania. *Frontiers in Earth Science*, *8*. doi: 10.3389/feart.2020.609805

Rooney, T. O., Bastow, I. D., & Keir, D. (2011, April). Insights into extensional processes during magma assisted rifting: Evidence from aligned scoria cones. *Journal of Volcanology and Geothermal Research*, *201*(1), 83–96. Retrieved 2018-02-02, from http://www.sciencedirect.com/science/article/pii/S0377027310002386 doi: 10.1016/j.jvolgeores.2010.07.019

Rooney, T. O., Furman, T., Yirgu, G., & Ayalew, D. (2005, August). Structure of the Ethiopian lithosphere: Xenolith evidence in the Main Ethiopian Rift. *Geochimica et Cosmochimica Acta*, *69*(15), 3889–3910. Retrieved 2018-10-25, from http://www.sciencedirect.com/science/article/pii/S0016703705003042 doi: 10.1016/j.gca.2005.03.043

Rooney, T. O., Wallace, P. J., Muirhead, J. D., Chiasera, B., Steiner, R. A., Girard, G., & Karson, J. A. (2022, November). Transition to magma-driven rifting in the South Turkana Basin, Kenya: Part 2. *Journal of the Geological Society*, *179*(6), jgs2021–160. Retrieved 2022-10-31, from https://www.lyellcollection.org/doi/10.1144/jgs2021-160 doi: 10.1144/jgs2021-160

Saria, E., Calais, E., Stamps, D. S., Delvaux, D., & Hartnady, C. J. H. (2014, March). Present-day kinematics of the East African Rift. *Journal of Geophysical Research: Solid Earth*, *119*(4), 3584–3600. Retrieved 2018-11-01, from https://agupubs.onlinelibrary.wiley.com/doi/full/10.1002/2013JB010901 doi: 10.1002/2013JB010901

Schneider, C. A., Rasband, W. S., & Eliceiri, K. W. (2012, July). NIH Image to ImageJ: 25 years of image analysis. *Nature Methods*, *9*(7), 671–675. Retrieved 2021-03-17, from https://www.nature.com/articles/nmeth.2089 (Number: 7 Publisher: Nature Publishing Group) doi: 10.1038/nmeth.2089

Shishkina, T., Botcharnikov, R., Holtz, F., Almeev, R., & Portnyagin, M. (2010, October). Solubility of H_2O- and CO_2-bearing fluids in tholeiitic basalts at pressures up to 500MPa. *Chemical Geology*, *277*(1-2), 115–125. Retrieved 2021-09-10, from https://linkinghub.elsevier.com/retrieve/pii/S0009254110002640 doi: 10.1016/j.chemgeo.2010.07.014

Shorttle, O., & Maclennan, J. (2011, November). Compositional trends of Icelandic basalts: Implications for short–length scale lithological heterogeneity in mantle plumes. *Geochemistry, Geophysics, Geosystems*, *12*(11), Q11008. Retrieved 2017-02-01, from http://onlinelibrary.wiley.com/doi/10.1029/2011GC003748/abstract doi: 10.1029/2011GC003748

Tadesse, A. Z., Ayalew, D., Pik, R., Yirgu, G., & Fontijn, K. (2019, January). Magmatic evolution of the Boku Volcanic Complex, Main Ethiopian Rift. *Journal of African Earth Sciences*, *149*, 109–130. Retrieved 2019-01-26, from http://www.sciencedirect.com/science/article/pii/S1464343X18302450 doi: 10.1016/j.jafrearsci.2018.08.003

Tetreault, J. L., & Buiter, S. J. H. (2018, October). The influence of extension rate and crustal rheology on the evolution of passive margins from rifting to break-up. *Tectonophysics*, *746*, 155–172. Retrieved 2022-12-01, from https://www.sciencedirect.com/science/article/pii/S0040195117303505 doi: 10.1016/j.tecto.2017.08.029

Thybo, H., & Nielsen, C. A. (2009, February). Magma-compensated crustal thinning in continental rift zones. *Nature*, *457*(7231), 873–876. Retrieved 2018-05-23, from https://www.nature.com/articles/nature07688 doi: 10.1038/nature07688

Tucker, J. M., Hauri, E. H., Pietruszka, A. J., Garcia, M. O., Marske, J. P., & Trusdell, F. A. (2019, June). A high carbon content of the Hawaiian mantle from olivine-hosted melt inclusions. *Geochimica et Cosmochimica Acta*, *254*, 156–172. Retrieved 2019-05-15, from http://www.sciencedirect.com/science/article/pii/S001670371930208X doi: 10.1016/j.gca.2019.04.001

Wallace, P. J., Plank, T., Bodnar, R. J., Gaetani, G. A., & Shea, T. (2021). Olivine-Hosted Melt Inclusions: A Microscopic Perspective on a Complex Magmatic World. *Annual Review of Earth and Planetary Sciences*, *49*(1), null. Retrieved 2021-03-03, from https://doi.org/10.1146/annurev-earth-082420-060506 (_eprint: https://doi.org/10.1146/annurev-earth-082420-060506) doi: 10.1146/annurev-earth-082420-060506

Weinstein, A., Oliva, S. J., Ebinger, C. J., Roecker, S., Tiberi, C., Aman, M., … Fischer, T. P. (2017). Fault-magma interactions during early continental rifting: Seismicity of the Magadi-Natron-Manyara basins, Africa. *Geochemistry, Geophysics, Geosystems*, *18*(10), 3662–3686. Retrieved 2022-11-24, from https://onlinelibrary.wiley.com/doi/abs/10.1002/2017GC007027 (_eprint: https://onlinelibrary.wiley.com/doi/pdf/10.1002/2017GC007027) doi: 10.1002/2017GC007027

Whaler, K. A., & Hautot, S. (2006, January). The electrical resistivity structure of the crust beneath the northern Main Ethiopian Rift. In G. Yirgu, C. J. Ebinger, & P. K. H. Maguire (Eds.), *The Afar Volcanic Province within the East African Rift System* (Vol. 259, pp. 293–305). Retrieved 2018-11-12, from `http://sp.lyellcollection.org/content/259/1/293`

White, R. S., Smith, L. K., Roberts, A. W., Christie, P. a. F., Kusznir, N. J., & the rest of the iSIMM Team. (2008, March). Lower-crustal intrusion on the North Atlantic continental margin. *Nature*, *452*(7186), 460–464. Retrieved 2018-05-13, from `https://www.nature.com/articles/nature06687` doi: 10.1038/nature06687

Wieser, P. E., Iacovino, K., Matthews, S., Moore, G., & Allison, C. M. (2022). VESIcal: 2. A Critical Approach to Volatile Solubility Modeling Using an Open-Source Python3 Engine. *Earth and Space Science*, *9*(2), e2021EA001932. Retrieved 2022-07-14, from `https://onlinelibrary.wiley.com/doi/abs/10.1029/2021EA001932` (_eprint: https://onlinelibrary.wiley.com/doi/pdf/10.1029/2021EA001932) doi: 10.1029/2021EA001932

Wieser, P. E., Lamadrid, H., Maclennan, J., Edmonds, M., Matthews, S., Iacovino, K., . . . Ilyinskaya, E. (2021). Reconstructing Magma Storage Depths for the 2018 Kilauean Eruption From Melt Inclusion CO_2 Contents: The Importance of Vapor Bubbles. *Geochemistry, Geophysics, Geosystems*, *22*(2), e2020GC009364. Retrieved 2021-02-13, from `https://agupubs.onlinelibrary.wiley.com/doi/abs/10.1029/2020GC009364` (_eprint: https://agupubs.onlinelibrary.wiley.com/doi/pdf/10.1029/2020GC009364) doi: https://doi.org/10.1029/2020GC009364

Wong, K., Ferguson, D., Matthews, S., Morgan, D., Tadesse, A. Z., Sinetebeb, Y., & Yirgu, G. (2022, November). Exploring rift geodynamics in Ethiopia through olivine-spinel Al-exchange thermometry and rare-earth element distributions. *Earth and Planetary Science Letters*, *597*, 117820. Retrieved 2022-09-23, from `https://www.sciencedirect.com/science/article/pii/S0012821X22004563` doi: 10.1016/j.epsl.2022.117820

References from the Supporting Information

(Schneider et al., 2012; Tucker et al., 2019; Wieser et al., 2021; Lamadrid et al., 2017; Hartley et al., 2014; Iacovino & Till, 2019; Moore et al., 2018, 2015; DeVitre et al., 2021; Hauri et al., 2002; Shishkina et al., 2010; Jochum et al., 2006; Jarosewich, 2002; J. J. Donovan, 2021; Danyushevsky & Plechov, 2011; Danyushevsky, 2001; Gleeson et al., 2017; DeVitre et al., 2022; Iacovino et al., 2021; Wieser et al., 2022; Ghiorso & Gualda, 2015; Iddon et al., 2019; Wong et al., 2022; Iddon & Edmonds, 2020; Dixon, 1997; Iacono-Marziano et al., 2012; Allison et al., 2019; Newman & Lowenstern, 2002; Gualda et al., 2012; Neave et al., 2012; Blundy & Wood, 1991; Saria et al., 2014; Le Voyer et al., 2018; Kendall et al., 2005; Bastow et al., 2010; Lavayssière et al., 2018; Daniels et al., 2014; Armitage et al., 2015; Hunt et al., 2017; Keir et al., 2006; Daly et al., 2008)

CReDiT: Author Contributions

- Conceptualization: KW, DF, DM, ME, GY
- Formal analysis: KW, DF, PW, ME
- Funding acquisition: KW, DF, DM, ME, GY
- Investigation: KW, DF, PW, JH, SH
- Resources: KW, DF, AZT, GY
- Supervision: DF, DM, ME, GY
- Visualization: KW, PW
- Writing – original draft: KW, DF
- Writing – review and editing: All authors

Figure 1.

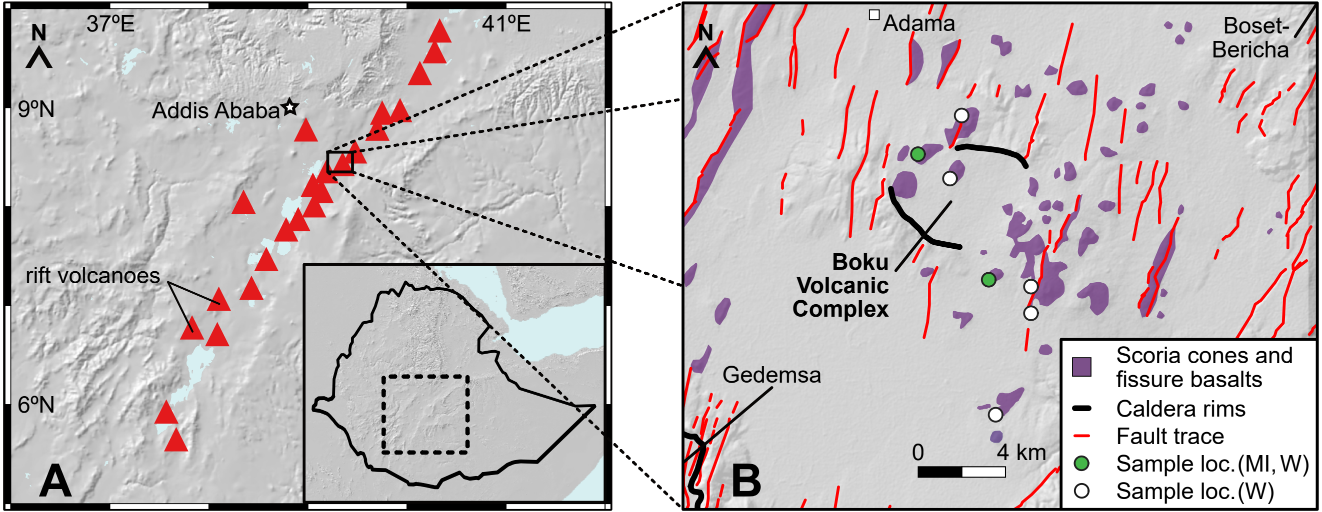

37ºE
41ºE
N
9ºN
Addis Ababa
rift volcanoes
6ºN
A
N
Adama
Boset-
Bericha
Boku
Volcanic
Complex
Gedemsa
0
4 km
B
Scoria cones and
fissure basalts
Caldera rims
Fault trace
Sample loc. (MI, W)
Sample loc. (W)

Figure 2.

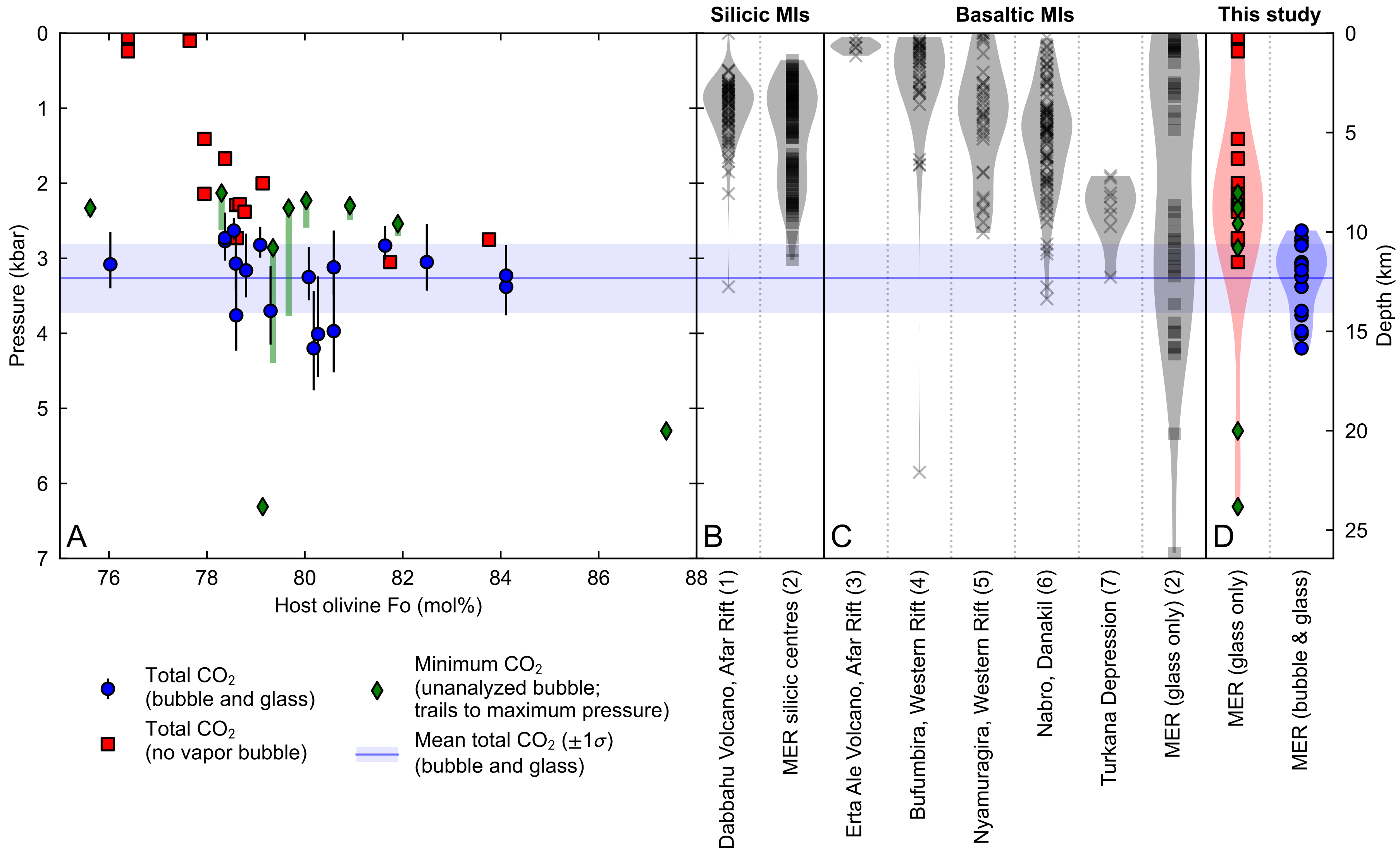
Silicic MIs
Basaltic MIs
This study
Pressure (kbar)
Depth (km)
Host olivine Fo (mol%)
A
B
C
D
Dabbahu Volcano, Afar Rift (1)
MER silicic centres (2)
Erta Ale Volcano, Afar Rift (3)
Bufumbira, Western Rift (4)
Nyamuragira, Western Rift (5)
Nabro, Danakil (6)
Turkana Depression (7)
MER (glass only) (2)
MER (glass only)
MER (bubble & glass)
Total CO_2 (bubble and glass)
Total CO_2 (no vapor bubble)
Minimum CO_2 (unanalyzed bubble; trails to maximum pressure)
Mean total CO_2 ($\pm 1\sigma$) (bubble and glass)

Figure 3.

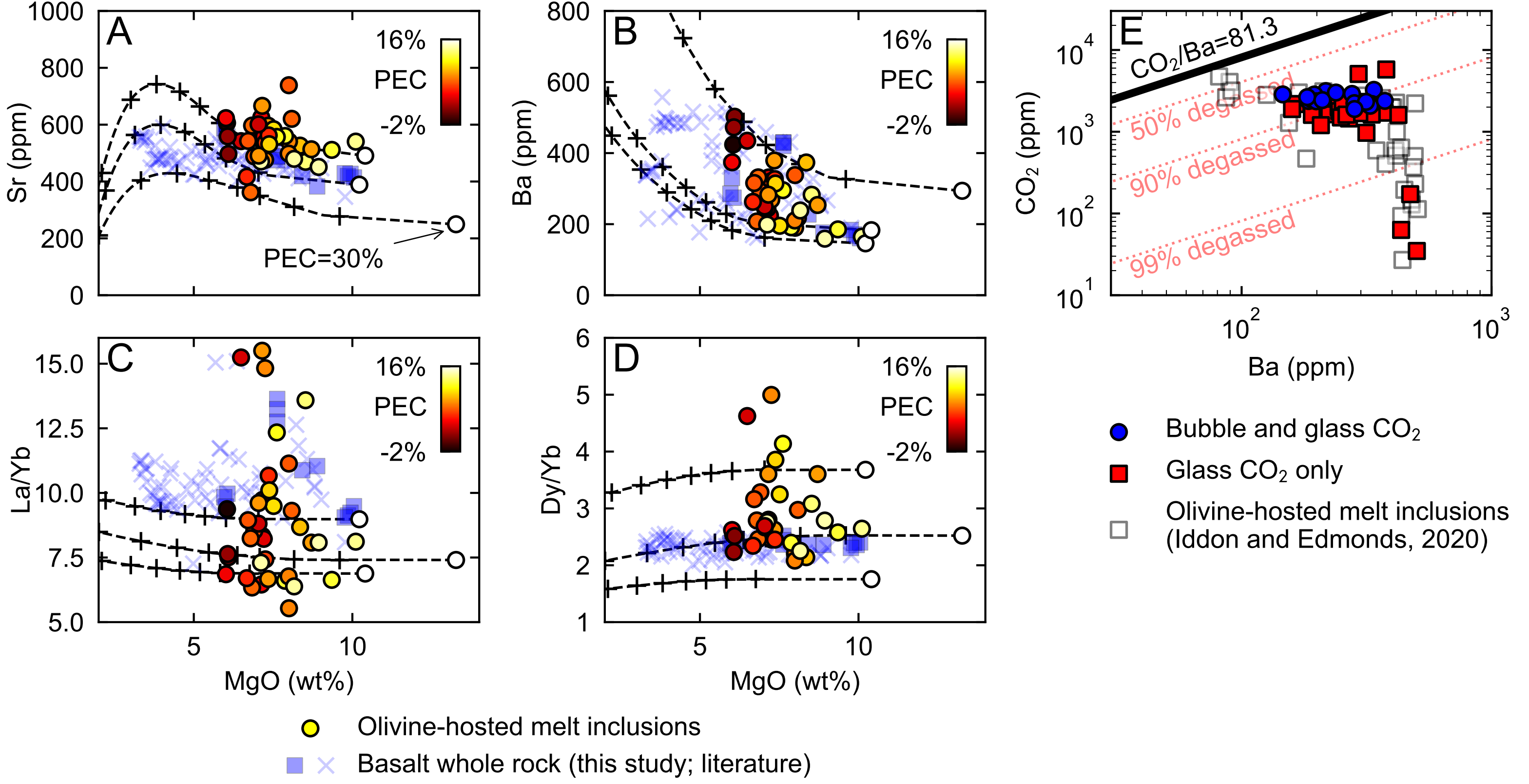

A
B
C
D
E
16%
PEC
-2%
PEC=30%
Sr (ppm)
Ba (ppm)
La/Yb
Dy/Yb
MgO (wt%)
CO2/Ba=81.3
50% degassed
90% degassed
99% degassed
CO2 (ppm)
Bubble and glass CO2
Glass CO2 only
Olivine-hosted melt inclusions (Iddon and Edmonds, 2020)
Olivine-hosted melt inclusions
Basalt whole rock (this study; literature)

Figure 4.

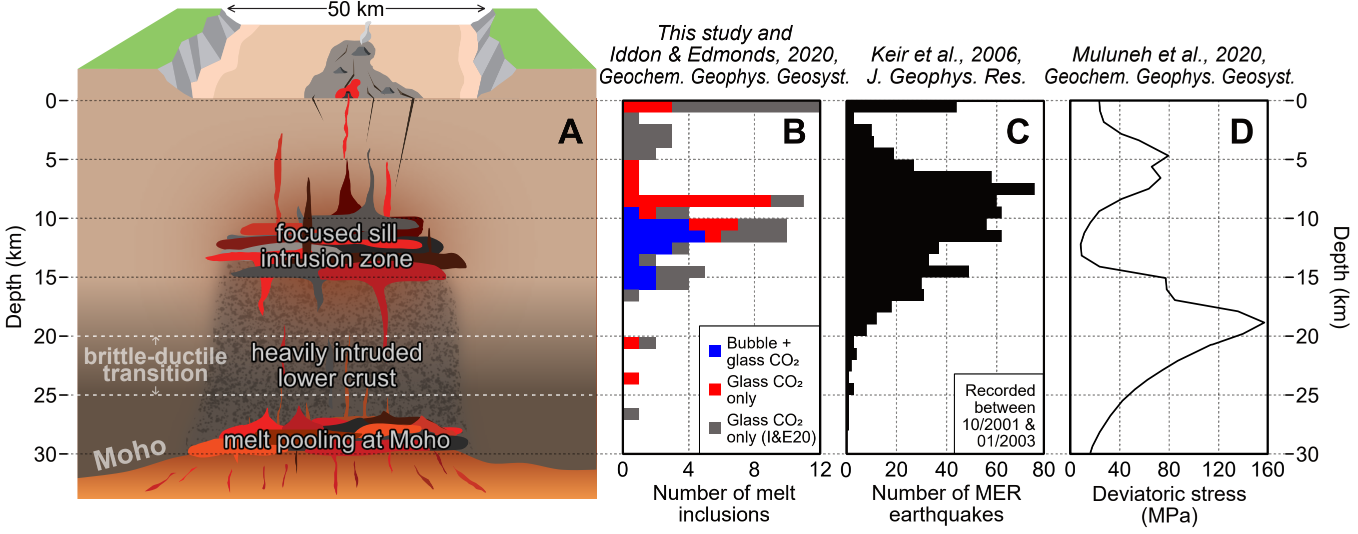

50 km
A
focused sill intrusion zone
heavily intruded lower crust
brittle-ductile transition
melt pooling at Moho
Moho
Depth (km)
0
5
10
15
20
25
30
This study and Iddon & Edmonds, 2020, Geochem. Geophys. Geosyst.
B
Bubble + glass CO₂
Glass CO₂ only
Glass CO₂ only (I&E20)
0
4
8
12
Number of melt inclusions
Keir et al., 2006, J. Geophys. Res.
C
Recorded between 10/2001 & 01/2003
0
20
40
60
80
Number of MER earthquakes
Muluneh et al., 2020, Geochem. Geophys. Geosyst.
D
0
40
80
120
160
Deviatoric stress (MPa)
Depth (km)

Focused mid-crustal magma intrusion during continental break-up in Ethiopia

Kevin Wong[1*], David Ferguson[1], Penny Wieser[2], Daniel Morgan[1], Marie Edmonds[3], Amdemichael Zafu Tadesse[4], Gezahegn Yirgu[5], Jason Harvey[1], and Samantha Hammond[6]

[1]School of Earth and Environment, University of Leeds, Leeds LS2 9JT, United Kingdom
[2]Earth and Planetary Science, University of California, Berkeley, CA 94720-4767, United States of America
[3]Centre for the Observation and Modelling of Earthquakes, Volcanoes and Tectonics (COMET), Department of Earth Sciences, University of Cambridge, Cambridge CB2 3EQ, United Kingdom
[4]Department of Geosciences, Environment and Society, Université Libre de Bruxelles (ULB), 50 B-1050 Bruxelles, Belgium
[5]School of Earth Sciences, Addis Ababa University, P. O. Box 1176 Addis Ababa, Ethiopia
[6]School of Environment, Earth and Ecosystems Sciences, The Open University, Milton Keynes MK7 6AA, United Kingdom

Key Points:

- We determine magma storage conditions in the Main Ethiopian Rift through geochemical analysis of olivine-hosted melt inclusions.
- Volatile saturation barometry reveals that basaltic melts are focused at 10–15 km depth in the Ethiopian crust.
- Geochemical heterogeneity in melt inclusions suggests that magma storage is likely to occur in semi-discrete sills.

*Current address, Department of Biological, Geological, and Environmental Sciences (BiGeA), Alma Mater Studiorum Università di Bologna, Piazza di Porta San Donato 1, 40126, Bologna, Italy

Corresponding author: Kevin Wong, `kevin.wong@unibo.it`

Abstract

Significant volumes of magma are intruded into the crust during continental break-up, which can influence rift evolution by altering thermo-mechanical structure of the crust and thereby its response to extensional stresses. Rift magmas additionally feed surface volcanic activity and can be globally significant sources of tectonic CO_2 emissions. Understanding how magmatism may affect rift development requires knowledge on magma intrusion depths in the crust. Here, using data from olivine-hosted melt inclusions, we investigate magma dynamics for basaltic intrusions in the Main Ethiopian Rift (MER). We find evidence for a spatially focused zone of magma intrusion at the MER upper-lower crustal boundary (10-15 km depth), consistent with geophysical datasets. We propose that ascending melts in the MER are intruded over this depth range as discrete sills, likely creating a mechanically weak mid-crustal layer. Our results have important implications for how magma addition can influence crustal rheology in a maturing continental rift.

Plain Language Summary

Continental rifting, the break-up of continents to form new ocean basins, is a key component in the tectonic cycle that affects Earth's surface environment. The rifting process is aided by magmatic activity in its final stages, which weakens the crust by heating it. This is believed to facilitate present-day rifting in Ethiopia, where we can find rift-related volcanoes. Where melts are stored in the rifting crust will determine how heat is distributed, and therefore how the physical properties of the crust will be altered. Here we analyse melt inclusions, small pockets of precursor magmas trapped in crystals. Because melt inclusions are trapped at depth they record key geochemical information about the conditions magmas experience as they enter the crust from the mantle. By considering the concentrations of CO_2 and H_2O in our melt inclusions we demonstrate that magmas are focused in a 10–15 km zone in the rifting Ethiopian crust. The diverse geochemistry of our melt inclusions additionally suggests that magmas do not substantially mix together in the crust, and are likely to be stored within non-interacting magmatic bodies. This study therefore provides new insights into how melts are stored in the Ethiopian crust before volcanic eruptions.

1 Introduction

Continental rifting involves the rupture of strong continental lithosphere to form new ocean basins. Evidence from active continental rifts and passive margins suggests that continental break-up often involves intrusion of substantial volumes of magma into the rifting crust (e.g., White et al., 2008; Bastow et al., 2011; Bastow & Keir, 2011). These magmas can accommodate extension via dyke intrusion and, depending on their distribution in space and time, may alter the thermo-mechanical structure of the crust (e.g., Buck, 2006; Daniels et al., 2014; Lavecchia et al., 2016; Muluneh et al., 2020). Determining where and how intruded melts accumulate during rift development is therefore crucial for understanding how the rheology and density structure of the crust evolves with progressive rifting, which in turn has a strong influence on how the crust responds to far-field extensional stresses during non-magmatic and magmatic rifting regimes (e.g., Bialas et al., 2010; Tetreault & Buiter, 2018; Oliveira et al., 2022).

Although the syn-rift interplay between magmatism and tectonics is a key ingredient in facilitating continental break-up (e.g., Thybo & Nielsen, 2009; Bastow & Keir, 2011), observational constraints on the depths of basaltic intrusion in active rifts obtained through petrology and geochemistry remain limited. While geophysical observations can infer depths of intrusion and storage of crustal melts (e.g., seismicity concurrently triggered during emplacement; Keir et al., 2006; Ebinger et al., 2008), only petrological observations, obtained from basaltic materials derived directly from the intruding melts

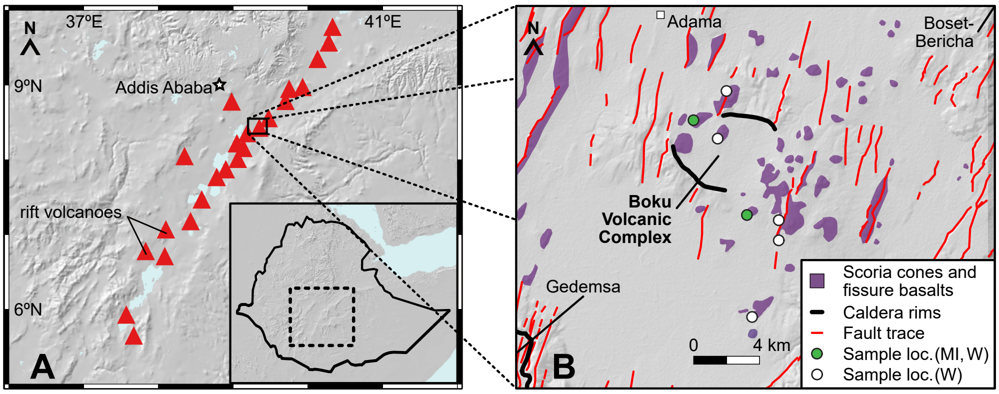

Figure 1. A. The location of the Boku Volcanic Complex in the MER. B. Simplified geological map of Boku, with olivine-hosted melt inclusion (MI) and whole-rock (W) sample localities shown. Digital elevation models are GTOPO30 (A) and SRTM (B). Volcano locations in subfigure A are obtained from the Global Volcanism Program, Smithsonian Institution (`https://volcano.si.edu/`).

themselves, can provide first-hand evidence of the magmatic conditions associated with crustal emplacement.

The Main Ethiopian Rift (MER), comprising the northernmost sector of the East African Rift system (EARS), provides a natural laboratory to examine the interplay between rift geodynamics and magmatic intrusion. This late-stage continental rift, which bridges the large fault-bound grabens of the Kenyan Rift and inferred incipient seafloor spreading in Afar (Figure 1A), has been extensively studied through multiple geophysical approaches (e.g., Bastow et al., 2011). These studies suggest that significant magma intrusion has occurred in the MER lithosphere, focused under ∼20 km-wide and ∼60 km-long magmatic-tectonic segments (e.g., Bastow et al., 2011), where as much as half of the crustal volume may comprise new igneous material (Maguire et al., 2006; Daniels et al., 2014). The compositional and thermal effects of magma intrusion may modify the response of the Ethiopian crust to extension, determining where and how strain is localized as rifting proceeds (e.g., Bastow & Keir, 2011; Lavecchia et al., 2016). Furthermore, degassing of intruded melts during and after emplacement contributes to the significant diffuse CO_2 fluxes measured in the MER (Hunt et al., 2017).

In this study we use petrological methods to investigate the storage depths and compositional diversity of intruded basaltic magmas in the northern MER. Our constraints on magma intrusion conditions are derived from analysis of olivine-hosted silicate melt inclusions (MIs), which are small pockets of quenched magma trapped within growing crystals during crustal magma storage (e.g., Wallace et al., 2021). Unlike erupted lavas, MIs can preserve magmatic volatile contents (e.g., CO_2, H_2O etc., Wallace et al., 2021), allowing volatile saturation pressures, and therefore magmatic storage depths, to be determined (e.g., Ghiorso & Gualda, 2015). Of particular importance is the volatile species CO_2, which degases strongly with decreasing pressure in basaltic magmas (e.g., Dixon et al., 1995). Continental rifts, including the MER, are known to be significant sources of passively degassing magmatic CO_2 (Lee et al., 2016; Foley & Fischer, 2017; Hunt et al., 2017). By considering the total CO_2 in MIs, entrapped within both glass and bubble, we provide new well-constrained petrological estimates of basaltic intrusion pressures in the MER.

2 Materials and Methods

Our samples are scoriae from the Boku Volcanic Complex, a Quaternary monogenetic basaltic cone field located in the northern MER (Figure 1B Tadesse et al., 2019). Littering the remnants of a collapsed ∼500 ka caldera, the later-stage ∼200 ka basaltic cones and fissure flows of Boku are associated with adjacent faults which are sub-parallel to the strike of the MER (Figure 1; Rooney et al., 2011; Tadesse et al., 2019). Quarries provide access into the interiors of cones, where fresh glassy basaltic scoria can be sampled.

Olivine crystals from two Boku cones (Figure 1), picked from disaggregated scoria, were characterized for MIs, individually polished to 0.25 μm grade on glass slides to expose MIs, and mounted in epoxy resin. We have measured the compositions of 40 MIs (full methods in Supporting Information). 27 of these MIs contain CO_2-rich vapor bubbles, which form from post-entrapment changes in pressure, volume and temperature (e.g., Moore et al., 2015; Maclennan, 2017). Bubbles can host a significant fraction of the MI CO_2 budget (e.g., Hartley et al., 2014; Wieser et al., 2021). To estimate the total CO_2 in MIs, essential for accurate barometry, 18 MIs were additionally assessed for shrinkage bubble CO_2 density using Raman spectroscopy. Our approach differs from previous studies considering MIs from the EARS in this regard, which have opted to either a) experimentally rehomogenize the bubble (Head et al., 2011; Hudgins et al., 2015), b) use CO_2 equation of state methods (Rooney et al., 2022), or c) select MIs without vapor bubbles wherever possible (Field, Barnie, et al., 2012; Field, Blundy, et al., 2012; A. Donovan et al., 2017; Iddon & Edmonds, 2020). The primary advantage of our approach is the direct measurement of bubble CO_2 without making assumptions concerning bubble cooling history and post-entrapment processes or experimentally modifying the MI glass composition, which will introduce uncertainties that are difficult to assess and quantify (Rasmussen et al., 2020; Wieser et al., 2021). In addition, by selecting bubble-hosting MIs we avoid biases towards magmatic conditions that favor bubble-free MIs, which may not be representative of crustal melt storage. By doing so, we provide a robust estimate of total CO_2 in an MI, which can be used to determine crustal melt storage pressures.

After Raman spectroscopy, all MIs were analysed for trace and volatile elements in the glass phase by SIMS. This was followed by EPMA to assess major element compositions of MI glass, carrier melt, and host olivine crystals. MI compositions were corrected for post-entrapment crystallization (PEC) using Petrolog3 software (Danyushevsky & Plechov, 2011, full details in Supporting Information). The total CO_2 of MIs is calculated by mass balance using the CO_2 measured in the bubble and MI glass (e.g., Hartley et al., 2014). To complement the MI compositional dataset, we have additionally assessed the major and trace element whole-rock compositions of basalts collected from several Boku scoria cones and fissure flows using XRF and solution ICP-MS respectively. All standards and geochemical data are presented in Supporting Dataset S1.

3 Results

3.1 Magma Intrusion Depths in the Main Ethiopian Rift

Our key barometric and geochemical results are presented in Figures 2 and 3, with additional figures presented in the Supporting Information. MIs are entrapped within olivine crystals of composition Fo_{76-88}, and there are no systematic differences in major, trace, or volatile element concentrations between MIs collected from the two cones in this study (Dataset S1). CO_2 concentrations range from 35–5770 ppm in MI glass only; MIs with CO_2 measurements in both the glass and vapor bubble have total combined CO_2 contents of 1895–3248 ppm, with 15–46% of the CO_2 residing within the bubble (Dataset S1). Where an unanalyzed shrinkage bubble is present, CO_2 contents are assumed to be minima and we estimate the plausible range of total CO_2 using our bub-

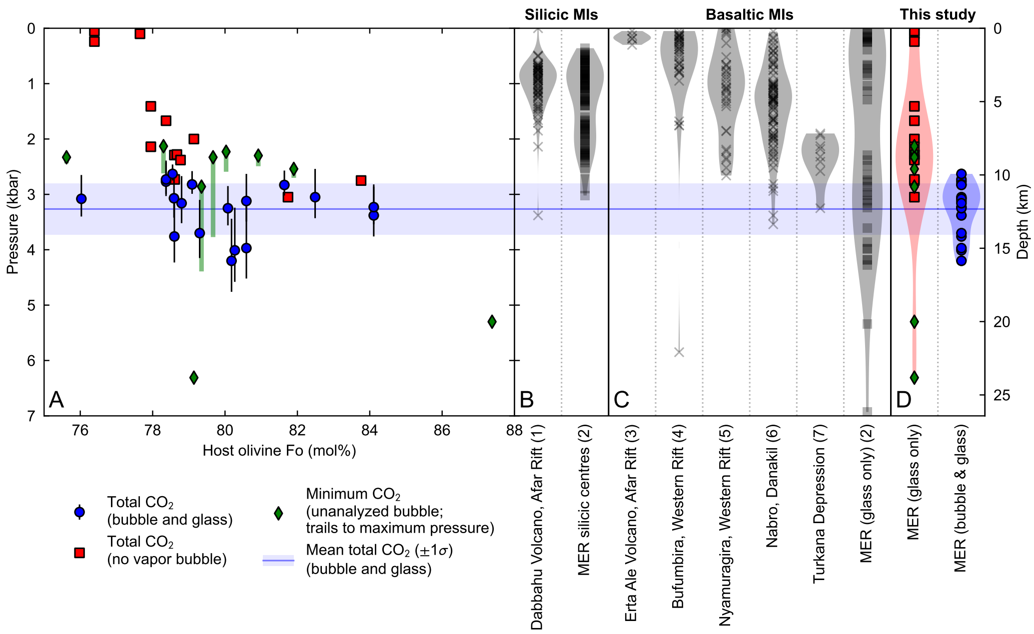

Figure 2. A. Volatile CO_2-H_2O saturation pressures of olivine-hosted MIs from the MER, plotted against MI olivine host Fo (olivine Fo=100·Mg/(Fe+Mg)). MIs are categorized on which components are analyzed. Physical dimensions of MI vapor bubbles that are analyzed only for glass composition can be used to estimate maximum CO_2 if bubble CO_2 density is well characterized (green diamonds); this is performed assuming a density of 0.21 g cm^{-3} (see Supporting Information). Error bars on pressures calculated from MIs for which bubble and glass are analysed are 1σ. B–D. Violin plots of volatile CO_2-H_2O saturation pressures recorded by mineral-hosted MIs from the EARS and Afar calculated using MagmaSat. Saturation pressures are individually determined for each MI using their recorded major and trace element composition and magmatic temperatures. Where FeO_t is provided without Fe_2O_3 all Fe is assumed to be Fe^{2+}. Subfigure B shows distributions of silicic MIs (SiO_2 >60 wt%), subfigure C shows basaltic MIs (SiO_2 <55 wt%), and subfigure D shows the basaltic MIs of this study. The blue line and shaded area across all subfigures marks the mean and 1σ of the MI subset of this study with combined vapor bubble and glass CO_2. References: 1. Field, Blundy, et al. (2012); 2. Iddon and Edmonds (2020), shown as squares for emphasis; 3. Field, Barnie, et al. (2012); 4. Hudgins et al. (2015); 5. Head et al. (2011); 6. A. Donovan et al. (2017); 7. Rooney et al. (2022), without bubble corrections.

ble CO_2 density measurements (see Supporting Information). H_2O concentrations display less variability: discounting the three MIs that have clearly degassed (containing $\leq$0.4 wt% H_2O), MIs have a mean H_2O concentration of 1.1$\pm$0.2 wt% (Supporting Figure S6), which is comparable to H_2O concentrations obtained from other MER and EARS MIs (Iddon & Edmonds, 2020; Rooney et al., 2022).

Volatile saturation pressures of MIs are calculated using the fully thermodynamic MagmaSat volatile solubility model (Ghiorso & Gualda, 2015) via the Python 3 library VESIcal (Iacovino et al., 2021; Wieser et al., 2022); other volatile solubility models are considered and compared in the Supporting Information. Storage pressures for MIs for which total CO_2 contents are known (vapor bubble and glass), determined at a magmatic temperature of 1200 °C (Iddon et al., 2019; Wong et al., 2022), vary over a relatively narrow range from 2.5–4.5 kbar (Figure 2A). In the MER these pressures correspond to depths of $\sim$10–15 km (assuming a crustal density of 2.7 g cm^{-3}), among the deepest recorded volatile saturation depths for continental rift magmas (Figure 2B-D). Pressures recorded by MIs without bubbles overlap partially with those that do have analyzed bubbles; however, the average CO_2 concentration and therefore pressure of MIs without a bubble is typically lower than those with a bubble. Two MIs for which only inclusion glass CO_2 is known record higher pressures in excess of 5 kbar ($\sim$20 km), corresponding to the MER lower crust. Overall, our barometric results show a relatively limited distribution of magma storage depths with a narrowly focused zone of intrusion centered at $\sim$12 km depth, coincident with the seismically imaged boundary between the upper and lower crust in the MER (Maguire et al., 2006), and in close agreement with MI volatile saturation pressures from the Turkana Depression to the south of the MER (Figure 2C; Rooney et al., 2022).

3.2 Melt Inclusion Trace Element Compositions

The major element compositions of MIs overlap with carrier basalt (Supporting Figure S8) and whole-rock compositions of erupted lavas (Dataset S1; Tadesse et al., 2019; Nicotra et al., 2021). Incompatible trace element concentrations vary considerably in both MIs and lavas, but nonetheless still overlap (Figures 3A and B). Greater primary compositional variability is preserved in the MIs over the whole rocks, further evidenced by variations in trace element ratios that are not significantly affected by crystal fractionation, e.g., La/Yb and Dy/Yb (Figures 3C and D). While absolute trace element compositions can be achieved by melt fractionation from our most primitive MIs (Figures 3A and B), the scatter in trace element ratios cannot be replicated solely by fractionation of a common parental melt (Figures 3C and D).

By comparing CO_2 concentrations with trace elements with similar behavior during mantle melting (e.g., Ba, Rb), CO_2 degassing from mantle melts can be assessed (e.g., Le Voyer et al., 2018). While primary magmatic CO_2 contents are not known for MER magmas, the highest observed CO_2/Ba and CO_2/Rb ratios approach those measured in undegassed MORB (Le Voyer et al., 2018). Assuming that initial CO_2-trace element ratios are similar to those of MORB, CO_2/Ba and CO_2/Rb systematics for MER MIs clearly show evidence for degassing of CO_2 even in MIs with total CO_2 determinations (Figure 3E). Most melts therefore appear to have lost substantial volumes of CO_2 prior to MI entrapment (Figure 3E). If MORB ratios are reflective of primary CO_2/Ba and CO_2/Rb values in MER melts then initial CO_2 contents will be in the range of 1–4 wt% (mean of 2.0$\pm$0.6 wt% with the same CO_2/Ba as MORB), with $\sim$60–95% of the CO_2 having been exsolved at mid-crustal pressures.

CO_2 degassing in the MER, likely derived from degassing of intruded mid-crustal magmas, is focused along discrete fault zones (Hunt et al., 2017). By making assumptions on the volumes of melt intruded into the crust (e.g., Iddon & Edmonds, 2020), we determine that the difference between expected CO_2 concentrations in primary mantle

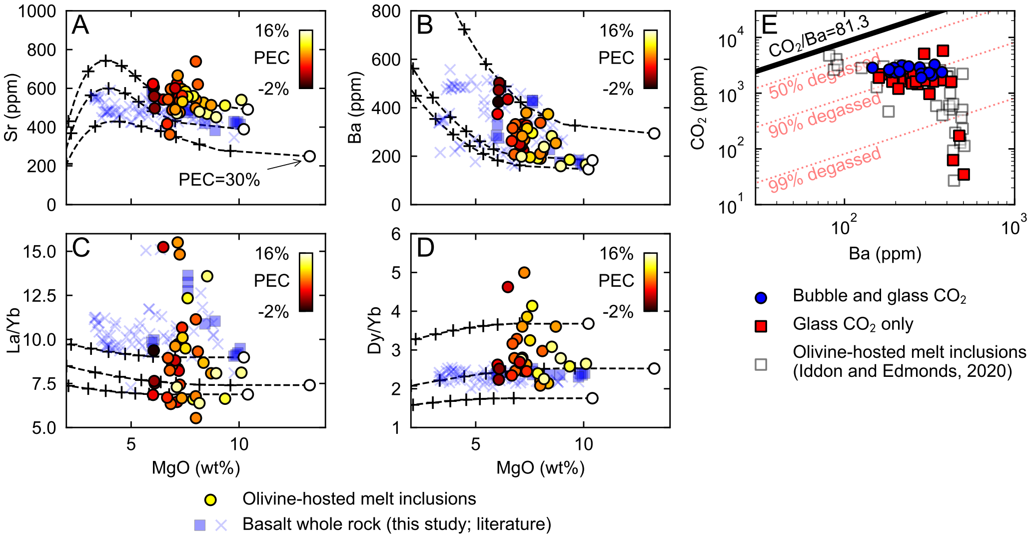

Figure 3. A–D. MI and whole-rock trace element and trace element ratios plotted against MgO (this study; Tadesse et al., 2019; Nicotra et al., 2021). Liquid lines of descent with crosses denoting 10% fractionation intervals are determined from our three highest MgO melts using Rhyolite-MELTS v1.2.0 (Gualda et al., 2012, see Supporting Information), assuming Rayleigh fractionation with the partition coefficients collated by Iddon and Edmonds (2020). PEC corrections are detailed in the Supporting Information. E. Olivine-hosted MI CO_2 plotted against Ba; primary CO_2/Ba of MORB (Le Voyer et al., 2018).

melts and those observed in our MIs is sufficient to generate the CO_2 fluxes measured from surface degassing (Figure 3E Hunt et al., 2017, see Supporting Information). The restriction of significant degassing to localized regions in the MER (Hunt et al., 2017) may suggest that some regions are subject to active intrusion at the present day whereas other portions are not; future studies should aim to constrain this periodicity of melt emplacement.

4 Discussion

4.1 Depths of Intrusion in the East African Rift

Our total CO_2 saturation pressures determined from vapor bubble and glass are in broad agreement with maximum pressures of melt storage estimated from MI volatiles at other EARS sectors (Figure 2B–D). Applying the same volatile solubility modelling performed on our MIs to literature datasets, we determine that our proposed 10–15 km depth range for basalt storage coincides with the deepest MIs at other parts of the EARS and Afar Rift (Figure 2C; e.g., A. Donovan et al., 2017; Rooney et al., 2022). Geophysical observations of crustal melt movement in other sectors of the EARS (Weinstein et al., 2017; Reiss et al., 2021, 2022) suggests that melt focusing at these pressures may be ubiquitous within the EARS.

The lack of evidence for significant melt storage within the upper crust in our dataset contrasts with the depth distributions for magma storage obtained from suites of MIs collected at large caldera-forming volcanic centers found along the MER (Figure 2; Iddon & Edmonds, 2020). Under these silicic centers, melt storage appears to extend upwards into the upper crust, where evolved magmas are generated via low pressure fractionation (Iddon & Edmonds, 2020). Notably, the maximum storage depths under caldera complexes in the EARS identified both from MI volatile saturation barometry (Figure 2; Iddon & Edmonds, 2020; Rooney et al., 2022) and from mineral barometry (Rooney et al., 2005; Iddon et al., 2019) coincides with the 10–15 km depth range observed in our dataset. This depth range may therefore be the locus of initial basaltic melt emplacement along the MER, with important implications for heat distribution within the rifting crust and therefore crustal strength profiles (Buck, 2006; Daniels et al., 2014; Lavecchia et al., 2016), such as the creation of a mid-crustal weak layer (Muluneh et al., 2020). With the exception of those below caldera complexes/silicic volcanoes (e.g., Biggs et al., 2011), upper crustal melt bodies (<10 km depth) in the MER are likely to be ephemeral, perhaps forming during periodic intrusive-eruptive episodes (e.g., Ebinger et al., 2013).

In contrast to the extensive MI data corresponding to mid-crustal pressures, very few MIs from our dataset and the MER dataset of Iddon and Edmonds (2020) record pressures corresponding to the lower crust or Moho (Figure 2; e.g., Maguire et al., 2006; Lavayssière et al., 2018). Considering the evolved compositions of our olivines (mean Fo_{80}) relative to Fo_{90} olivines in other MER volcanic materials (e.g., Rooney et al., 2005), we posit that an initial stage of fractionation near the Moho prior to ascent to mid-crustal pressures is necessary. This hypothesis is supported by low wavespeeds observed at Moho depths from the presence of melt in the heavily intruded lower crust (Keranen et al., 2009; Chambers et al., 2019, 2021), and numerical models suggesting that the lowermost crust is weak, hot and underlies a lower-crustal brittle-ductile transition at 20–25 km (Lavecchia et al., 2016; Muluneh et al., 2020). The absence of strong radial seismic anisotropy in the lower crust may also imply that melt storage at these depths may comprise both sills and isotropic bodies (Chambers et al., 2021). Melts pooling and fractionating at the base of the crust may bypass the ductile lowermost crust entirely if both density differences between melt and crust and lower crustal strain rates are sufficiently high (Muluneh et al., 2021).

4.2 Compositional Heterogeneity in Melt Inclusions

Variability in absolute trace element concentrations (Figures 3A and B) could result from fractional crystallization of distinct parental melts and/or mixing between variably fractionated melts with distinct origins. In contrast, the broader distribution of trace element ratios observed in MIs relative to whole rocks (Figures 3C and D) can only be inherited from the compositional heterogeneity of parental mantle-derived melts. Such variability may be derived from the melting of multiple source lithologies (e.g., Shorttle & Maclennan, 2011) and/or unmixed fractional mantle melts (e.g., Gurenko & Chaussidon, 1995).

Physical interactions between intrusive bodies therefore appear to be limited, and we infer that intruded magmas reside in a series of discrete sills emplaced at a common depth. The slightly lower degree of compositional diversity observed in erupted lavas (Figures 3C and D), even at higher MgO, suggests that some mixing does occur prior to eruption and that dyke intrusion into the upper crust may involve partially homogenized melts sourced from multiple mid-crustal sills. Erupted melts extend to lower MgO than the MIs (after PEC corrections), and pre-eruptive mixing and homogenization may therefore occur during a final stage of differentiation within upper crustal magma bodies.

4.3 Basaltic Melt Focusing in the Main Ethiopian Rift

The presence of melts intruded as mid-crustal sill complexes is strongly supported by geophysical observations of the present-day MER crust. Strong horizontally oriented seismic anisotropy observed in the MER at depths of 10–15 km is consistent with the presence of sills (Chambers et al., 2021). Low seismic moment earthquakes in northern MER magmatic segments are distributed within a narrow depth band between 8–16 km and have been interpreted as being triggered by movement or emplacement of mid-crustal melts (Keir et al., 2006; Daly et al., 2008). High Vp, high-Vp/Vs and high-density bodies are inferred to be present at these depths under Boku and other MER segments (Keranen et al., 2004; Cornwell et al., 2006; Daly et al., 2008), as are high-conductivity crustal anomalies (Whaler & Hautot, 2006), all indicative of partially molten intrusions in the mid-crust. Our results are also in good agreement with empirical observations relating MER cone clustering to melt intrusion depths (Mazzarini et al., 2013). In other words, the melt storage depths resolved directly using petrological methods are in very close agreement with the deepest intrusion pressures determined using geophysical techniques.

Focusing of ascending basaltic melts at this depth range can, to a first order, be attributed to MER crustal density structure as the mean density of the lower crust exceeds that of our MIs (mean of 2.71 g cm^{-3}, calculated after PEC corrections using DensityX, Iacovino and Till (2019); cf. e.g., Cornwell et al. (2006)). Driven by density differences, basaltic melts will rise to mid-crustal depths before they achieve neutral buoyancy, stall and crystallize. The upper crust, comparatively less dense than the lower crust, will limit the ascent of basalt melts beyond the focusing zone (Cornwell et al., 2006; Mickus et al., 2007).

Melt focusing in the mid-crust could also be attributed to the rheological structure of the crust. Numerical models based on seismic observations suggest that the 10–15 km depth range resolved using our MIs coincides with the weakest part of the Ethiopian crust, which is sandwiched between two strong brittle layers in the upper and mid-lower crust (Muluneh et al., 2020). The strong, lower-density brittle crust above this ductile zone, combined with the density limitations discussed above, likely inhibits further ascent of the buoyant melt (Cornwell et al., 2006; Muluneh et al., 2020). Melt may only progress directly to the surface through the breaking of dyke-induced faults (e.g., Casey et al., 2006), by exploiting pre-existing crustal weaknesses (e.g., Le Corvec et al., 2013), or after extensive fractionation to form lower-density silicic melts (e.g., Gleeson et al., 2017).

We therefore hypothesise that the intrusion and emplacement of melts into this weak, ductile mid-crust will have a strong effect on the overall rheology of the rifting crust, which in turn may govern how the crust locally accommodates strain in response to far-field extensional stresses. Ductile stretching may accommodate crustal deformation at a different rate or manner relative to the brittle layers above and below this weak zone, in turn possibly dictating that future batches of melt are focused in the same region. Indeed, the development of crustal sill systems in the MER may arise from pulsed emplacement of magmas from the lower crust or mantle (e.g., Annen et al., 2015). Stacked sills formed in this manner may maintain high localized temperatures in the crust, which can facilitate further intrusion of melt at shallower pressures, or may themselves contract during cooling to generate accommodation space for further intrusions (Magee et al., 2016). Future numerical or analog models of rift deformation in Ethiopia must account for the development of a hot, ductile, weak layer in the crust, and the influences such a layer may have on overall crustal rheology.

5 Summary

The results of our study are summarized in Figure 4. Through the careful analysis of major, trace, and volatile elements in olivine-hosted MIs, we propose that stacked mid-crustal sills in the depth range of 10–15 km are the dominant form of magmatic storage in the MER (Figures 4A and B). These sills are known to be horizontally oriented from seismic anisotropy (Chambers et al., 2019), and develop as a consequence of repeated magmatic intrusion into the mid-crust during the progression of late-stage continental rifting. Initially crystallizing at or near the Moho, mantle-derived magmas bypass the ductile lowermost crust to arrive at the Ethiopian mid-crust, heralded by seismic activity during emplacement (Figure 4C). These melts are stored as discrete sills in the weak,

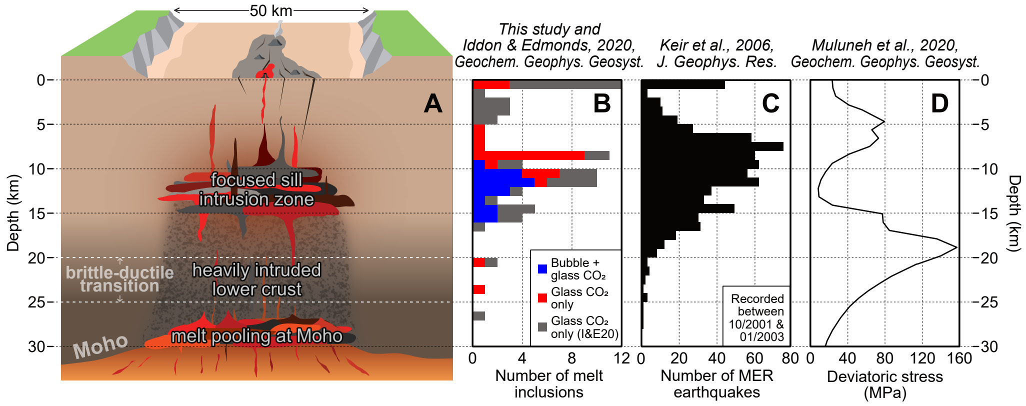

Figure 4. A. Summary cartoon illustrating our proposed structure of the MER crust. Horizontal and vertical dimensions not to same scale. B. Histogram of MER olivine-hosted MI saturation pressures (this study; Iddon & Edmonds, 2020). C. Histogram of MER earthquakes recorded between October 2001 and January 2003 (Keir et al., 2006; Daly et al., 2008, selection criteria in Supporting Figure S9). D. Numerical model of MER crustal deviatoric stress (Muluneh et al., 2020).

ductile mid-crust and blocked from further ascent by a strong, lower density upper crust (Figure 4D). The diverse range of trace element ratios observed in MIs gives evidence to limited melt mixing in the crust; partial mixing of magmas between sills may occur in the shallow crust prior to eruption (Figure 3). Petrological evidence for mid-crustal sills in the MER presented in this study is in agreement with geophysical observations (e.g., Keranen et al., 2004), and the volatile composition of basalts comprising these bodies are consistent with CO_2 degassing rates measured at the rift floor (Hunt et al., 2017). The presence of hot sills in the MER mid-crust has important implications for how intruding melts in late-stage rifts affect and are affected by the rheological structure of the crust, and should be considered a key element in future development of models of continental rifting.

6 Open Research

The complete dataset of geochemical analyses and melt inclusion microscope photographs is available within a Zenodo repository (`doi.org/10.5281/zenodo.7236254`).

Acknowledgments

KW and PW are funded by NERC DTP studentships NE/L002574/1 and NE/L002507/1 respectively. KW acknowledges additional financial support from the Geologists' Association New Researchers Award. Ion probe analyses are funded through NERC grant IMF694/1119 awarded to DF. ME acknowledges the support of COMET via NERC. We thank Cristina Talavera Rodriguez and Lesley Neve for performing geochemical analyses on our behalf during the COVID-19 pandemic. Yared Sinetebeb, Harri Wyn Williams, Emilie Ringe, and Richard Walshaw are thanked for assistance with fieldwork, sample preparation, Raman spectroscopy, and EPMA respectively. We acknowledge thought-provoking discussions with Ian Bastow, Emma Chambers, Tim Craig, Sophie Hautot, Derek Keir, Tyrone Rooney, and Kathy Whaler. Finally, we acknowledge the Ethiopian Ministry of Mines and Oromia State Administration for sampling and field permissions.

References

Allison, C. M., Roggensack, K., & Clarke, A. B. (2019, June). H_2O–CO_2 solubility in alkali-rich mafic magmas: new experiments at mid-crustal pressures. *Contributions to Mineralogy and Petrology*, *174*(7), 58. Retrieved 2022-02-01, from `https://doi.org/10.1007/s00410-019-1592-4` doi: 10.1007/s00410-019-1592-4

Annen, C., Blundy, J. D., Leuthold, J., & Sparks, R. S. J. (2015, August). Construction and evolution of igneous bodies: Towards an integrated perspective of crustal magmatism. *Lithos*, *230*, 206–221. Retrieved 2022-12-09, from `https://www.sciencedirect.com/science/article/pii/S0024493715001759` doi: 10.1016/j.lithos.2015.05.008

Armitage, J. J., Ferguson, D. J., Goes, S., Hammond, J. O. S., Calais, E., Rychert, C. A., & Harmon, N. (2015, May). Upper mantle temperature and the onset of extension and break-up in Afar, Africa. *Earth and Planetary Science Letters*, *418*, 78–90. Retrieved 2018-10-03, from `http://www.sciencedirect.com/science/article/pii/S0012821X15001259` doi: 10.1016/j.epsl.2015.02.039

Bastow, I. D., & Keir, D. (2011, April). The protracted development of the continent–ocean transition in Afar. *Nature Geoscience*, *4*(4), 248–250. Retrieved 2018-05-16, from `https://www.nature.com/articles/ngeo1095` doi: 10.1038/ngeo1095

Bastow, I. D., Keir, D., & Daly, E. (2011, June). The Ethiopia Afar Geoscientific Lithospheric Experiment (EAGLE): Probing the transition from continental rifting to incipient seafloor spreading. In *Geological Society of America Special Papers* (Vol. 478, pp. 51–76). Geological Society of America. Retrieved 2018-10-26, from `https://pubs.geoscienceworld.org/books/book/653/chapter/3806991/` doi: 10.1130/2011.2478(04)

Bastow, I. D., Pilidou, S., Kendall, J.-M., & Stuart, G. W. (2010, June). Melt-induced seismic anisotropy and magma assisted rifting in Ethiopia: Evidence from surface waves. *Geochemistry, Geophysics, Geosystems*, *11*(6). Retrieved 2018-11-02, from `https://agupubs.onlinelibrary.wiley.com/doi/full/10.1029/2010GC003036` doi: 10.1029/2010GC003036

Bialas, R. W., Buck, W. R., & Qin, R. (2010, March). How much magma is required to rift a continent? *Earth and Planetary Science Letters*, *292*(1), 68–78. Retrieved 2022-11-29, from `https://www.sciencedirect.com/science/article/pii/S0012821X10000555` doi: 10.1016/j.epsl.2010.01.021

Biggs, J., Bastow, I. D., Keir, D., & Lewi, E. (2011, September). Pulses of deformation reveal frequently recurring shallow magmatic activity beneath the Main Ethiopian Rift. *Geochemistry, Geophysics, Geosystems*, *12*(9). Retrieved 2019-02-05, from `https://agupubs.onlinelibrary.wiley.com/doi/full/10.1029/2011GC003662` doi: 10.1029/2011GC003662

Blundy, J. D., & Wood, B. J. (1991, January). Crystal-chemical controls on the partitioning of Sr and Ba between plagioclase feldspar, silicate melts, and hydrothermal solutions. *Geochimica et Cosmochimica Acta*, *55*(1), 193–209. Retrieved 2017-05-25, from `http://www.sciencedirect.com/science/article/pii/001670379190411W` doi: 10.1016/0016-7037(91)90411-W

Buck, W. R. (2006, January). The role of magma in the development of the Afro-Arabian Rift System. In G. Yirgu, C. Ebinger, & P. K. H. Maguire (Eds.), *The Afar Volcanic Province within the East African Rift System* (Vol. 259, pp. 43–54). Retrieved 2018-11-05, from `http://sp.lyellcollection.org/content/259/1/43`

Casey, M., Ebinger, C., Keir, D., Gloaguen, R., & Mohamed, F. (2006, January). Strain accommodation in transitional rifts: extension by magma intrusion and faulting in Ethiopian rift magmatic segments. In G. Yirgu, C. J. Ebinger, & P. K. H. Maguire (Eds.), *The Afar Volcanic Province within the East African Rift System* (Vol. 259, pp. 143–163). Retrieved 2018-09-23, from http://sp.lyellcollection.org/content/259/1/143

Chambers, E. L., Harmon, N., Keir, D., & Rychert, C. A. (2019, April). Using Ambient Noise to Image the Northern East African Rift. *Geochemistry, Geophysics, Geosystems*, *20*(4), 2091–2109. Retrieved 2019-06-21, from https://agupubs.onlinelibrary.wiley.com/doi/full/10.1029/2018GC008129 doi: 10.1029/2018GC008129

Chambers, E. L., Harmon, N., Rychert, C. A., & Keir, D. (2021, November). Variations in melt emplacement beneath the northern East African Rift from radial anisotropy. *Earth and Planetary Science Letters*, *573*, 117150. Retrieved 2021-11-03, from https://linkinghub.elsevier.com/retrieve/pii/S0012821X21004052 doi: 10.1016/j.epsl.2021.117150

Cornwell, D. G., Mackenzie, G. D., England, R. W., Maguire, P. K. H., Asfaw, L. M., & Oluma, B. (2006, January). Northern Main Ethiopian Rift crustal structure from new high-precision gravity data. In *The Afar Volcanic Province within the East African Rift System* (Vol. 259, pp. 307–321). Retrieved 2018-11-14, from http://sp.lyellcollection.org/content/259/1/307

Daly, E., Keir, D., Ebinger, C. J., Stuart, G. W., Bastow, I. D., & Ayele, A. (2008, March). Crustal tomographic imaging of a transitional continental rift: The Ethiopian rift. *Geophysical Journal International*, *172*(3), 1033–1048. Retrieved 2018-11-01, from https://academic.oup.com/gji/article/172/3/1033/571185 doi: 10.1111/j.1365-246X.2007.03682.x

Daniels, K. A., Bastow, I. D., Keir, D., Sparks, R. S. J., & Menand, T. (2014, January). Thermal models of dyke intrusion during development of continent–ocean transition. *Earth and Planetary Science Letters*, *385*, 145–153. Retrieved 2018-11-22, from http://www.sciencedirect.com/science/article/pii/S0012821X13005293 doi: 10.1016/j.epsl.2013.09.018

Danyushevsky, L. V. (2001, October). The effect of small amounts of H_2O on crystallisation of mid-ocean ridge and backarc basin magmas. *Journal of Volcanology and Geothermal Research*, *110*(3), 265–280. Retrieved 2021-03-30, from https://www.sciencedirect.com/science/article/pii/S037702730100213X doi: 10.1016/S0377-0273(01)00213-X

Danyushevsky, L. V., & Plechov, P. (2011, July). Petrolog3: Integrated software for modeling crystallization processes. *Geochemistry, Geophysics, Geosystems*, *12*(7), Q07021. Retrieved 2017-12-02, from http://onlinelibrary.wiley.com/doi/10.1029/2011GC003516/abstract doi: 10.1029/2011GC003516

DeVitre, C. L., Barth, A., Gazel, E., Plank, T. A., & Ramalho, R. (2021, December). Solving the Carbonate Problem in Melt Inclusion Bubbles. In *AGU Fall Meeting Abstracts.* Retrieved from https://agu.confex.com/agu/fm21/meetingapp.cgi/Paper/845682

DeVitre, C. L., Dayton, K., Gazel, E., Barth, A., Plank, T. A., Pamukcu, A., ... Monteleone, B. (2022, July). Accounting for Multi-Phase Carbon in Melt Inclusion Bubbles. In *Goldschmidt Conference Abstracts.* Retrieved 2022-08-08, from https://conf.goldschmidt.info/goldschmidt/2022/meetingapp.cgi/Paper/12601

Dixon, J. E. (1997, April). Degassing of alkalic basalts. *American Mineralogist*, *82*(3-4), 368–378. Retrieved 2022-01-05, from https://pubs.geoscienceworld.org/ammin/article/82/3-4/368-378/43291 doi: 10.2138/am-1997-3-415

Dixon, J. E., Stolper, E. M., & Holloway, J. R. (1995, December). An Experimental Study of Water and Carbon Dioxide Solubilities in Mid-Ocean Ridge Basaltic Liquids. Part I: Calibration and Solubility Models. *Journal of Petrology*, *36*(6), 1607–1631. Retrieved 2019-04-08, from https://academic.oup.com/petrology/article/36/6/1607/1493308 doi: 10.1093/oxfordjournals.petrology.a037267

Donovan, A., Blundy, J., Oppenheimer, C., & Buisman, I. (2017, November). The

2011 eruption of Nabro volcano, Eritrea: perspectives on magmatic processes from melt inclusions. *Contributions to Mineralogy and Petrology*, *173*(1), 1. Retrieved 2022-01-17, from `https://doi.org/10.1007/s00410-017-1425-2` doi: 10.1007/s00410-017-1425-2

Donovan, J. J. (2021). *Probe for EPMA v. 13.0.5 User's Guide and Reference (Xtreme Edition).* Retrieved 2022-06-07, from `https://probesoftware.com/download/PROBEWIN.pdf`

Ebinger, C. J., Keir, D., Ayele, A., Calais, E., Wright, T. J., Belachew, M., ... Buck, W. R. (2008, September). Capturing magma intrusion and faulting processes during continental rupture: Seismicity of the Dabbahu (Afar) rift. *Geophysical Journal International*, *174*(3), 1138–1152. Retrieved 2021-02-01, from `https://doi.org/10.1111/j.1365-246X.2008.03877.x` doi: 10.1111/j.1365-246X.2008.03877.x

Ebinger, C. J., van Wijk, J., & Keir, D. (2013, September). The time scales of continental rifting: Implications for global processes. In *Geological Society of America Special Papers* (Vol. 500, pp. 371–396). Geological Society of America. Retrieved 2018-05-18, from `https://pubs.geoscienceworld.org/books/book/671/chapter/3807783/` doi: 10.1130/2013.2500(11)

Field, L., Barnie, T., Blundy, J., Brooker, R. A., Keir, D., Lewi, E., & Saunders, K. (2012, December). Integrated field, satellite and petrological observations of the November 2010 eruption of Erta Ale. *Bulletin of Volcanology*, *74*(10), 2251–2271. Retrieved 2019-08-21, from `https://doi.org/10.1007/s00445-012-0660-7` doi: 10.1007/s00445-012-0660-7

Field, L., Blundy, J., Brooker, R. A., Wright, T., & Yirgu, G. (2012, July). Magma storage conditions beneath Dabbahu Volcano (Ethiopia) constrained by petrology, seismicity and satellite geodesy. *Bulletin of Volcanology*, *74*(5), 981–1004. Retrieved 2019-02-05, from `http://link.springer.com/10.1007/s00445-012-0580-6` doi: 10.1007/s00445-012-0580-6

Foley, S. F., & Fischer, T. P. (2017, December). An essential role for continental rifts and lithosphere in the deep carbon cycle. *Nature Geoscience*, *10*(12), 897–902. Retrieved 2018-07-18, from `https://www.nature.com/articles/s41561-017-0002-7` doi: 10.1038/s41561-017-0002-7

Ghiorso, M. S., & Gualda, G. A. R. (2015, June). An H_2O–CO_2 mixed fluid saturation model compatible with rhyolite-MELTS. *Contributions to Mineralogy and Petrology*, *169*(6), 53. Retrieved 2021-11-25, from `https://doi.org/10.1007/s00410-015-1141-8` doi: 10.1007/s00410-015-1141-8

Gleeson, M. L. M., Stock, M. J., Pyle, D. M., Mather, T. A., Hutchison, W., Yirgu, G., & Wade, J. (2017, May). Constraining magma storage conditions at a restless volcano in the Main Ethiopian Rift using phase equilibria models. *Journal of Volcanology and Geothermal Research*, *337*, 44–61. Retrieved 2018-10-24, from `http://www.sciencedirect.com/science/article/pii/S0377027316304383` doi: 10.1016/j.jvolgeores.2017.02.026

Gualda, G. A. R., Ghiorso, M. S., Lemons, R. V., & Carley, T. L. (2012, May). Rhyolite-MELTS: a Modified Calibration of MELTS Optimized for Silica-rich, Fluid-bearing Magmatic Systems. *Journal of Petrology*, *53*(5), 875–890. Retrieved 2021-03-24, from `https://doi.org/10.1093/petrology/egr080` doi: 10.1093/petrology/egr080

Gurenko, A. A., & Chaussidon, M. (1995, July). Enriched and depleted primitive melts included in olivine from Icelandic tholeiites: origin by continuous melting of a single mantle column. *Geochimica et Cosmochimica Acta*, *59*(14), 2905–2917. Retrieved 2021-12-09, from `https://www.sciencedirect.com/science/article/pii/0016703795001840` doi: 10.1016/0016-7037(95)00184-0

Hartley, M. E., Maclennan, J., Edmonds, M., & Thordarson, T. (2014, May). Reconstructing the deep CO_2 degassing behaviour of large basaltic fissure eruptions. *Earth and Planetary Science Letters*, *393*, 120–131. Retrieved 2018-02-16, from http://www.sciencedirect.com/science/article/pii/S0012821X14001125 doi: 10.1016/j.epsl.2014.02.031

Hauri, E., Wang, J., Dixon, J. E., King, P. L., Mandeville, C., & Newman, S. (2002, March). SIMS analysis of volatiles in silicate glasses: 1. Calibration, matrix effects and comparisons with FTIR. *Chemical Geology*, *183*(1), 99–114. Retrieved 2022-02-21, from https://www.sciencedirect.com/science/article/pii/S0009254101003758 doi: 10.1016/S0009-2541(01)00375-8

Head, E. M., Shaw, A. M., Wallace, P. J., Sims, K. W. W., & Carn, S. A. (2011). Insight into volatile behavior at Nyamuragira volcano (D.R. Congo, Africa) through olivine-hosted melt inclusions. *Geochemistry, Geophysics, Geosystems*, *12*(10). Retrieved 2022-01-17, from https://onlinelibrary.wiley.com/doi/abs/10.1029/2011GC003699 (_eprint: https://onlinelibrary.wiley.com/doi/pdf/10.1029/2011GC003699) doi: 10.1029/2011GC003699

Hudgins, T. R., Mukasa, S. B., Simon, A. C., Moore, G., & Barifaijo, E. (2015, April). Melt inclusion evidence for CO_2-rich melts beneath the western branch of the East African Rift: implications for long-term storage of volatiles in the deep lithospheric mantle. *Contributions to Mineralogy and Petrology*, *169*(5), 46. Retrieved 2020-09-15, from https://doi.org/10.1007/s00410-015-1140-9 doi: 10.1007/s00410-015-1140-9

Hunt, J. A., Zafu, A., Mather, T. A., Pyle, D. M., & Barry, P. H. (2017, October). Spatially Variable CO_2 Degassing in the Main Ethiopian Rift: Implications for Magma Storage, Volatile Transport, and Rift-Related Emissions. *Geochemistry, Geophysics, Geosystems*, *18*(10), 3714–3737. Retrieved 2018-08-07, from https://agupubs.onlinelibrary.wiley.com/doi/abs/10.1002/2017GC006975 doi: 10.1002/2017GC006975

Iacono-Marziano, G., Morizet, Y., Le Trong, E., & Gaillard, F. (2012, November). New experimental data and semi-empirical parameterization of H_2O–CO_2 solubility in mafic melts. *Geochimica et Cosmochimica Acta*, *97*, 1–23. Retrieved 2020-02-17, from http://www.sciencedirect.com/science/article/pii/S0016703712004930 doi: 10.1016/j.gca.2012.08.035

Iacovino, K., Matthews, S., Wieser, P. E., Moore, G. M., & Bégué, F. (2021). VESIcal Part I: An Open-Source Thermodynamic Model Engine for Mixed Volatile (H_2O-CO_2) Solubility in Silicate Melts. *Earth and Space Science*, *8*(11), e2020EA001584. Retrieved 2021-11-16, from https://onlinelibrary.wiley.com/doi/abs/10.1029/2020EA001584 (_eprint: https://onlinelibrary.wiley.com/doi/pdf/10.1029/2020EA001584) doi: 10.1029/2020EA001584

Iacovino, K., & Till, C. B. (2019, February). DensityX: A program for calculating the densities of magmatic liquids up to 1,627 °C and 30 kbar. *Volcanica*, *2*(1), 1–10. Retrieved 2021-03-04, from http://jvolcanica.org/ojs/index.php/volcanica/article/view/12 (Number: 1) doi: 10.30909/vol.02.01.0110

Iddon, F., & Edmonds, M. (2020). Volatile-Rich Magmas Distributed Through the Upper Crust in the Main Ethiopian Rift. *Geochemistry, Geophysics, Geosystems*, *21*(6), e2019–GC008904. Retrieved 2020-06-24, from https://agupubs.onlinelibrary.wiley.com/doi/abs/10.1029/2019GC008904 (_eprint: https://agupubs.onlinelibrary.wiley.com/doi/pdf/10.1029/2019GC008904) doi: 10.1029/2019GC008904

Iddon, F., Jackson, C., Hutchison, W., Fontijn, K., Pyle, D. M., Mather, T. A., … Edmonds, M. (2019). Mixing and Crystal Scavenging in the Main Ethiopian Rift Revealed by Trace Element Systematics in Feldspars and Glasses. *Geochemistry, Geophysics, Geosystems*, *20*(1), 230–259. Retrieved 2019-10-02, from https://agupubs.onlinelibrary.wiley.com/doi/abs/10.1029/2018GC007836 doi: 10.1029/2018GC007836

Jarosewich, E. (2002). Smithsonian Microbeam Standards. *Journal of Research* *of the National Institute of Standards and Technology*, *107*(6), 681–685. Retrieved 2022-02-21, from https://www.ncbi.nlm.nih.gov/pmc/articles/PMC4863845/ doi: 10.6028/jres.107.054

Jochum, K. P., Stoll, B., Herwig, K., Willbold, M., Hofmann, A. W., Amini, M., … Woodhead, J. D. (2006). MPI-DING reference glasses for in situ microanalysis: New reference values for element concentrations and isotope ratios. *Geochemistry, Geophysics, Geosystems*, *7*(2). Retrieved 2021-06-15, from https://agupubs.onlinelibrary.wiley.com/doi/abs/10.1029/2005GC001060 (_eprint: https://agupubs.onlinelibrary.wiley.com/doi/pdf/10.1029/2005GC001060) doi: 10.1029/2005GC001060

Keir, D., Ebinger, C. J., Stuart, G. W., Daly, E., & Ayele, A. (2006, May). Strain accommodation by magmatism and faulting as rifting proceeds to breakup: Seismicity of the northern Ethiopian rift. *Journal of Geophysical Research: Solid Earth*, *111*(B5). Retrieved 2018-11-01, from https://agupubs.onlinelibrary.wiley.com/doi/full/10.1029/2005JB003748 doi: 10.1029/2005JB003748

Kendall, J.-M., Stuart, G. W., Ebinger, C. J., Bastow, I. D., & Keir, D. (2005, January). Magma-assisted rifting in Ethiopia. *Nature*, *433*(7022), 146–148. Retrieved 2018-04-11, from https://www.nature.com/articles/nature03161 doi: 10.1038/nature03161

Keranen, K. M., Klemperer, S. L., Gloaguen, R., & EAGLE Working Group. (2004). Three-dimensional seismic imaging of a protoridge axis in the Main Ethiopian rift. *Geology*, *32*(11), 949. Retrieved 2018-11-01, from https://pubs.geoscienceworld.org/geology/article/32/11/949-952/103645 doi: 10.1130/G20737.1

Keranen, K. M., Klemperer, S. L., Julia, J., Lawrence, J. F., & Nyblade, A. A. (2009, May). Low lower crustal velocity across Ethiopia: Is the Main Ethiopian Rift a narrow rift in a hot craton? *Geochemistry, Geophysics, Geosystems*, *10*(5). Retrieved 2018-11-05, from https://agupubs.onlinelibrary.wiley.com/doi/abs/10.1029/2008GC002293 doi: 10.1029/2008GC002293

Lamadrid, H., Moore, L., Moncada, D., Rimstidt, J., Burruss, R., & Bodnar, R. (2017, February). Reassessment of the Raman CO_2 densimeter. *Chemical Geology*, *450*, 210–222. Retrieved 2020-02-09, from https://linkinghub.elsevier.com/retrieve/pii/S0009254116306945 doi: 10.1016/j.chemgeo.2016.12.034

Lavayssière, A., Rychert, C., Harmon, N., Keir, D., Hammond, J. O. S., Kendall, J.-M., … Leroy, S. (2018, October). Imaging Lithospheric Discontinuities Beneath the Northern East African Rift Using S-to-P Receiver Functions. *Geochemistry, Geophysics, Geosystems*. Retrieved 2018-11-19, from https://agupubs.onlinelibrary.wiley.com/doi/abs/10.1029/2018GC007463 doi: 10.1029/2018GC007463

Lavecchia, A., Beekman, F., Clark, S. R., & Cloetingh, S. A. P. L. (2016, August). Thermo-rheological aspects of crustal evolution during continental breakup and melt intrusion: The Main Ethiopian Rift, East Africa. *Tectonophysics*, *686*, 51–62. Retrieved 2022-06-01, from https://www.sciencedirect.com/science/article/pii/S0040195116302840 doi: 10.1016/j.tecto.2016.07.018

Le Corvec, N., Menand, T., & Lindsay, J. (2013). Interaction of ascending magma with pre-existing crustal fractures in monogenetic basaltic volcanism: an experimental approach. *Journal of Geophysical Research: Solid Earth*, *118*(3), 968–984. Retrieved 2022-11-25, from https://onlinelibrary.wiley.com/doi/abs/10.1002/jgrb.50142 (_eprint: https://onlinelibrary.wiley.com/doi/pdf/10.1002/jgrb.50142) doi: 10.1002/jgrb.50142

Lee, H., Muirhead, J. D., Fischer, T. P., Ebinger, C. J., Kattenhorn, S. A., Sharp,

Z. D., & Kianji, G. (2016, February). Massive and prolonged deep carbon emissions associated with continental rifting. *Nature Geoscience*, *9*(2), 145–149. Retrieved 2018-07-25, from https://www.nature.com/articles/ngeo2622 doi: 10.1038/ngeo2622

Le Voyer, M., Hauri, E. H., Cottrell, E., Kelley, K. A., Salters, V. J. M., Langmuir, C. H., ... Füri, E. (2018). Carbon fluxes and primary magma CO_2 contents along the global mid-ocean ridge system. *Geochemistry, Geophysics, Geosystems*, *20*(3), 1387–1424. Retrieved 2018-12-03, from https://agupubs.onlinelibrary.wiley.com/doi/abs/10.1029/2018GC007630 doi: 10.1029/2018GC007630

Maclennan, J. (2017, February). Bubble formation and decrepitation control the CO_2 content of olivine-hosted melt inclusions. *Geochemistry, Geophysics, Geosystems*, *18*(2), 597–616. Retrieved 2018-11-14, from https://agupubs.onlinelibrary.wiley.com/doi/abs/10.1002/2016GC006633 doi: 10.1002/2016GC006633

Magee, C., Muirhead, J. D., Karvelas, A., Holford, S. P., Jackson, C. A., Bastow, I. D., ... Shtukert, O. (2016, June). Lateral magma flow in mafic sill complexes. *Geosphere*, *12*(3), 809–841. Retrieved 2022-05-09, from https://doi.org/10.1130/GES01256.1 doi: 10.1130/GES01256.1

Maguire, P., Keller, G., Klemperer, S., Mackenzie, G., Keranen, K., Harder, S., ... Amha, M. (2006). Crustal structure of the northern Main Ethiopian Rift from the EAGLE controlled-source survey; a snapshot of incipient lithospheric break-up. In *The Afar Volcanic Province within the East African Rift System* (Vol. 259, pp. 269–292). Retrieved 2018-11-26, from http://sp.lyellcollection.org/lookup/doi/10.1144/GSL.SP.2006.259.01.21

Mazzarini, F., Rooney, T. O., & Isola, I. (2013, January). The intimate relationship between strain and magmatism: A numerical treatment of clustered monogenetic fields in the Main Ethiopian Rift. *Tectonics*, *32*(1), 49–64. Retrieved 2018-11-13, from http://doi.wiley.com/10.1029/2012TC003146 doi: 10.1029/2012TC003146

Mickus, K., Tadesse, K., Keller, G. R., & Oluma, B. (2007, June). Gravity analysis of the main Ethiopian rift. *Journal of African Earth Sciences*, *48*(2), 59–69. Retrieved 2021-11-30, from https://www.sciencedirect.com/science/article/pii/S1464343X07000192 doi: 10.1016/j.jafrearsci.2007.02.008

Moore, L. R., Gazel, E., Tuohy, R., Lloyd, A. S., Esposito, R., Steele-MacInnis, M., ... Bodnar, R. J. (2015, April). Bubbles matter: An assessment of the contribution of vapor bubbles to melt inclusion volatile budgets. *American Mineralogist*, *100*(4), 806–823. Retrieved 2019-05-13, from https://pubs.geoscienceworld.org/ammin/article/100/4/806-823/40390 doi: 10.2138/am-2015-5036

Moore, L. R., Mironov, N., Portnyagin, M., Gazel, E., & Bodnar, R. J. (2018, June). Volatile contents of primitive bubble-bearing melt inclusions from Klyuchevskoy volcano, Kamchatka: Comparison of volatile contents determined by mass-balance versus experimental homogenization. *Journal of Volcanology and Geothermal Research*, *358*, 124–131. Retrieved 2022-08-25, from https://www.sciencedirect.com/science/article/pii/S0377027317306510 doi: 10.1016/j.jvolgeores.2018.03.007

Muluneh, A. A., Brune, S., Illsley-Kemp, F., Corti, G., Keir, D., Glerum, A., ... Mori, J. (2020). Mechanism for Deep Crustal Seismicity: Insight From Modeling of Deformation Processes at the Main Ethiopian Rift. *Geochemistry, Geophysics, Geosystems*, *21*(7), e2020GC008935. Retrieved 2022-06-01, from https://onlinelibrary.wiley.com/doi/abs/10.1029/2020GC008935 (_eprint: https://onlinelibrary.wiley.com/doi/pdf/10.1029/2020GC008935) doi: 10.1029/2020GC008935

Muluneh, A. A., Keir, D., & Corti, G. (2021). Thermo-Rheological Properties of the Ethiopian Lithosphere and Evidence for Transient Fluid Induced Lower Crustal Seismicity Beneath the Ethiopian Rift. *Frontiers in Earth Science*, *9*. Retrieved 2022-06-01, from https://www.frontiersin.org/article/10.3389/feart.2021.610165

Neave, D. A., Fabbro, G., Herd, R. A., Petrone, C. M., & Edmonds, M. (2012, March). Melting, Differentiation and Degassing at the Pantelleria Volcano, Italy. *Journal of Petrology*, *53*(3), 637–663. Retrieved 2019-02-05, from https://academic.oup.com/petrology/article/53/3/637/1613886 doi: 10.1093/petrology/egr074

Newman, S., & Lowenstern, J. B. (2002, June). VolatileCalc: a silicate melt–H_2O–CO_2 solution model written in Visual Basic for excel. *Computers & Geosciences*, *28*(5), 597–604. Retrieved 2021-02-01, from http://www.sciencedirect.com/science/article/pii/S0098300401000814 doi: 10.1016/S0098-3004(01)00081-4

Nicotra, E., Viccaro, M., Donato, P., Acocella, V., & De Rosa, R. (2021, November). Catching the Main Ethiopian Rift evolving towards plate divergence. *Scientific Reports*, *11*(1), 21821. Retrieved 2021-11-09, from https://www.nature.com/articles/s41598-021-01259-6 (Bandiera_abtest: a Cc_license_type: cc_by Cg_type: Nature Research Journals Number: 1 Primary_atype: Research Publisher: Nature Publishing Group Subject_term: Petrology;Tectonics;Volcanology Subject_term_id: petrology;tectonics;volcanology) doi: 10.1038/s41598-021-01259-6

Oliveira, M. E., Gomes, A. S., Rosas, F. M., Duarte, J. C., França, G. S., Almeida, J. C., & Fuck, R. A. (2022, May). Impact of crustal rheology and inherited mechanical weaknesses on early continental rifting and initial evolution of double graben structural configurations: Insights from 2D numerical models. *Tectonophysics*, *831*, 229281. Retrieved 2022-12-10, from https://www.sciencedirect.com/science/article/pii/S0040195122000750 doi: 10.1016/j.tecto.2022.229281

Rasmussen, D. J., Plank, T. A., Wallace, P. J., Newcombe, M. E., & Lowenstern, J. B. (2020, December). Vapor-bubble growth in olivine-hosted melt inclusions. *American Mineralogist*, *105*(12), 1898–1919. Retrieved 2021-03-03, from https://pubs.geoscienceworld.org/msa/ammin/article/105/12/1898/592851/Vapor-bubble-growth-in-olivine-hosted-melt (Publisher: GeoScienceWorld) doi: 10.2138/am-2020-7377

Reiss, M. C., De Siena, L., & Muirhead, J. D. (2022). The Interconnected Magmatic Plumbing System of the Natron Rift. *Geophysical Research Letters*, *49*(15), e2022GL098922. Retrieved 2022-11-24, from https://onlinelibrary.wiley.com/doi/abs/10.1029/2022GL098922 (_eprint: https://onlinelibrary.wiley.com/doi/pdf/10.1029/2022GL098922) doi: 10.1029/2022GL098922

Reiss, M. C., Muirhead, J. D., Laizer, A., Link, F., Kazimoto, E., Ebinger, C. J., & Rümpker, G. (2021, February). The Impact of Complex Volcanic Plumbing on the Nature of Seismicity in the Developing Magmatic Natron Rift, Tanzania. *Frontiers in Earth Science*, *8*. doi: 10.3389/feart.2020.609805

Rooney, T. O., Bastow, I. D., & Keir, D. (2011, April). Insights into extensional processes during magma assisted rifting: Evidence from aligned scoria cones. *Journal of Volcanology and Geothermal Research*, *201*(1), 83–96. Retrieved 2018-02-02, from http://www.sciencedirect.com/science/article/pii/S0377027310002386 doi: 10.1016/j.jvolgeores.2010.07.019

Rooney, T. O., Furman, T., Yirgu, G., & Ayalew, D. (2005, August). Structure of the Ethiopian lithosphere: Xenolith evidence in the Main Ethiopian Rift. *Geochimica et Cosmochimica Acta*, *69*(15), 3889–3910. Retrieved 2018-10-25, from http://www.sciencedirect.com/science/article/pii/S0016703705003042 doi: 10.1016/j.gca.2005.03.043

Rooney, T. O., Wallace, P. J., Muirhead, J. D., Chiasera, B., Steiner, R. A., Girard, G., & Karson, J. A. (2022, November). Transition to magma-driven rifting in the South Turkana Basin, Kenya: Part 2. *Journal of the Geological Society*, *179*(6), jgs2021–160. Retrieved 2022-10-31, from `https://www.lyellcollection.org/doi/10.1144/jgs2021-160` doi: 10.1144/jgs2021-160

Saria, E., Calais, E., Stamps, D. S., Delvaux, D., & Hartnady, C. J. H. (2014, March). Present-day kinematics of the East African Rift. *Journal of Geophysical Research: Solid Earth*, *119*(4), 3584–3600. Retrieved 2018-11-01, from `https://agupubs.onlinelibrary.wiley.com/doi/full/10.1002/2013JB010901` doi: 10.1002/2013JB010901

Schneider, C. A., Rasband, W. S., & Eliceiri, K. W. (2012, July). NIH Image to ImageJ: 25 years of image analysis. *Nature Methods*, *9*(7), 671–675. Retrieved 2021-03-17, from `https://www.nature.com/articles/nmeth.2089` (Number: 7 Publisher: Nature Publishing Group) doi: 10.1038/nmeth.2089

Shishkina, T., Botcharnikov, R., Holtz, F., Almeev, R., & Portnyagin, M. (2010, October). Solubility of H_2O- and CO_2-bearing fluids in tholeiitic basalts at pressures up to 500MPa. *Chemical Geology*, *277*(1-2), 115–125. Retrieved 2021-09-10, from `https://linkinghub.elsevier.com/retrieve/pii/S0009254110002640` doi: 10.1016/j.chemgeo.2010.07.014

Shorttle, O., & Maclennan, J. (2011, November). Compositional trends of Icelandic basalts: Implications for short–length scale lithological heterogeneity in mantle plumes. *Geochemistry, Geophysics, Geosystems*, *12*(11), Q11008. Retrieved 2017-02-01, from `http://onlinelibrary.wiley.com/doi/10.1029/2011GC003748/abstract` doi: 10.1029/2011GC003748

Tadesse, A. Z., Ayalew, D., Pik, R., Yirgu, G., & Fontijn, K. (2019, January). Magmatic evolution of the Boku Volcanic Complex, Main Ethiopian Rift. *Journal of African Earth Sciences*, *149*, 109–130. Retrieved 2019-01-26, from `http://www.sciencedirect.com/science/article/pii/S1464343X18302450` doi: 10.1016/j.jafrearsci.2018.08.003

Tetreault, J. L., & Buiter, S. J. H. (2018, October). The influence of extension rate and crustal rheology on the evolution of passive margins from rifting to break-up. *Tectonophysics*, *746*, 155–172. Retrieved 2022-12-01, from `https://www.sciencedirect.com/science/article/pii/S0040195117303505` doi: 10.1016/j.tecto.2017.08.029

Thybo, H., & Nielsen, C. A. (2009, February). Magma-compensated crustal thinning in continental rift zones. *Nature*, *457*(7231), 873–876. Retrieved 2018-05-23, from `https://www.nature.com/articles/nature07688` doi: 10.1038/nature07688

Tucker, J. M., Hauri, E. H., Pietruszka, A. J., Garcia, M. O., Marske, J. P., & Trusdell, F. A. (2019, June). A high carbon content of the Hawaiian mantle from olivine-hosted melt inclusions. *Geochimica et Cosmochimica Acta*, *254*, 156–172. Retrieved 2019-05-15, from `http://www.sciencedirect.com/science/article/pii/S001670371930208X` doi: 10.1016/j.gca.2019.04.001

Wallace, P. J., Plank, T., Bodnar, R. J., Gaetani, G. A., & Shea, T. (2021). Olivine-Hosted Melt Inclusions: A Microscopic Perspective on a Complex Magmatic World. *Annual Review of Earth and Planetary Sciences*, *49*(1), null. Retrieved 2021-03-03, from `https://doi.org/10.1146/annurev-earth-082420-060506` (_eprint: https://doi.org/10.1146/annurev-earth-082420-060506) doi: 10.1146/annurev-earth-082420-060506

Weinstein, A., Oliva, S. J., Ebinger, C. J., Roecker, S., Tiberi, C., Aman, M., ... Fischer, T. P. (2017). Fault-magma interactions during early continental rifting: Seismicity of the Magadi-Natron-Manyara basins, Africa. *Geochemistry, Geophysics, Geosystems*, *18*(10), 3662–3686. Retrieved 2022-11-24, from `https://onlinelibrary.wiley.com/doi/abs/10.1002/2017GC007027` (_eprint: https://onlinelibrary.wiley.com/doi/pdf/10.1002/2017GC007027) doi: 10.1002/2017GC007027

Whaler, K. A., & Hautot, S. (2006, January). The electrical resistivity structure of the crust beneath the northern Main Ethiopian Rift. In G. Yirgu, C. J. Ebinger, & P. K. H. Maguire (Eds.), *The Afar Volcanic Province within the East African Rift System* (Vol. 259, pp. 293–305). Retrieved 2018-11-12, from http://sp.lyellcollection.org/content/259/1/293

White, R. S., Smith, L. K., Roberts, A. W., Christie, P. a. F., Kusznir, N. J., & the rest of the iSIMM Team. (2008, March). Lower-crustal intrusion on the North Atlantic continental margin. *Nature*, *452*(7186), 460–464. Retrieved 2018-05-13, from https://www.nature.com/articles/nature06687 doi: 10.1038/nature06687

Wieser, P. E., Iacovino, K., Matthews, S., Moore, G., & Allison, C. M. (2022). VESIcal: 2. A Critical Approach to Volatile Solubility Modeling Using an Open-Source Python3 Engine. *Earth and Space Science*, *9*(2), e2021EA001932. Retrieved 2022-07-14, from https://onlinelibrary.wiley.com/doi/abs/10.1029/2021EA001932 (_eprint: https://onlinelibrary.wiley.com/doi/pdf/10.1029/2021EA001932) doi: 10.1029/2021EA001932

Wieser, P. E., Lamadrid, H., Maclennan, J., Edmonds, M., Matthews, S., Iacovino, K., . . . Ilyinskaya, E. (2021). Reconstructing Magma Storage Depths for the 2018 Kilauean Eruption From Melt Inclusion CO_2 Contents: The Importance of Vapor Bubbles. *Geochemistry, Geophysics, Geosystems*, *22*(2), e2020GC009364. Retrieved 2021-02-13, from https://agupubs.onlinelibrary.wiley.com/doi/abs/10.1029/2020GC009364 (_eprint: https://agupubs.onlinelibrary.wiley.com/doi/pdf/10.1029/2020GC009364) doi: https://doi.org/10.1029/2020GC009364

Wong, K., Ferguson, D., Matthews, S., Morgan, D., Tadesse, A. Z., Sinetebeb, Y., & Yirgu, G. (2022, November). Exploring rift geodynamics in Ethiopia through olivine-spinel Al-exchange thermometry and rare-earth element distributions. *Earth and Planetary Science Letters*, *597*, 117820. Retrieved 2022-09-23, from https://www.sciencedirect.com/science/article/pii/S0012821X22004563 doi: 10.1016/j.epsl.2022.117820

References from the Supporting Information

(Schneider et al., 2012; Tucker et al., 2019; Wieser et al., 2021; Lamadrid et al., 2017; Hartley et al., 2014; Iacovino & Till, 2019; Moore et al., 2018, 2015; DeVitre et al., 2021; Hauri et al., 2002; Shishkina et al., 2010; Jochum et al., 2006; Jarosewich, 2002; J. J. Donovan, 2021; Danyushevsky & Plechov, 2011; Danyushevsky, 2001; Gleeson et al., 2017; DeVitre et al., 2022; Iacovino et al., 2021; Wieser et al., 2022; Ghiorso & Gualda, 2015; Iddon et al., 2019; Wong et al., 2022; Iddon & Edmonds, 2020; Dixon, 1997; Iacono-Marziano et al., 2012; Allison et al., 2019; Newman & Lowenstern, 2002; Gualda et al., 2012; Neave et al., 2012; Blundy & Wood, 1991; Saria et al., 2014; Le Voyer et al., 2018; Kendall et al., 2005; Bastow et al., 2010; Lavayssière et al., 2018; Daniels et al., 2014; Armitage et al., 2015; Hunt et al., 2017; Keir et al., 2006; Daly et al., 2008)

CReDiT: Author Contributions

- Conceptualization: KW, DF, DM, ME, GY
- Formal analysis: KW, DF, PW, ME
- Funding acquisition: KW, DF, DM, ME, GY
- Investigation: KW, DF, PW, JH, SH
- Resources: KW, DF, AZT, GY
- Supervision: DF, DM, ME, GY
- Visualization: KW, PW
- Writing – original draft: KW, DF
- Writing – review and editing: All authors

Supporting Information for "Focused mid-crustal magma intrusion during continental break-up in Ethiopia"

Kevin Wong[1], David Ferguson[1], Penny Wieser[2], Daniel Morgan[1], Marie Edmonds[3], Amdemichael Zafu Tadesse[4], Gezahegn Yirgu[5], Jason Harvey[1], and Samantha Hammond[6]

[1]School of Earth and Environment, University of Leeds, Leeds LS2 9JT, United Kingdom

[2]Earth and Planetary Science, University of California, Berkeley, CA 94720-4767, United States of America

[3]Centre for the Observation and Modelling of Earthquakes, Volcanoes and Tectonics (COMET), Department of Earth Sciences, University of Cambridge, Cambridge CB2 3EQ, United Kingdom

[4]Department of Geosciences, Environment and Society, Université Libre de Bruxelles, 50 B-1050 Bruxelles, Belgium

[5]School of Earth Sciences, Addis Ababa University, P. O. Box 1176 Addis Ababa, Ethiopia

[6]School of Environment, Earth and Ecosystems Sciences, The Open University, Milton Keynes MK7 6AA, United Kingdom

Contents of this file

Corresponding author: K. Wong, Dipartimento di Scienze Biologiche, Geologiche, e Ambientali (BiGeA), Alma Mater Studiorum Università di Bologna, Piazza di Porta San Donato 1, 40126, Bologna, Italy (kevin.wong@unibo.it)

2. Table S1

3. Figures S1 to S9

Additional Supporting Information (Files uploaded separately)

1. Dataset S1: standards and geochemical analyses of melt inclusions, whole rocks, and carrier glasses.

2. Transmitted and reflected light microscope images of analysed melt inclusions.

Introduction

The Supplementary Information contains text (Text S1) detailing analytical methods, expanded Raman spectroscopy results, volatile solubility and melt fractionation modelling, and CO_2 flux estimation calculations. Text S1 is complemented by Figures S1 to S9, and Table S1.

Text S1.

1. Analytical methods

Data, standards, secondary standards, and the accuracy and precision of all analyses on Main Ethiopian Rift (MER) materials are provided in Dataset S1.

1.1. Raman spectroscopy

Olivines hosting melt inclusions were picked from scoria from the two Boku Volcanic Complex localities shown in Figure 1 in the main text, and mounted onto glass slides using CrystalBond^{TM}. Crystals hosting melt inclusions with shrinkage bubbles were ground down until melt inclusions were within $\sim$100 μm of the surface, and then polished to 1 μm grade using silicon carbide papers and diamond pastes. Transmitted light optical microscopy was used to obtain high quality imagery of the melt inclusion and bubble. The outline of the bubble and melt inclusion were traced and fitted with ellipses using ImageJ to obtain dimensions for each (Schneider et al., 2012). Volumes of bubbles and melt inclusions were calculated assuming that the non-measurable dimension (orthogonal to the plane of polishing) was equal to the arithmetic mean of the two dimensions that could be measured. This introduces a 1σ error of +37/-47 % (Tucker et al., 2019), which dwarfs other uncertainties from Raman spectroscopy.

CO_2 densimetry of melt inclusion vapor bubbles was performed using the confocal Horiba LabRAM 300 Raman spectrometer at the Department of Earth Sciences, University of Cambridge over five days in February 2020, using a 100 mW 532.05 nm Ventus laser source focussed on the sample with an Olympus LMPLFLN 50$\times$ working distance objective lens. Spectra were collected with a Peltier front-illuminated 1024$\times$256 pixel

CCD detector with a holographic grating of 1800 gr/mm, a confocal aperture of 300 *mu*m, and a slit width of 100 *mu*m. Our analyses were performed at room temperature, and only CO_2 in the vapor bubble was considered in the Raman spectrum. The instrument was calibrated at the start of every day using the Labspec 6 autocalibration function, which assesses the linearity of the spectrum relative to the Si peak between 0 and 520.69 cm^{-1}. Spectra were collected within a single spectral window centered on 1250 cm^{-1}. Fermi diads obtained from Raman spectroscopy were fitted with Gaussian peaks after correcting for a fourth-order polynomial-fitted background, and diad splitting (Δ, in cm^{-1}) was determined through the difference of the means of the peaks. The relationship between diad splitting and CO_2 density (ρCO_2, in g cm^{-3}) has been previously assessed for this machine by Wieser et al. (2021) owing for the necessity of calibrating each individual Raman machine (Lamadrid et al., 2017), and takes the form of the following linear relation:

$$\rho_{\mathrm{CO_2}} = 0.3217\Delta - 32.9955 \tag{1}$$

The density of CO_2 in the bubble is converted into concentration through mass balance (Hartley et al., 2014):

$$[\mathrm{CO_2}] = 10^6 \times \frac{\rho_{\mathrm{CO_2}} \cdot V_{\mathrm{VB}}}{\rho_{\mathrm{melt}} \cdot V_{\mathrm{MI}}} \tag{2}$$

where V_{VB} and V_{MI} are the volume of the vapor bubble and the melt inclusion glass respectively, and $\rho_{\mathrm{melt}} = 2.706$ g cm^{-3} is the mean density of our melt inclusions determined using the software DensityX (Iacovino & Till, 2019). The total concentration of

CO_2 within the melt inclusion is then simply the sum of the CO_2 concentration in the bubble and the CO_2 concentration of the melt inclusion glass, which is assessed using SIMS (Supplement Section 2).

Removal of artifacts in the Raman spectrum was accomplished through multiple accumulations (5×60 s). Where signal strength of the Fermi diad was weak, longer count times were used at the expense of the number of accumulations (4×90 s). Each sample was run three times to obtain a mean and standard deviation; clear anomalies were not considered when computing the mean.

In addition to primary calibration performed every morning on a Si chip, secondary standards were measured at regular intervals throughout the day to check for instrument drift. The secondary standard used is a synthetic quartz-hosted fluid inclusion (label E) calibrated using an optical cell. Figure S1 shows repeat measurements of the Raman instrument over the course of a day, for five days. Precision in measuring bubble density was 5.8 %, and the accuracy relative to the mean diad splitting of (Wieser et al., 2021) was 0.9 %. Secondary standards were run with a shorter analysis time of 4×30 second accumulations as CO_2 diad signals were typically stronger than those of the samples. As with the samples, each secondary standard acquisition was measured three times to obtain a mean and standard deviation of repeat analyses. Mean peak splitting of the secondary standard appeared to be affected by instrument drift on some days (Figure S1); whether this results from temperature effects remains uncertain and should be explored in future studies using this Raman spectrometer. A linear correction was applied to data collected during the days where this effect is most prominent (12/02/2020 and 14/02/2020).

Dimensions of melt inclusions, their bubbles, and diad splitting are provided in Supplementary Dataset S1. All melt inclusion shrinkage bubbles analyzed for CO_2 returned a Fermi diad. ~35 % of bubbles produce Fermi diads with splittings corresponding to densities >0.20 g cm^{-3}. At room temperature, bubbles with densities greater than >~0.20–0.23 g cm^{-3} (depending on the exact temperature of the room and any heating from the laser) will consist of a vapor phase in the center with a density of 0.20–0.23 g cm^{-3} and a liquid CO_2 phase on the walls with a density of ~0.7 g cm^{-3}. The fact that we measure some densities above ~0.23 g cm^{-3} could represent analytical error; repeated measurements yielded standard deviations of ~0.04 cm^{-1} in diad splitting corresponding to standard deviations in density of ~0.01 g cm^{-3}; warmer room temperatures and small amounts of laser heating are also expected. As our bubbles were not heated above the critical point of CO_2 where a single phase is measured, our Raman measurements which only measure the interior vapor phase will underestimate the true density of the bubble (e.g., Moore et al., 2018). We do not observe any liquid films or 'bouncing bubbles': where the liquid phase is abundant enough Brownian motion causes the interior bubble to bounce. The absence of this motion suggests that if a liquid film were present, it is likely thin, so our measurements do not represent substantial underestimates.

~15 % of the shrinkage bubble Raman spectra contain a noticeable carbonate signature (~1090 cm^{-1}, see Figure S2; Moore et al., 2015; DeVitre et al., 2021). Only one bubble had a strong Raman carbonate signal, whereas the majority of carbonate signals were comparatively weak (Figure S2); we therefore believe that the presence of carbonate in MER melt inclusion shrinkage bubbles is fairly uncommon, and concentrations of carbonate are low when present. Owing to the overlap in CO_2 densities between bubbles that do and do not return a carbonate signature, we believe that the effect of sequestration of CO2 within carbonate is within uncertainty.

1.2. Secondary ion mass spectrometry (SIMS)

Crystals both with and without shrinkage bubbles were ground down to expose the melt inclusions. By doing so, most shrinkage bubbles were ruptured. The crystals were then mounted in epoxy blocks, and polished with progressively finer diamond pastes (culminating in 0.25 μm grade paste). In between each step of polishing the epoxy blocks were thoroughly cleaned through ultrasonication.

Volatile element and selected trace element concentrations were determined by secondary ion mass spectrometry (SIMS). The final stages of sample preparation and the SIMS analyses themselves were performed by Dr. Cristina Talavera Rodriguez using the Cameca IMS-7f-Geo at the NERC Ion Microprobe Facility, University of Edinburgh, owing to the COVID-19 pandemic. A gold coat was applied to the epoxy blocks, which were subsequently placed in the sample chamber at vacuum for several hours to allow for outgassing prior to the start of the analyses. SIMS was performed using a 5-6 nA 15 m diameter oval beam of O^- ions with an acceleration voltage of 13 kV. Positive secondary ions were accelerated to 5000 eV, with an offset of -50 eV for ^{12}C and -75 eV for ^{1}H and trace elements.

$^{26}Mg^+$, $^{30}Si^+$, $^{40}Ca^{2+}$, $^{85}Rb^+$, $^{88}Sr^+$, $^{89}Y^+$, $^{138}Ba^+$, $^{139}La^+$, and $^{140}Ce^+$ were counted for 2 seconds; $^{7}Li^+$ was counted for 3 seconds; $^{1}H^+$, $^{24}Mg^{2+}$, $^{93}Nb^+$, $^{141}Pr^+$, $^{143}Nd^+$, $^{157}Gd^+$, $^{159}Tb^+$, and $^{161}Dy^+$ were counted for 5 seconds; $^{149}Sm^+$, $^{171}Yb^+$, and $^{175}Lu^+$ were counted for 8 seconds; $^{12}C^{+}$ and $^{19}F^{+}$ were counted for 10 seconds. Counts were then normalized to 30Si and converted into concentrations. For C, 15 scans were performed, but only the last 8 were used to avoid surface contamination at the beginning of each analysis and to allow the C signal to stabilize. Similarly, 20 scans were performed for H from which the last 10 were used. As the ion yield of these two elements correlate with SiO_2, calibration curves were determined using a range of standards of variable SiO_2 (M40, N72, M36, M21, M5, M10, M47; Figure S3; Hauri et al., 2002; Shishkina et al., 2010). A background correction was applied by removing the number of counts for C and H_2O recorded by the CO_2- and H_2O-free standard N72 (Shishkina et al., 2010). General calibration was performed in every session using MPI-DING glasses (GSD-1, NIST610, KL2-G, ML3B; Jochum et al., 2006).

1.3. Electron probe microanalysis (EPMA)

Following SIMS analyses the gold coat was removed by polishing each epoxy block with 0.25 μm grade diamond paste for 2 minutes, and a carbon coat was applied for electron probe microanalysis (EPMA). Analyses to determine major element concentrations were performed on melt inclusions, matrix glasses, and host olivines using the JEOL JXA8230 at Leeds Electron Microscopy and Spectroscopy Centre (LEMAS), University of Leeds. Olivine analyses were performed using a 40 nA beam with 20 kV acceleration voltage; glass analyses, including both melt inclusions and carrier glasses, were performed using a defocused 5 μm beam with 15 kV acceleration voltage, with beam currents of 6 nA for Na and K and 15 nA for all other major elements. Spectrometer configurations, count times, calibration materials, and estimates of precision and accuracy from secondary standard analyses (olivine: San Carlos Olivine NMNH 111312-44; Jarosewich (2002); basaltic glass: ML3-B and KL2-G; Jochum et al. (2006)) are included in Supplementary Dataset S1. Data reduction is performed using the ProbeForEPMA software (Donovan, 2021).

1.4. Post-entrapment crystallization corrections

Melt inclusion post-entrapment crystallization and Fe-loss was corrected using Petrolog3 (Danyushevsky & Plechov, 2011). Initial FeO_t was set at 12.69 wt%, which is the mean FeO_t of carrier glasses from the Boku Volcanic Complex (see Supplementary Dataset S1). The olivine-melt model selected was (Danyushevsky, 2001), and the QFM buffer was chosen for the oxidation state (Gleeson et al., 2017). Changing the initial FeO_t by 1.5 wt% affects MagmaSat pressures by a mean of 8 ± 4 %, which does not significantly influence the results of this study.

1.5. X-ray fluorescence

A subset of scoria samples from cones in the Boku Volcanic Complex were powdered using an agate ball mill at the University of Leeds to 150 μm grade. X-ray fluorescence was performed using the Rigaku ZSX Primus WDXRF at the University of Leeds by Lesley Neve. Prior to analyses all samples were dried at 105 °C to remove remaining moisture. Loss on ignition was assessed at 1025 °C for at least one hour. A 1:10 ratio of sample:flux (comprising 66 % $Li_2B_4O_7$ and 34 % $LiBO_2$) supplemented with 3 drops of LiI was used to create fused beads. Sample-flux mixtures were cast at 1150 $\circ$C for 20 minutes in platinum crucibles to allow for the sample to dissolve. Once molten, the beads were allowed to cool to room temperature and cleaned with 25 % HCl. The standards USGS BCR-1 and STSD-4 were run at the start of the session and at regular intervals throughout. Detection limits were 0.03 wt% for MgO and Na2O, and 0.01 wt% for all other elements.

1.6. Solution ICP-MS

The samples powdered for XRF were digested in strong ultrapure acids (Romil UpA). Solution ICP-MS was performed using the Agilent 8800 QQQ at the Open University. To correct for plasma fractionation and drift, samples were run with internal standards (Be, Rh, In, Tm and Bi) bled in at the same time. Calibration standards were run at the start of the analytical period, followed by the samples. BHVO-2, JP-1, and WSE were analyzed as secondary standards. Monitors were analyzed every 5 unknowns to check for instrument drift. Detection limits were at most 0.012 μg g^{-1}.

2. Raman spectroscopy results

76 melt inclusion shrinkage bubbles analyzed by Raman spectroscopy returned a Fermi diad (Supplementary Dataset S1). Bubble CO_2 densities range from 0.12 to 0.27 g cm^{-3}, with a mean density of 0.19 g cm^{-3} (Figure S3), in excess of the expected detection limit for the Raman machine used (0.02 g cm^{-3} Wieser et al., 2021). Vapor bubbles constitute 0.09 to 2.85 vol% of the melt inclusion, and are similar in vol% to bubbles from Iceland (Hartley et al., 2014).

As shown in Figure S4 there are no clear correlations between bubble CO_2 density and melt inclusion volume (Figure S4A), bubble volume (Figure S4B), or bubble volume proportion of the melt inclusion (Figure S4C). Furthermore, in the samples where SIMS and subsequent EPMA has been performed, there is no correlation between bubble volume proportion and PEC as observed in melt inclusions from Hawaii (Wieser et al., 2021). No difference in bubble densities or melt inclusion and bubble dimensions were observed between the two cones sampled in our study.

2.1. Corrections for empty bubbles

Although 76 melt inclusion shrinkage bubbles were analyzed by Raman spectroscopy, a significant number could not be analyzed by SIMS owing to their small size. The melt inclusions considered in the main text of this study are therefore a mixture of samples that have been analyzed by Raman and others which were not, but were selected owing to their size. Several melt inclusions therefore have shrinkage bubbles that were not analyzed by Raman prior to SIMS.

We consider pressures from total CO_2 from these melt inclusions, assuming that their bubbles have CO_2 densities of 0.21 g cm^{-3}. This density falls near the mean of all melt inclusion vapor bubbles (0.18 g cm^{-3}), and could correspond to the maximum possible CO_2 vapor density below the critical point (DeVitre et al., 2022). We apply this maximum density with post-rupture measurements of the bubble to estimate total melt inclusion CO_2.

Nine melt inclusions are corrected in this manner, and seven are shown in Figure 2 of the main text as green diamonds with a trail leading to the pressure corresponding to the maximum vapor bubble CO_2 density. These seven inclusions have maximum pressures within the range 8–18 km, in agreement with our proposed focused intrusion zone of 10–15 km.

The remaining two melt inclusions, already recording the highest CO_2 in the dataset from glass analyses only, return maximum possible pressures nearing 10 kbar if bubble

CO_2 is estimated, i.e., under the MER crust and within the lithospheric mantle. For these two melt inclusions the bubble constitutes 6.5 vol% of the overall melt inclusion volume and make up more than twice the volume percentage of all other melt inclusion shrinkage bubbles (Figure S5). These samples may have significantly degassed, and may have been derived from deepest parts of the sub-rift magmatic system; these inclusions may also have co-entrapped magmatic bubbles and may not be suitable for estimating saturation pressures (e.g., Tucker et al., 2019). Tucker et al. (2019) note that one cannot differentiate between ensnared magmatic vapor bubbles and shrinkage bubbles that form after inclusion formation; in this study we err on the side of caution and do not estimate the pressures of these bubbles and inclusions in Figure 2 of the main text owing to their anomalous size relative to the other bubbles.

3. Volatile solubility modelling

The open-source Python 3 library VESIcal was used to determine volatile saturation pressures (Iacovino et al., 2021; Wieser et al., 2022), using the MagmaSat volatile saturation model (Ghiorso & Gualda, 2015). VESIcal models were run at a temperature of 1200 ∘C (Gleeson et al., 2017; Iddon et al., 2019; Wong et al., 2022) for all PEC-corrected melt inclusions in this study and for melt inclusions in Iddon and Edmonds (2020), assuming that PEC correction for this dataset was not necessary owing to the low reported PEC (<5 %). Uncertainties for volatile saturation pressure were determined using minimum and maximum CO_2 expected from 1σ melt inclusion volume uncertainty, which is the most significant uncertainty in our analyses. As shown in Figure S6, the primary control on determining saturation pressures for our melt inclusions using MagmaSat is CO_2 concentration. H_2O in our basaltic melt inclusions remains constant at 1.1±0.2 wt% up to ∼2 kbar (Figure S6).

Other saturation models have been calibrated for the composition and pressure ranges which our basaltic samples occupy. Figure S7 shows a comparison of MagmaSat compared to other basalt saturation models which are calibrated for our melt inclusion compositional range (Dixon, 1997; Shishkina et al., 2010; Iacono-Marziano et al., 2012; Allison et al., 2019). Both the Etna and Sunset Crater models of Allison et al. (2019) are selected owing to the broad calibration range of the former and the similarity in composition to our samples of the latter. For the majority of our melt inclusions the difference between a selected model and MagmaSat is typically less than 500 bars (∼2 km; see Figure S7). Kolmogotov-Smirnov statistics and p-values are presented in Table S1.

Entrapment pressures for melt inclusions calculated using MagmaSat and the models of Shishkina et al. (2010), Iacono-Marziano et al. (2012) and the Sunset Crater model of Allison et al. (2019) are statistically indistinguishable using Kolmogotov-Smirnov statistics at p=0.05 (Table S1). Owing to the compositional difference between our samples and the Etna basalt, the Allison et al. (2019) Etna model substantially underestimates pressures relative to other models (p <0.05 for all models except for Dixon, 1997, Table S1). Our samples fall on the North Arch Glasses regression line used to calibrate Dixon (1997) (and by extension the VolatileCalc model implemented in VESIcal; Newman & Lowenstern, 2002), and are therefore compositionally suitable for this solubility model. However, it has previously been suggested that this model is appropriate only for low H_2O and CO_2 contents and therefore low pressures (<1000 bar; Iacono-Marziano et al., 2012). As the majority of our melt inclusions are likely to be entrapped at mid-crustal depths, the model of Dixon (1997) is deemed inappropriate for this work. The differences between MagmaSat and the other empirical models of volatile saturation are statistically insignificant and our samples are expected to have fractionated within their calibrated temperature and pressure ranges (Figure S7). These other models typically fall within the uncertainty envelope of melt inclusion and bubble volumes. We therefore favor the fully thermodynamic parameterisation of MagmaSat over the other empirical models.

4. Fractionation models

Liquid lines of descent for major elements were predicted using RhyoliteMELTS v1.2.0 (Gualda et al., 2012), using the three most primitive melt inclusion compositions as starting compositions. Models were run at an oxygen fugacity range of QFM-2 to QFM+1, which is characteristic of MER basalts (e.g., Gleeson et al., 2017). Pressures of fractionation of 2–4 kbars were selected based on the pressures obtained from VESIcal for melt inclusions for which total CO_2 was determined (see above). Model differences arising from starting oxygen fugacity and pressure were minor and are therefore not considered further. Trace element partitioning was modeled using the Rayleigh fractionation equation:

$$C = C_0 \cdot F^{(D-1)} \tag{3}$$

Where C_0 is the original concentration of an element, F is the melt fraction, and D is the bulk mineral-melt distribution coefficient. Melt fraction and mass proportions of olivine, clinopyroxene and plagioclase feldspar were determined from RhyoliteMELTS outputs; other mineral fractions were typically <5 wt% and hence were not considered.

Mineral-melt distribution coefficients were collated from Neave, Fabbro, Herd, Petrone, and Edmonds (2012) and Iddon and Edmonds (2020), and, other than Ba and Sr in plagioclase, were assumed to be constant. Distribution coefficients for Ba and Sr in plagioclase were calculated using the temperature-dependent partitioning of Blundy and Wood (1991).

5. CO_2 flux estimates

To estimate CO_2 fluxes resulting from the degassing of our melt inclusions, we estimate the quantity of melts supplied to the MER. The length of the MER is ∼1000 km, and the full spreading rate is ∼5.0 mm yr^{-1} (Saria et al., 2014). Assuming a melt density of 2700 kg m^{-3} (calculated as our mean melt inclusion density using DensityX; Iacovino & Till, 2019), and that the CO_2 degassed at mid-crustal pressures is 2.0±0.6 wt% (assuming same CO_2/Ba as MORB; Le Voyer et al., 2018), we consider three possible estimates of intruded melt thickness per unit of rift length:

- Firstly, we can assume that all new rifting crust is igneous; this is a suitable estimate as most present-day extension in the MER is predominantly magma-assisted (e.g., Kendall et al., 2005; Bastow et al., 2010). Using a crustal thickness of 28 km (Lavayssière et al., 2018), we estimate melt volume flux as 0.14 km^3 yr^{-1}, and a CO_2 flux of 7.6±2.7 Mt CO_2 yr^{-1}.

- Secondly, we can assume that 50% of extension in the MER is accommodated by magmatic intrusion (Daniels et al., 2014). If this is the case, melt volume flux and CO_2 flux are simply half that of the previous case: 0.07 km^3 yr^{-1} and 3.8±1.1 Mt CO_2 yr^{-1} respectively.

• Finally, we can calculate the proportion of igneous crust in rifting crust by comparing crustal thicknesses expected from stretching factors to present-day MER crustal thickness (Armitage et al., 2015; Wong et al., 2022). Using an intruded melt thickness of 3–6 km calculated from an estimated MER stretch factor of 1.2–1.5 (Wong et al., 2022), performing the calculations as above provides melt volume flux estimates of 0.02–0.03 km^3 y^{-1}, and corresponding CO_2 flux estimates of 0.8±0.2 Mt CO_2 yr^{-1} (assuming 3 km), 1.2±0.4 Mt CO_2 yr^{-1} (assuming 4.5 km), and 1.6±0.5 Mt CO_2 yr^{-1} (assuming 6 km).

Our melt volume flux estimates, ranging from 0.02 to 0.14 km^3 yr^{-1}, are similar to the range estimated by Iddon and Edmonds (2020). Similarly, our CO_2 flux estimates, which range from 0.8 to 7.6 Mt CO_2 yr^{-1}, are of a similar magnitude to total CO_2 emissions of 0.52–4.36 Mt CO_2 yr^{-1} recorded by Hunt, Zafu, Mather, Pyle, and Barry (2017). We conclude therefore that the degassing of mid-crustal sill complexes can supply sufficient CO_2 to match the quantity degassed at geothermal centers in the MER.

References

Allison, C. M., Roggensack, K., & Clarke, A. B. (2019, June). H_2O–CO_2 solubility in alkali-rich mafic magmas: new experiments at mid-crustal pressures. *Contributions to Mineralogy and Petrology*, *174*(7), 58. Retrieved 2022-02-01, from `https://doi.org/10.1007/s00410-019-1592-4` doi: 10.1007/s00410-019-1592-4

Armitage, J. J., Ferguson, D. J., Goes, S., Hammond, J. O. S., Calais, E., Rychert, C. A., & Harmon, N. (2015, May). Upper mantle temperature and the onset of extension and break-up in Afar, Africa. *Earth and Planetary Science Letters*, *418*, 78–90. Retrieved 2018-10-03, from http://www.sciencedirect.com/science/article/pii/S0012821X15001259 doi: 10.1016/j.epsl.2015.02.039

Bastow, I. D., Pilidou, S., Kendall, J.-M., & Stuart, G. W. (2010, June). Melt-induced seismic anisotropy and magma assisted rifting in Ethiopia: Evidence from surface waves. *Geochemistry, Geophysics, Geosystems*, *11*(6). Retrieved 2018-11-02, from https://agupubs.onlinelibrary.wiley.com/doi/full/10.1029/2010GC003036 doi: 10.1029/2010GC003036

Blundy, J. D., & Wood, B. J. (1991, January). Crystal-chemical controls on the partitioning of Sr and Ba between plagioclase feldspar, silicate melts, and hydrothermal solutions. *Geochimica et Cosmochimica Acta*, *55*(1), 193–209. Retrieved 2017-05-25, from http://www.sciencedirect.com/science/article/pii/001670379190411W doi: 10.1016/0016-7037(91)90411-W

Daly, E., Keir, D., Ebinger, C. J., Stuart, G. W., Bastow, I. D., & Ayele, A. (2008, March). Crustal tomographic imaging of a transitional continental rift: The Ethiopian rift. *Geophysical Journal International*, *172*(3), 1033–1048. Retrieved 2018-11-01, from https://academic.oup.com/gji/article/172/3/1033/571185 doi: 10.1111/j.1365-246X.2007.03682.x

Daniels, K. A., Bastow, I. D., Keir, D., Sparks, R. S. J., & Menand, T. (2014, January). Thermal models of dyke intrusion during development of continent–ocean transition. *Earth and Planetary Science Letters*, *385*, 145–153. Retrieved 2018-11-22, from http://www.sciencedirect.com/science/article/pii/S0012821X13005293 doi: 10.1016/j.epsl.2013.09.018

Danyushevsky, L. V. (2001, October). The effect of small amounts of H_2O on crystallisation of mid-ocean ridge and backarc basin magmas. *Journal of Volcanology and Geothermal Research*, *110*(3), 265–280. Retrieved 2021-03-30, from https://www.sciencedirect.com/science/article/pii/S037702730100213X doi: 10.1016/S0377-0273(01)00213-X

Danyushevsky, L. V., & Plechov, P. (2011, July). Petrolog3: Integrated software for modeling crystallization processes. *Geochemistry, Geophysics, Geosystems*, *12*(7), Q07021. Retrieved 2017-12-02, from http://onlinelibrary.wiley.com/doi/10.1029/2011GC003516/abstract doi: 10.1029/2011GC003516

DeVitre, C. L., Barth, A., Gazel, E., Plank, T. A., & Ramalho, R. (2021, December). Solving the Carbonate Problem in Melt Inclusion Bubbles. In *AGU Fall Meeting Abstracts.* Retrieved from https://agu.confex.com/agu/fm21/meetingapp.cgi/Paper/845682

DeVitre, C. L., Dayton, K., Gazel, E., Barth, A., Plank, T. A., Pamukcu, A., . . . Monteleone, B. (2022, July). Accounting for Multi-Phase Carbon in Melt Inclusion Bubbles. In *Goldschmidt Conference Abstracts.* Retrieved 2022-08-08, from https://conf.goldschmidt.info/goldschmidt/2022/meetingapp.cgi/Paper/12601

Dixon, J. E. (1997, April). Degassing of alkalic basalts. *American Mineralogist*, *82*(3-4), 368–378. Retrieved 2022-01-05, from https://pubs.geoscienceworld.org/ammin/article/82/3-4/368-378/43291 doi: 10.2138/am-1997-3-415

Donovan, J. J. (2021). *Probe for EPMA v. 13.0.5 User's Guide and Reference (Xtreme Edition).* Retrieved 2022-06-07, from https://probesoftware.com/download/

PROBEWIN.pdf

Ghiorso, M. S., & Gualda, G. A. R. (2015, June). An H_2O–CO_2 mixed fluid saturation model compatible with rhyolite-MELTS. *Contributions to Mineralogy and Petrology*, *169*(6), 53. Retrieved 2021-11-25, from https://doi.org/10.1007/s00410-015-1141-8 doi: 10.1007/s00410-015-1141-8

Gleeson, M. L. M., Stock, M. J., Pyle, D. M., Mather, T. A., Hutchison, W., Yirgu, G., & Wade, J. (2017, May). Constraining magma storage conditions at a restless volcano in the Main Ethiopian Rift using phase equilibria models. *Journal of Volcanology and Geothermal Research*, *337*, 44–61. Retrieved 2018-10-24, from http://www.sciencedirect.com/science/article/pii/S0377027316304383 doi: 10.1016/j.jvolgeores.2017.02.026

Gualda, G. A. R., Ghiorso, M. S., Lemons, R. V., & Carley, T. L. (2012, May). Rhyolite-MELTS: a Modified Calibration of MELTS Optimized for Silica-rich, Fluid-bearing Magmatic Systems. *Journal of Petrology*, *53*(5), 875–890. Retrieved 2021-03-24, from https://doi.org/10.1093/petrology/egr080 doi: 10.1093/petrology/egr080

Hartley, M. E., Maclennan, J., Edmonds, M., & Thordarson, T. (2014, May). Reconstructing the deep CO_2 degassing behaviour of large basaltic fissure eruptions. *Earth and Planetary Science Letters*, *393*, 120–131. Retrieved 2018-02-16, from http://www.sciencedirect.com/science/article/pii/S0012821X14001125 doi: 10.1016/j.epsl.2014.02.031

Hauri, E., Wang, J., Dixon, J. E., King, P. L., Mandeville, C., & Newman, S. (2002, March). SIMS analysis of volatiles in silicate glasses: 1. Calibration, matrix effects and comparisons with FTIR. *Chemical Geology*, *183*(1), 99–114. Retrieved 2022-02-21, from https://www.sciencedirect.com/science/article/pii/S0009254101003758 doi: 10.1016/S0009-2541(01)00375-8

Hunt, J. A., Zafu, A., Mather, T. A., Pyle, D. M., & Barry, P. H. (2017, October). Spatially Variable CO_2 Degassing in the Main Ethiopian Rift: Implications for Magma Storage, Volatile Transport, and Rift-Related Emissions. *Geochemistry, Geophysics, Geosystems*, *18*(10), 3714–3737. Retrieved 2018-08-07, from https://agupubs.onlinelibrary.wiley.com/doi/abs/10.1002/2017GC006975 doi: 10.1002/2017GC006975

Iacono-Marziano, G., Morizet, Y., Le Trong, E., & Gaillard, F. (2012, November). New experimental data and semi-empirical parameterization of H_2O–CO_2 solubility in mafic melts. *Geochimica et Cosmochimica Acta*, *97*, 1–23. Retrieved 2020-02-17, from http://www.sciencedirect.com/science/article/pii/S0016703712004930 doi: 10.1016/j.gca.2012.08.035

Iacovino, K., Matthews, S., Wieser, P. E., Moore, G. M., & Bégué, F. (2021). VESIcal Part I: An Open-Source Thermodynamic Model Engine for Mixed Volatile (H_2O-CO_2) Solubility in Silicate Melts. *Earth and Space Science*, *8*(11), e2020EA001584. Retrieved 2021-11-16, from https://onlinelibrary.wiley.com/doi/abs/10.1029/2020EA001584 (_eprint: https://onlinelibrary.wiley.com/doi/pdf/10.1029/2020EA001584) doi: 10.1029/2020EA001584

Iacovino, K., & Till, C. B. (2019, February). DensityX: A program for calculating the densities of magmatic liquids up to 1,627 °C and 30 kbar. *Volcanica*, *2*(1), 1–10. Retrieved 2021-03-04, from http://jvolcanica.org/ojs/index.php/volcanica/article/view/12 (Number: 1) doi: 10.30909/vol.02.01.0110

Iddon, F., & Edmonds, M. (2020). Volatile-Rich Magmas Distributed Through the Upper Crust in the Main Ethiopian Rift. *Geochemistry, Geophysics, Geosystems*, *21*(6), e2019–GC008904. Retrieved 2020-06-24, from https://agupubs.onlinelibrary.wiley.com/doi/abs/10.1029/2019GC008904 (_eprint: https://agupubs.onlinelibrary.wiley.com/doi/pdf/10.1029/2019GC008904) doi: 10.1029/2019GC008904

Iddon, F., Jackson, C., Hutchison, W., Fontijn, K., Pyle, D. M., Mather, T. A., ... Edmonds, M. (2019). Mixing and Crystal Scavenging in the Main Ethiopian Rift Revealed by Trace Element Systematics in Feldspars and Glasses. *Geochemistry, Geophysics, Geosystems*, *20*(1), 230–259. Retrieved 2019-10-02, from https://agupubs.onlinelibrary.wiley.com/doi/abs/10.1029/2018GC007836 doi: 10.1029/2018GC007836

Jarosewich, E. (2002). Smithsonian Microbeam Standards. *Journal of Research of the National Institute of Standards and Technology*, *107*(6), 681–685. Retrieved 2022-02-21, from https://www.ncbi.nlm.nih.gov/pmc/articles/PMC4863845/ doi: 10.6028/jres.107.054

Jochum, K. P., Stoll, B., Herwig, K., Willbold, M., Hofmann, A. W., Amini, M., ... Woodhead, J. D. (2006). MPI-DING reference glasses for in situ microanalysis: New reference values for element concentrations and isotope ratios. *Geo-*

chemistry, Geophysics, Geosystems, *7*(2). Retrieved 2021-06-15, from https://agupubs.onlinelibrary.wiley.com/doi/abs/10.1029/2005GC001060 (_eprint: https://agupubs.onlinelibrary.wiley.com/doi/pdf/10.1029/2005GC001060) doi: 10.1029/2005GC001060

Keir, D., Ebinger, C. J., Stuart, G. W., Daly, E., & Ayele, A. (2006, May). Strain accommodation by magmatism and faulting as rifting proceeds to breakup: Seismicity of the northern Ethiopian rift. *Journal of Geophysical Research: Solid Earth*, *111*(B5). Retrieved 2018-11-01, from https://agupubs.onlinelibrary.wiley.com/doi/full/10.1029/2005JB003748 doi: 10.1029/2005JB003748

Kendall, J.-M., Stuart, G. W., Ebinger, C. J., Bastow, I. D., & Keir, D. (2005, January). Magma-assisted rifting in Ethiopia. *Nature*, *433*(7022), 146–148. Retrieved 2018-04-11, from https://www.nature.com/articles/nature03161 doi: 10.1038/nature03161

Lamadrid, H., Moore, L., Moncada, D., Rimstidt, J., Burruss, R., & Bodnar, R. (2017, February). Reassessment of the Raman CO_2 densimeter. *Chemical Geology*, *450*, 210–222. Retrieved 2020-02-09, from https://linkinghub.elsevier.com/retrieve/pii/S0009254116306945 doi: 10.1016/j.chemgeo.2016.12.034

Lavayssière, A., Rychert, C., Harmon, N., Keir, D., Hammond, J. O. S., Kendall, J.-M., … Leroy, S. (2018, October). Imaging Lithospheric Discontinuities Beneath the Northern East African Rift Using S-to-P Receiver Functions. *Geochemistry, Geophysics, Geosystems*. Retrieved 2018-11-19, from https://agupubs.onlinelibrary.wiley.com/doi/abs/10.1029/2018GC007463 doi: 10.1029/2018GC007463

Le Voyer, M., Hauri, E. H., Cottrell, E., Kelley, K. A., Salters, V. J. M., Langmuir, C. H., … Füri, E. (2018). Carbon fluxes and primary magma CO_2 contents along the global mid-ocean ridge system. *Geochemistry, Geophysics, Geosystems*, *20*(3), 1387–1424. Retrieved 2018-12-03, from https://agupubs.onlinelibrary.wiley.com/doi/abs/10.1029/2018GC007630 doi: 10.1029/2018GC007630

Moore, L. R., Gazel, E., Tuohy, R., Lloyd, A. S., Esposito, R., Steele-MacInnis, M., … Bodnar, R. J. (2015, April). Bubbles matter: An assessment of the contribution of vapor bubbles to melt inclusion volatile budgets. *American Mineralogist*, *100*(4), 806–823. Retrieved 2019-05-13, from https://pubs.geoscienceworld.org/ammin/article/100/4/806-823/40390 doi: 10.2138/am-2015-5036

Moore, L. R., Mironov, N., Portnyagin, M., Gazel, E., & Bodnar, R. J. (2018, June). Volatile contents of primitive bubble-bearing melt inclusions from Klyuchevskoy volcano, Kamchatka: Comparison of volatile contents determined by mass-balance versus experimental homogenization. *Journal of Volcanology and Geothermal Research*, *358*, 124–131. Retrieved 2022-08-25, from https://www.sciencedirect.com/science/article/pii/S0377027317306510 doi: 10.1016/j.jvolgeores.2018.03.007

Neave, D. A., Fabbro, G., Herd, R. A., Petrone, C. M., & Edmonds, M. (2012, March). Melting, Differentiation and Degassing at the Pantelleria Volcano, Italy. *Journal of Petrology*, *53*(3), 637–663. Retrieved 2019-02-05, from https://academic.oup.com/petrology/article/53/3/637/1613886 doi: 10.1093/petrology/egr074

Newman, S., & Lowenstern, J. B. (2002, June). VolatileCalc: a silicate melt–H_2O–CO_2 solution model written in Visual Basic for excel. *Computers & Geosciences*, *28*(5), 597–604. Retrieved 2021-02-01, from http://www.sciencedirect.com/science/article/pii/S0098300401000814 doi: 10.1016/S0098-3004(01)00081-4

Saria, E., Calais, E., Stamps, D. S., Delvaux, D., & Hartnady, C. J. H. (2014, March). Present-day kinematics of the East African Rift. *Journal of Geophysical Research: Solid Earth*, *119*(4), 3584–3600. Retrieved 2018-11-01, from https://agupubs.onlinelibrary.wiley.com/doi/full/10.1002/2013JB010901 doi: 10.1002/2013JB010901

Schneider, C. A., Rasband, W. S., & Eliceiri, K. W. (2012, July). NIH Image to ImageJ: 25 years of image analysis. *Nature Methods*, *9*(7), 671–675. Retrieved 2021-03-17, from https://www.nature.com/articles/nmeth.2089 (Number: 7 Publisher: Nature Publishing Group) doi: 10.1038/nmeth.2089

Shishkina, T., Botcharnikov, R., Holtz, F., Almeev, R., & Portnyagin, M. (2010, October). Solubility of H_2O- and CO_2-bearing fluids in tholeiitic basalts at pressures up to 500MPa. *Chemical Geology*, *277*(1-2), 115–125. Retrieved 2021-09-10, from https://linkinghub.elsevier.com/retrieve/pii/S0009254110002640 doi: 10.1016/j.chemgeo.2010.07.014

Tucker, J. M., Hauri, E. H., Pietruszka, A. J., Garcia, M. O., Marske, J. P., & Trusdell, F. A. (2019, June). A high carbon content of the Hawaiian mantle from olivine-hosted melt inclusions. *Geochimica et Cosmochimica Acta*, *254*, 156–172. Retrieved 2019-05-15, from http://www.sciencedirect.com/science/article/pii/S001670371930208X doi: 10.1016/j.gca.2019.04.001

Wieser, P. E., Iacovino, K., Matthews, S., Moore, G., & Allison, C. M. (2022). VESIcal: 2. A Critical Approach to Volatile Solubility Modeling Using an Open-Source Python3 Engine. *Earth and Space Science*, *9*(2), e2021EA001932. Retrieved 2022-07-14, from `https://onlinelibrary.wiley.com/doi/abs/10.1029/2021EA001932` (_eprint: https://onlinelibrary.wiley.com/doi/pdf/10.1029/2021EA001932) doi: 10.1029/2021EA001932

Wieser, P. E., Lamadrid, H., Maclennan, J., Edmonds, M., Matthews, S., Iacovino, K., ... Ilyinskaya, E. (2021). Reconstructing Magma Storage Depths for the 2018 Kilauean Eruption From Melt Inclusion CO_2 Contents: The Importance of Vapor Bubbles. *Geochemistry, Geophysics, Geosystems*, *22*(2), e2020GC009364. Retrieved 2021-02-13, from `https://agupubs.onlinelibrary.wiley.com/doi/abs/10.1029/2020GC009364` (_eprint: https://agupubs.onlinelibrary.wiley.com/doi/pdf/10.1029/2020GC009364) doi: https://doi.org/10.1029/2020GC009364

Wong, K., Ferguson, D., Matthews, S., Morgan, D., Tadesse, A. Z., Sinetebeb, Y., & Yirgu, G. (2022, November). Exploring rift geodynamics in Ethiopia through olivine-spinel Al-exchange thermometry and rare-earth element distributions. *Earth and Planetary Science Letters*, *597*, 117820. Retrieved 2022-09-23, from `https://www.sciencedirect.com/science/article/pii/S0012821X22004563` doi: 10.1016/j.epsl.2022.117820

Table S1. Kolmogorov-Smirnov statistics and p-values (in brackets) for different solubility models applied to our melt inclusions (see also Figure S7). Abbreviations are as follows: I.-M.: Iacono-Marziano et al. (2012); Allison-E: Allison et al. (2019) Etna model; Allison-S: Allison et al. (2019) Sunset Crater model.

K-S stat. (p)	**MagmaSat**	**Dixon**	**I.-M.**	**Shishkina**	**Allison-E**
Dixon	0.33 (0.03)	-	-	-	-
Iacono-Marziano	0.15 (0.77)	0.25 (0.16)	-	-	-
Shishkina	0.18 (0.58)	0.40 ($3{\cdot}10^{-3}$)	0.23 (0.27)	-	-
Allison-E	0.40 ($3{\cdot}10^{-3}$)	0.23 (0.27)	0.38 ($6{\cdot}10^{-3}$)	0.55 ($7{\cdot}10^{-6}$)	-
Allison-S	0.08 (1.00)	0.33 (0.03)	0.18 (0.58)	0.15 (0.77)	0.40 ($3{\cdot}10^{-3}$)

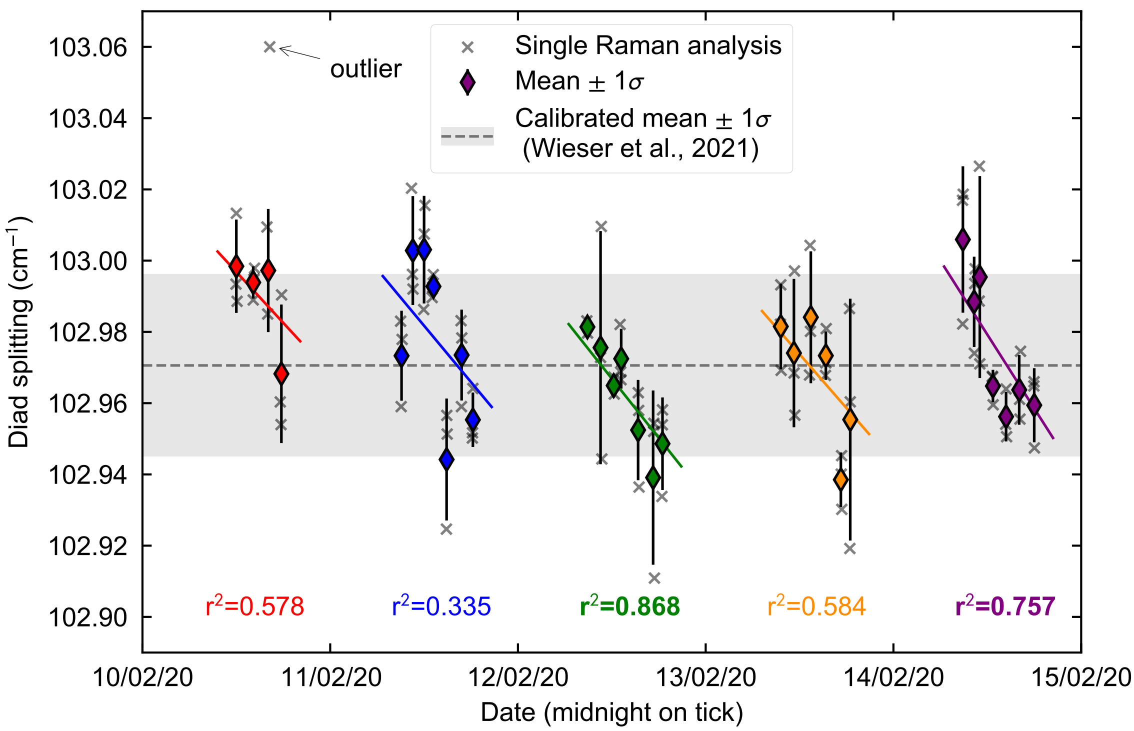

Figure S1. Secondary standard measurements on a synthetic quartz-hosted fluid inclusion used by (Wieser et al., 2021). Regression lines are fitted to analysis means.

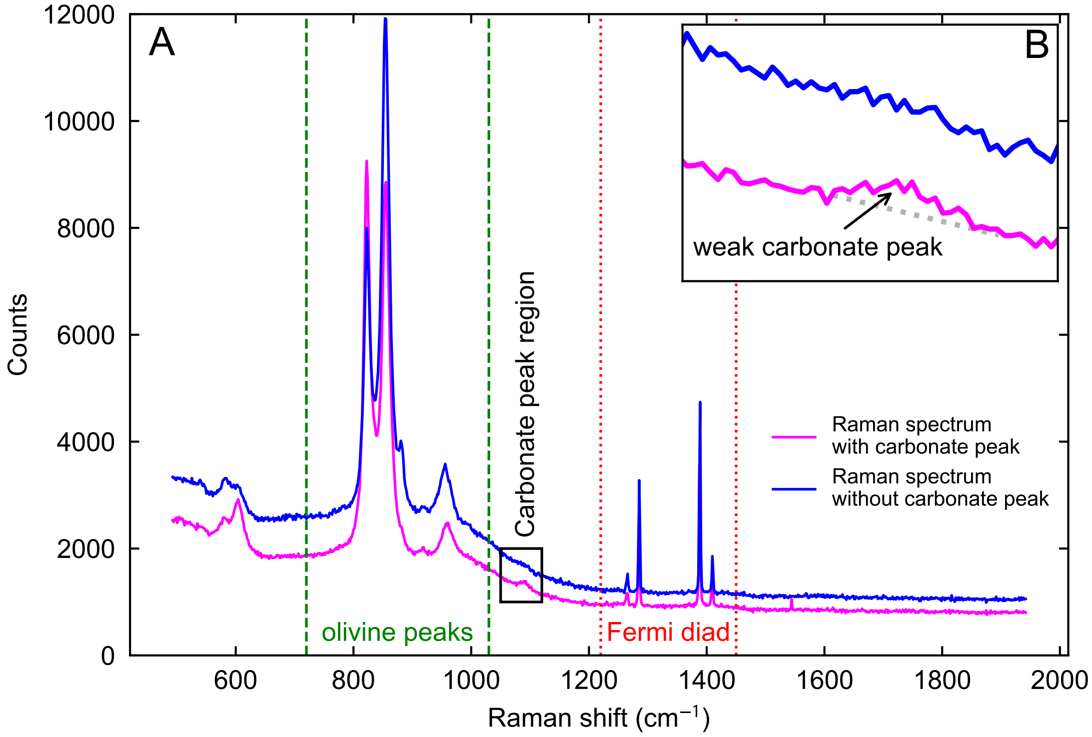

Figure S2. A. Raman spectra from this study with and without a carbonate peak at $\sim$1090 cm^{-1}. The region of the olivine peaks and Fermi diad are shown as the dashed and dotted regions respectively. B. Zoom inset on black rectangle in Subfigure A.

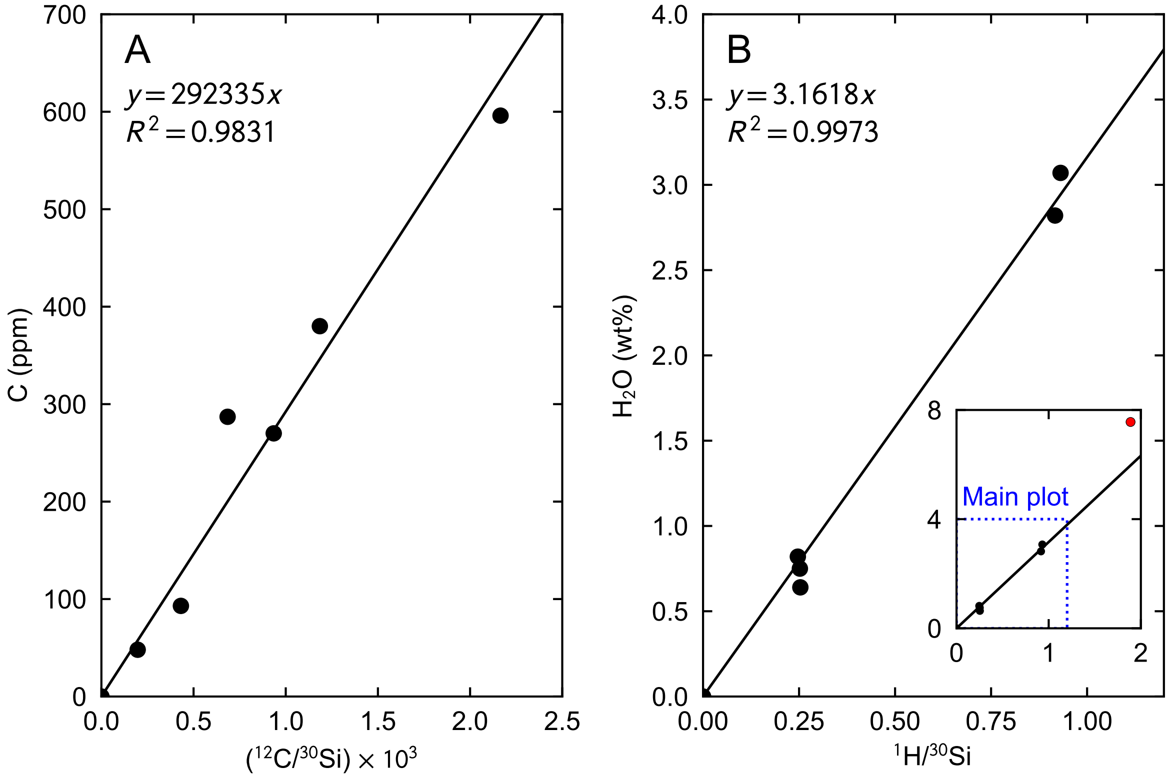

Figure S3. Calibration lines for basaltic standards used to convert measured counts of A) C and B) H_2O into concentrations. The subplot in subfigure B illustrates the position of the glass standard M21, which is shown as a red marker and was not used to determine the calibration line as its H2O concentration significantly exceeded those within our samples.

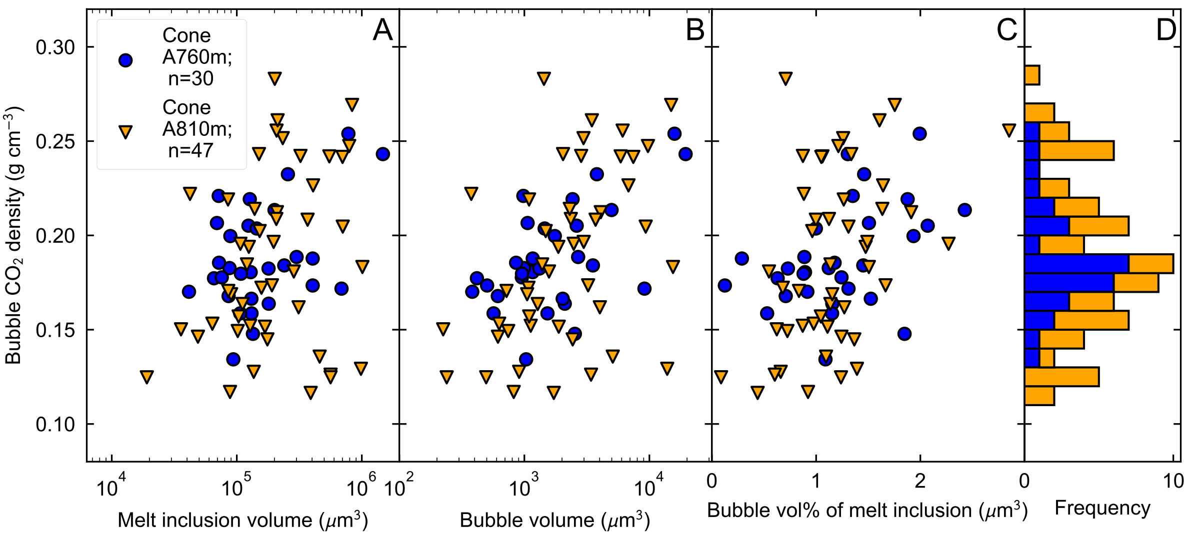

Figure S4. Bubble CO_2 density plotted against A. volume of melt inclusions, B. volume of shrinkage bubbles, C. bubble volume percentage of melt inclusions. D. Histogram of bubble CO_2 density.

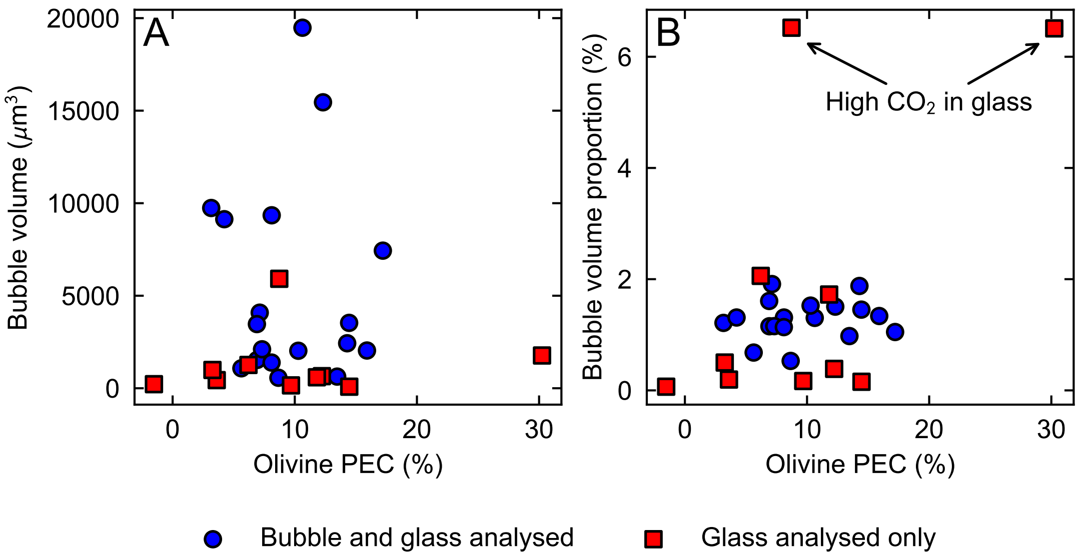

Figure S5. Olivine post-entrapment crystallization of analyzed melt inclusions plotted against A. bubble volume, and B. bubble volume as a proportion of the melt inclusion.

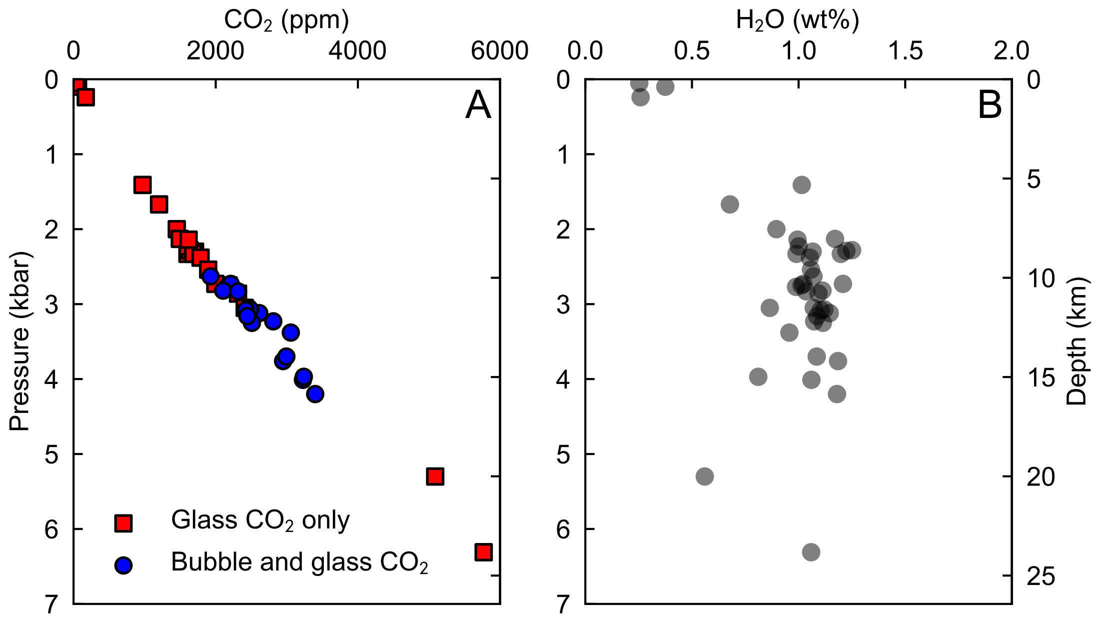

Figure S6. A) CO_2 and B) H_2O concentrations of MER melt inclusions plotted against volatile saturation pressures calculated using MagmaSat (Ghiorso & Gualda, 2015).

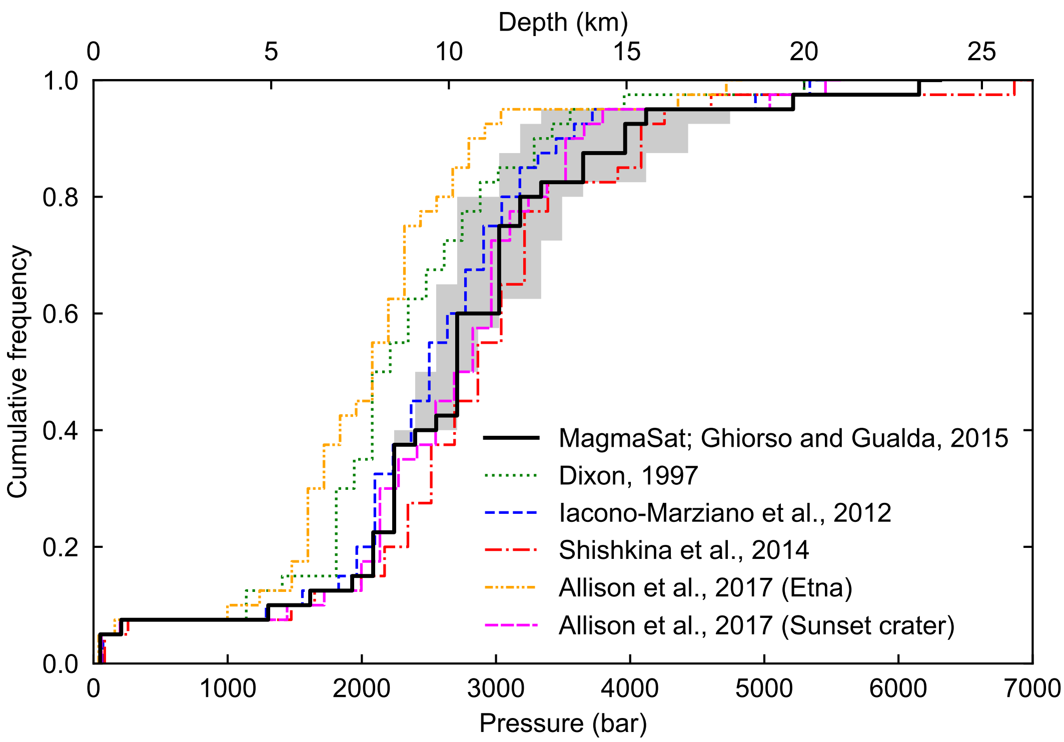

Figure S7. Cumulative distribution functions of entrapment pressures from different solubility models. The shaded region shows the error on MagmaSat entrapment pressures resulting from uncertainty in estimating bubble proportions from 2D images (Tucker et al., 2019).

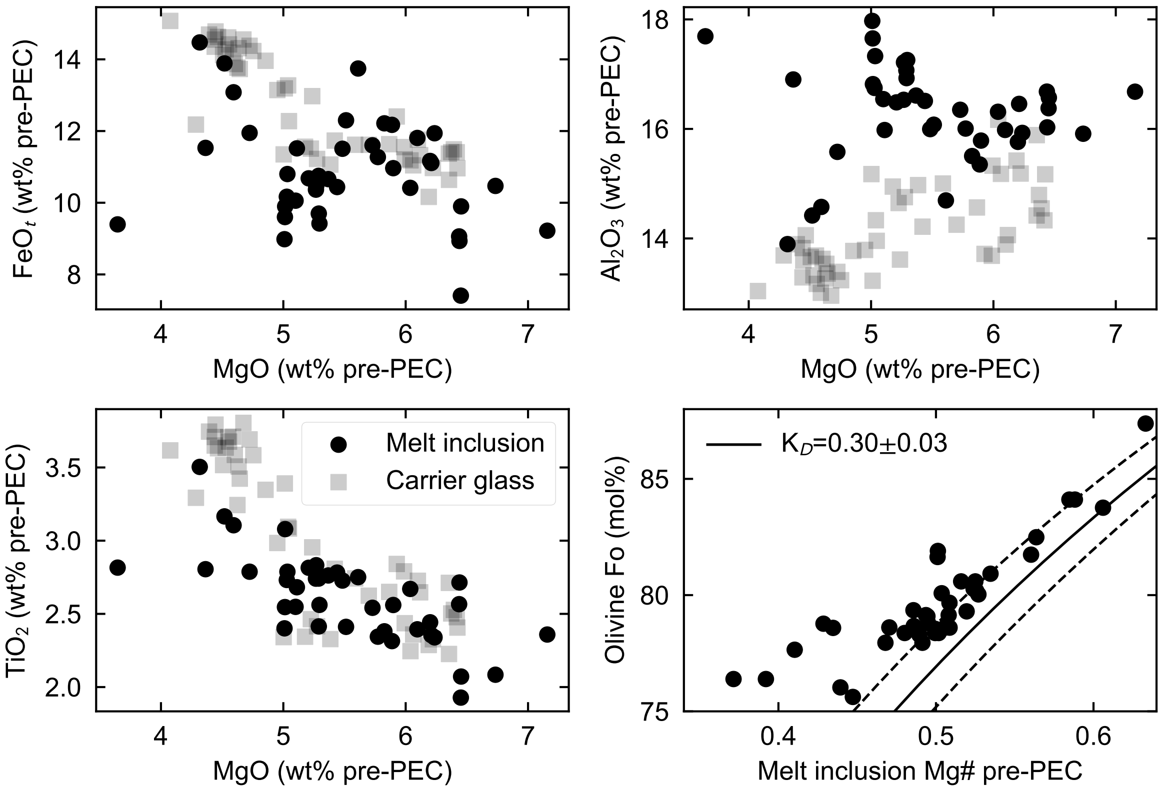

Figure S8. Melt inclusion major element geochemistry before post-entrapment crystallisation corrections. Carrier glass compositions are shown as the faded squares. Mg# is calculated as Mg/(Mg+Fe^{2+}), assuming 90 % of Fe is Fe^{2+}. Fo is calculated as in the caption to Figure 3 in the main text.

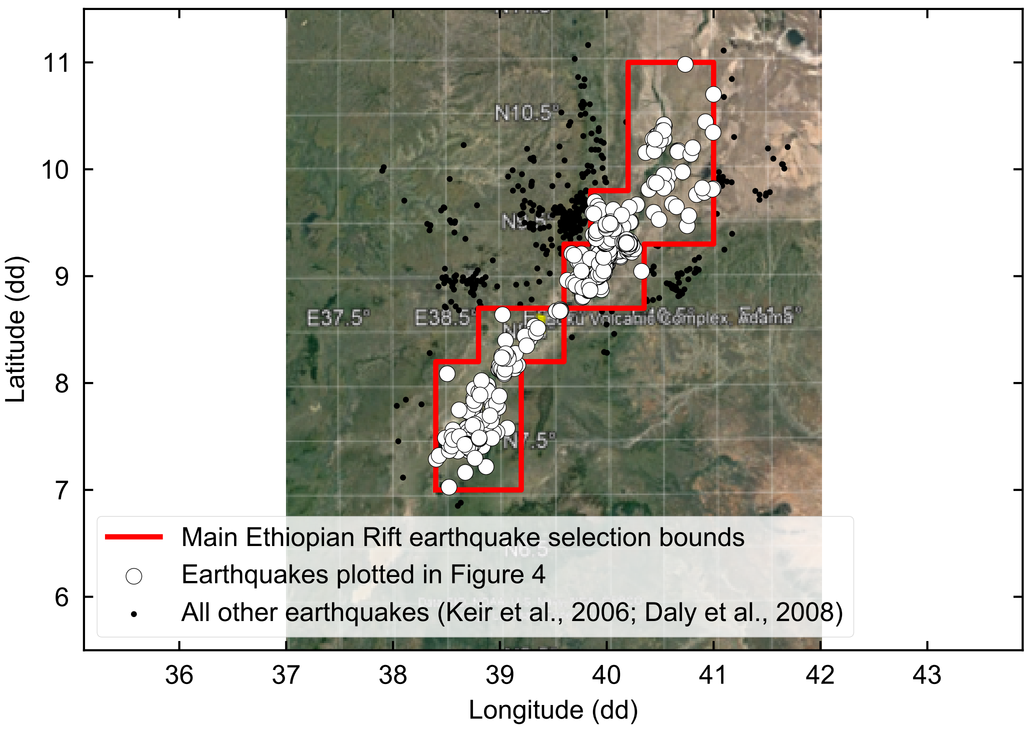

Figure S9. Earthquakes selected for earthquake histogram of Figure 4C in the main text. Areal limits are selected to encompass only earthquakes within the MER, and to avoid earthquakes that may be attributed to rift border fault seismicity. Earthquake data is from the EAGLE project (Keir et al., 2006; Daly et al., 2008).